DOCTORAL SCHOOL
UNIVERSITA' *MEDITERRANEA* DI REGGIO CALABRIA

DIPARTIMENTO DI INGEGNERIA DELL'INFORMAZIONE, DELLE INFRASTRUTTURE E DELL'ENERGIA SOSTENIBILE (DIIES)

PHD IN
INFORMATION ENGINEERING

S.S.D. ING-INF/02
XXXII CICLO

NUMERICAL MODELING AND REALIZATION OF MICROWAVE DEVICES FOR DIELECTRIC AND METALLIC ACCELERATORS

CANDIDATE

Giorgio Sebastiano MAURO

ADVISORS

Dott. Ing. Luigi CELONA

Prof. Gino SORBELLO

COORDINATOR

Prof. Tommaso ISERNIA

REGGIO CALABRIA, Febbraio 2020

Finito di stampare nel mese di **Febbraio 2020**

Edizione CSdA Centro Stampa d'Ateneo

Quaderno N. 46
Collana *Quaderni del Dottorato di Ricerca in Ingegneria dell'Informazione*
Curatore *Prof. Claudio De Capua*

ISBN 978-88-99352-39-4

Università degli Studi *Mediterranea* di Reggio Calabria
Salita Melissari, Feo di Vito, Reggio Calabria

GIORGIO SEBASTIANO MAURO

NUMERICAL MODELING AND REALIZATION OF MICROWAVE DEVICES FOR DIELECTRIC AND METALLIC ACCELERATORS

The Teaching Staff of the PhD course in
INFORMATION ENGINEERING
consists of:

Claudio DE CAPUA (coordinator)
Antonio IERA
Antonella MOLINARO
Giuseppe RUGGERI
Giuseppe ARANITI
Francesco Giuseppe DELLA CORTE
Riccardo CAROTENUTO
Fortunato PEZZIMENTI
Tommaso ISERNIA
Giovanni ANGIULLI
Francesco Antonio BUCCAFURRI
Domenico URSINO
Gianluca LAX
Rosario CARBONE
Sofia GIUFFRE'
Salvatore COCO
Domenico ROSACI
Valerio SCORDAMAGLIA
Andrea Francesco MORABITO
Pasquale Giuseppe Fabio FILIANOTI
Aimè LAY EKUAKILLE
Sandro RAO
Giacomo Domenico Savio MESSINA
Mariateresa RUSSO
Pier Luigi ANTONUCCI
Patrizia FRONTERA
Mariantonia COTRONEI
Giuliana FAGGIO
Claudia CAMPOLO
Voicu GROZA
Antoine O. BERTHET
Dominique DALLET
Luigi Giuseppe CELONA
Lorenzo CROCCO
Rosario MORELLO
Ivo RENDINA

Abstract

This thesis deals about analytical, numerical and experimental procedures for the design and realization of metallic and dielectric particle accelerators, along with related devices.

The first part, performed in the European Spallation Source (ESS) framework, is dedicated to the metallic accelerators and in particular to the ESS Drift Tube Linac. The numerical simulation of such structures, large cylindrical cavities composed of many cells, is not an easy task but results an essential step in the cavity electromagnetic design. In order to ease the simulation of large metallic structures such as the DTL, some analytical and numerical methods have been developed. These methods are able to predict, the frequency error introduced when the real structure is discretized inside the commercial electromagnetic simulators or can create computationally advantageous symmetries into the considered structure. These techniques have been employed in the electromagnetic design of a DTL tank cold model, which has been realized in order to test the field measurement setup and to obtain a field stabilization procedure to counteract random manufacturing errors that could degrade the accelerator performances.

The second part of this thesis, performed in the DiElectric and METallic Radiofrequency Accelerator (DEMETRA) framework, is focused on the study and numerical simulation of Dielectric Laser Accelerator devices. In particular, the woodpile structure has been studied through the use of numerical tools and an alumina prototype, operating at X-band, has been realized and experimentally characterized in terms of S-parameters and on-axis electric field, showing very good agreement with the numerical results. The knowledge acquired with the alumina prototype has led the way to the realization of a silicon prototype, operating in the W-band, which has been successfully characterized.

Contents

List of Figures

List of Tables

1

Introduction

Linear accelerators (LINACs) have a wide variety of utilization nowdays. From research to medicine, these machines are increasingly being used in small, as well as big, institutions.

The LINACs are usually large metallic standing wave structures that accelerate ions from few to some dozens of MeV or more compact travelling wave structures for electron acceleration. The RF design of such structures that will serve to accelerate and guide the electrons or ions toward its length plays a fundamental role in the overall LINAC design and on its final performances. Such design can be quite complicate, also considering that the LINAC contains several parts in order to achieve the correct electric field for proper particle acceleration. Usually the electromagnetic study can be carried out by employing commercial electromagnetic CADs such as Ansys HFSS or CST Studio Suite.

The thesis is focused on the RF design of proton and electron LINACs: numerical methods have been used to study the structure and a few prototypes of the accelerating structures have been realized.

The first part of the thesis is dedicated to the design methods of large proton accelerating structures and has been performed in the **European Spallation Source (ESS)** framework. Numerical and analytical methods to properly simulate such complex structures have been evaluated and successfully applied to the ESS structures. The numerical results have been used to realize a 'cold model' of the ESS DTL tank 2: the measured values have been found in very good agreement with the simulations in terms of scattering parameters and accelerating electric field. The prototype has then been employed in order to develop a field stabilization procedure with the objective to make the accelerating field immune from manufacturing errors, that is an essential requisite for a proper particle acceleration. The prototype tuning procedure can be quite complex and time consuming so, in order to make the process more user friendly, a post processing program has been developed in conjunction with the RF

tuning operations to aid the measured data evaluation. The tuning and stabilization procedure returned acceptable results, showing the validity of the developed methods.

The second part of the thesis, performed in the **DiElectric and METallic Radiofrequency Accelerator (DEMETRA)** framework, deals with the study of innovative dielectric accelerating structures (DLA) for electrons. These periodic structures, based on the photonic crystals (PhC), are obtained by the construction of periodic patterns of dielectric material whose elements (for example dielectric bricks or holes practiced into a dielectric slab) are disposed with a proper periodicity that allows or inhibits the electromagnetic waves propagation. By removing some dielectric material from these periodic patterns one can create a so called 'defect' that, by breaking the periodicity, permits the selective propagation of a guided e.m. mode. The DLA permits to overcome the fundamental limitations of the standard metallic accelerators and in particular, by eliminating the problem of power dissipation on the metallic walls, permits to push the working frequencies to the optical regime while at the same time allowing the reach of high accelerating energies, to the order of the GeV. Other advantages of these structures are the compactness and the high scalability. In this thesis the attention has been focused to the woodpile structure: after the study of the PhC and the achievement of the modal structure (the so called band diagram), a woodpile waveguide operating at X-band and able to support a guided mode has been numerically studied and validated through a prototype realization. A very good agreement has been achieved in terms of S-parameters and electric field between the measured values and the ones obtained in simulation. Due to the high voltage that this allumina structure can sustain (up to 40 kV), it can also be employed as a DC-break device and mounted in the RF feed line of microwave ion sources. The good results obtained with the X-band prototype confirmed the expected working behaviour and the structure has been easily scaled to the W-band. Another prototype working around 90 GHz has been therefore constructed, this time made of silicon. The successful characterization will lead the way to the future realization of a full-dielectric PhC coupler, necessary to transform a 'launch' telecom mode into an accelerating TM-like mode, that will be used with laser sources for electron acceleration.

1.1 Linear accelerators

The RF linear accelerator is classified as a resonance accelerator. Because both ends of the structure are grounded, a LINAC can easily be constructed as a modular array of accelerating structures. The modern linac typically consists of sections of specially designed waveguides or high-Q resonant cavities that are excited by RF

electromagnetic fields, usually in the VHF and UHF microwave frequency ranges. The accelerating structures are tuned to resonance and are driven by external, high-power RF tubes, such as klystrons, or various types of gridded vacuum tubes. The particles are launched inside the structure in bunchs and they are accelerated from the electric field excited inside the cavity, provided that the beam bunch is isochronous with the maximum accelerating filed along the LINAC, as shown in Fig. 1.1. The bunches may be separated longitudinally by one or more RF periods.

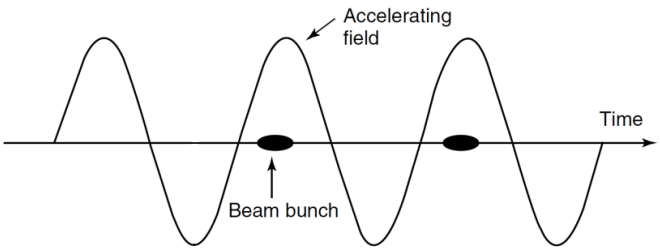

Fig. 1.1: Schematic of a particle bunch accelerated by an electric field.

1.2 Proton LINACs VS electron LINACs

One of the most famous linear accelerator for protons is the Drift Tube Linac (DTL), represented in Fig. 1.2: this long standing wave cavity can be divided into cell of different (increasing) lengths. The fields in all cells have the same phase so that the multicell structure can be said to operate in a 0-mode.

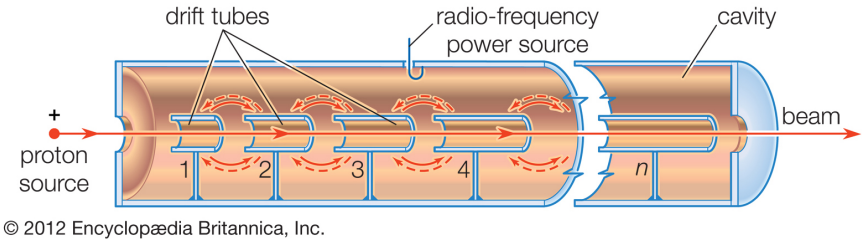

Fig. 1.2: Drift Tube Linac model.

Suppose we want to accelerate the beam to high energies in a long standing wave cavity. In order to work as an accelerator, the electric field must be along the direction of beam propagation. The beam must consist of bursts of particles with space in between the bursts. A burst of particles timed so as to see the accelerating portion

of the field is called a "bunch". Typically, the electric field is driven by a sinusoidal voltage oscillating in time at the frequency of the cavity, see Fig. 1.3, and so the polarity of the electric field will be accelerating only half of the RF period ($T/2$), the rest of the time the field is oriented in such a way as to decelerate the beam. Thus, when alternating fields are used to accelerate particles, the beam cannot be a continuous stream of particles, for then half the particles would be decelerated instead of accelerated.

The solution has been proposed by Alvarez and consists to install hollow conducting drift tubes along the axis, as shown in Fig. 1.3, into which the RF electric field decays to zero, as in a waveguide below the cutoff frequency. This creates field-free regions that shield the particles when the polarity of the axial electric field is opposite to the beam direction.

It is evident that, for a DTL structure, the maximum energy gain corresponds to the condition that a particle inside the bunch travels from one gap to the next in a time equal to T. In this case the particle will see an accelerating field in all the gaps. If we define the particle relativistic velocity as $\beta = \frac{v}{c}$ with v the particle velocity and c the speed of light, for a particle travelling at the relativistic velocity β, the time to cross one cell of length L is $\tau = \frac{L}{\beta c}$. The condition $\tau = T$ gives the required cell length for a 0-mode structure such as the DTL:

$$L = \tau\beta c = T\beta c = \beta\lambda \tag{1.1}$$

From this synchronism condition, it is clear that an electron LINAC, where the particles have $\beta = 1$ apart from a short initial section, will be made of a sequence of identical accelerating structures, with cells of the same length $L = \lambda$. The case of the proton LINAC is totally different, because β increases slowly by orders of magnitude, and the cell length has to follow a precise β profile: the cell length will increase as the particle travels along the structure.

As said before, the drift tubes allow us to divide the cavity into cells of length $\beta\lambda$ extending from the center of one drift tube to the center of the next, as shown in Fig. 1.4.

For a DTL cell it is more practical to work with the average electric field E_0: it defined as the integral of the cell axial field $E(z)$ along the cell axial length. The average voltage in every cell V_0 varies with cell length $\beta\lambda$, and because $V_0 = E_0\beta\lambda$ in practice it is possible to tune a DTL that has constant E_0 in every cell (but the electric field in the gaps, $E(z)$, will vary with cell geometry). The drift tubes are supported mechanically by stems attached to the outer wall, as seen in Fig. 1.4.

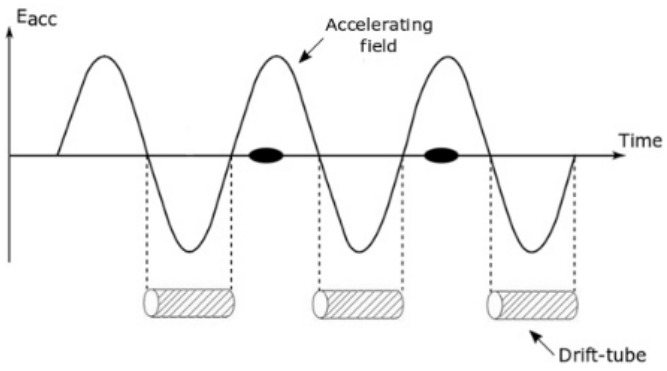

Fig. 1.3: Typical accelerating field of a metallic linear accelerator. Drift tubes are placed in the zones where a decelerating field would be otherwise present, creating a field-free region for travelling particles.

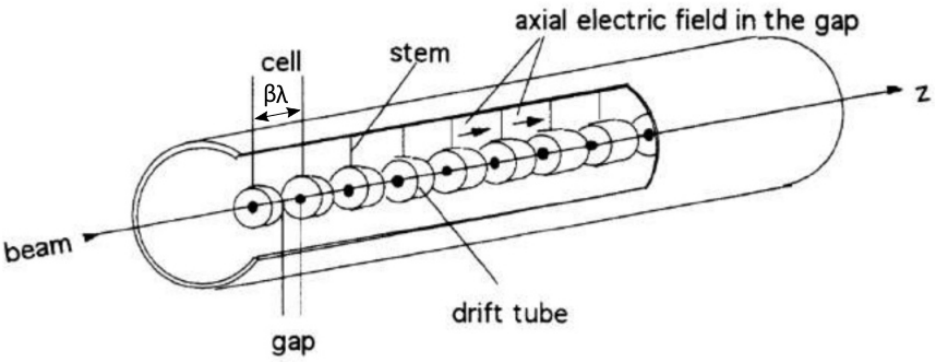

Fig. 1.4: Schematic of a DTL. The structure can be divided into cells, extending from the center of one drift tube to the center of the next. The cell length for a structure operating in the 0-mode (i.e. the distance from two drift-tube centers) is $\beta\lambda$, with β increasing as the particle travels along the structure. The drift-tubes are attached to the cavity outer wall through metal cylinders called 'stems'.

A body of mass m_0, at rest with respect to an observer, represents a supply of energy (called rest-mass energy or rest energy for short) given by W_0, where $W_0 = m_0c^2$. Now let this mass be given some kinetic energy T, as by launching a particle into an accelerator [1]. The total energy is

$$W = W_0 + T \Rightarrow W = m_0c^2 + T \tag{1.2}$$

By expressing the previous equation in terms of total mass, we obtain

$$mc^2 = m_0c^2 + T \Rightarrow T = c^2(m - m_0) \tag{1.3}$$

By remembering the relativistic statement for the mass as a function of velocity $m = \frac{m_0}{(1-v^2/c^2)^{1/2}}$ it can be written

$$T = m_0c^2\left(\frac{1}{(1-v^2/c^2)^{1/2}} - 1\right) \tag{1.4}$$

if v is very small compared with c, this may be expanded in a power series in v/c

$$T = m_0c^2\left[1 + \frac{1}{2}\left(\frac{v}{c}\right)^2 + \frac{3}{8}\left(\frac{v}{c}\right)^4 + \cdots - 1\right] \tag{1.5}$$

and if the terms $(\frac{v}{c})^4$, $(\frac{v}{c})^6$, etc, are neglected, this reduces to

$$T = \frac{1}{2}m_0v^2 \tag{1.6}$$

As long as the velocity is very small compared with that of light, the simple expression for kinetic energy is an adequate approximation of the truth, but it fails when the velocity is high, and the relativistic expression previously defined must be used because always correct. The *relativistic* expression for kinetic energy then becomes

$$T = m_0c^2\left(\frac{1}{(1-\beta^2)^{1/2}} - 1\right) \tag{1.7}$$

and expressing it in terms of β yields to

$$\beta^2 = 1 - \frac{1}{\left(1 + \frac{T}{m_0c^2}\right)^2} \tag{1.8}$$

The basic difference between electrons and ions [2] is their rest mass. The mass of an electron at rest is 9.1×10^{-31} kg while a proton has a mass of 1.6×10^{-27} kg: because of this mass difference, the two particles react differently when an RF field is applied inside the accelerating structure.

As said earlier, when accelerating particles the goal is to synchronize the accelerating field with the travelling particle in such a way that the particle sees the same field amplitude in each gap and thus it can be accelerated.

If we plot (1.8), β^2 VS the gained kinetic energy (i.e. the distance along the accelerator) for electrons ($m_0c^2 = 511$ keV) and for protons ($m_0c^2 = 938$ MeV) it can be seen that the electrons come close to the speed of light already after few MeV of energy, and for the rest of the acceleration process their velocity will not change. The plot is shown in Fig. 1.5.

Instead, in a proton LINAC the particles have a slow increase in velocity as the energy increases. After reaching few GeV the velocity saturates towards c, well beyond

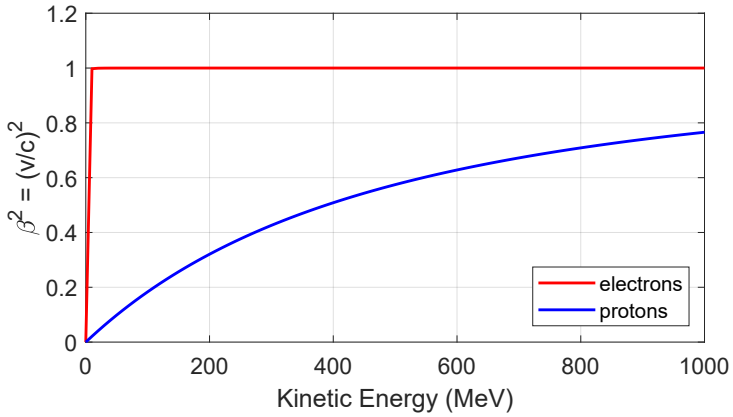

Fig. 1.5: Relativistic particle velocity (protons and electrons) as function of gained kinetic energy.

the energy range of most proton linacs. That is the reason why, in a proton LINAC, an adaptation to the increase in particle velocity needs to be taken into account: this is usually made by increasing the cell length with the proton velocity.

Another difference between proton and electron LINACs is found in the type of structure being used for acceleration.

Travelling wave structures are generally used for electrons at $\beta = 1$ (see Fig. 1.6), designed to have phase velocity $v = c$ for a given operating frequency. Input and output coupler are used to inject the RF wave and to extract at the end of the structure the remaining RF power. Electrons enters into the structure when the electric field is at its maximum and will travel along the LINAC with the same velocity as the wave, seeing the maximum accelerating electric field all along the structure and thus increasing their energy. The beam energy comes from the RF wave: part of the RF energy of the wave will be dissipated in the structure walls, usually made out of copper, part will be absorbed by the beam, and the rest will be extracted via the output coupler, to be absorbed in a matched load at the end of the structure.

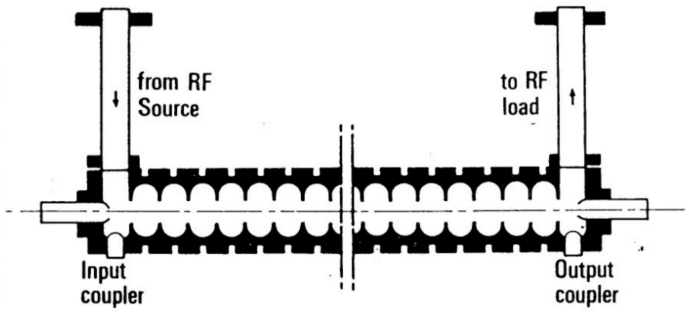

Fig. 1.6: Schematic of a typical travelling wave structure for particle acceleration.

Travelling wave structures are designed for a fixed phase velocity, and can not be used for ions at $\beta < 1$. Even if the structure could be designed for a lower phase velocity corresponding to the initial β of the particles, when gaining energy the beam velocity would increase and the synchronism with the wave would be lost.

When dealing with protons, instead of matching the phase velocity of a travelling wave to the particle velocity, we can realize the synchronism between moving particles and field by keeping constant the phase of the wave and by changing its space distribution accordingly to the synchronism condition. This is obtained in standing wave structures (RF cavities) like the DTL where the field is made 0 inside certain regions (the drift-tubes) as explained previously.

1.2.1 European Spallation Source (ESS) LINAC

The first part of this thesis deals with a proton accelerating structure and has been performed in the framework of the European Spallation Source (ESS).

The European Spallation Source (ESS) is a Research Infrastructure based in Lund (Sweden) with the vision to build and operate the world's most powerful neutron source, enabling scientific breakthroughs in research related to materials, energy, health and the environment, and addressing some of the most important societal challenges of our time. This multi-disciplinary research centre will perform research that can potentially lead to the next great inventions within pharmaceuticals, environmental technology, energy, cultural heritage or fundamental physics.

Here, in particular the attention will be focused on the Drift Tube LINAC, which is a part of the entire ESS accelerating system as shown in Fig. 1.7. The DTL, currently being assembled in the ESS Lund facility, is composed by 5 tanks working at 352.2 MHz with a constant average electric field of $\sim$ 3 MV/m; it can accelerate protons up to an energy of 90 MeV. This normal conducting accelerator creates and accelerates the proton beam using room temperature structures. It is composed of matching sections as well as of accelerating components. The accelerating components have the particularity to adapt their geometry as the velocity of the beam increases making the acceleration very efficient (see §1.2). The DTL has a total length of $\sim$ 38 m and counts 175 cells: each cell possess a drift-tube, a supporting stem and a post-coupler for field stabilization if necessary (depending on the increasing length).

When simulating electrically large complex structures such as Drift Tube Linac (DTL) cavity in 3D simulators, it is important to choose a model representation that is a compromise between accuracy and time/resource cost: in the case of a DTL, the whole structure can easily reach a length of a few tens of meters, so a numerical

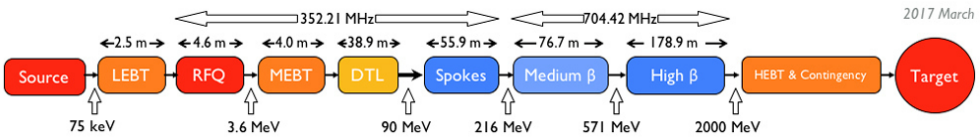

Fig. 1.7: Schematic of the ESS accelerating system.

representation problem is immediately evident. In fact, the simulation of such cavities, very complex in terms of geometry in particular due to the presence of the internal drift tubes and in general due to the presence of curved surfaces, can easily exhaust a high amount of computational resources in a very short time if the numerical problem is not smartly approached.

Usually an electromagnetic full-wave simulator makes convergence passes to reach the final solution: during a pass the model is meshed with a fixed number of tethraedrons and, for each pass, the difference between two subsequent curves of S-parameters (the ΔS, used in driven modal problems) or two subsequent stored energy values (the ΔU, used in eigenmode problems) is calculated. The convergence is considered reached when, for two successive passes, these values are below a previously fixed value. The simulator will give results even if the convergence is not reached after a fixed number of passes, but especially for large electromagnetic structures, this will probably lead to high inaccuracies in terms of operating frequency and field results.

Possible ways to obtain accurate simulation results and at the same time to simplify a complex model in the way to obtain the desired convergence with the computational resources at disposal, is to exploit axial symmetries or to try to predict the mesh needed to have a specific frequency error. In the last case one can decide if that frequency error is good enough for the application at hand and, eventually, settle with that mesh and try to reduce the model complexity in an alternative way. The numerical techniques that allowed us to obtain quite good results in the process of simulating the tanks of the ESS DTL will be discussed in the next chapter. In Fig. 1.8 a DTL model with its mesh (HFSS simulation) is depicted.

1.2.2 Dielectric Laser Accelerators (DLA) and high gradient electron sources

The dielectric structures for electron acceleration that will be the argument of the second part of this thesis have been studied and developed in the DiElectric and METallic Radiofrequency Accelerator (DEMETRA) framework, a collaboration between INFN-LNS, INFN-LNF, UniCT and UniBS. The experiment is dedicated to

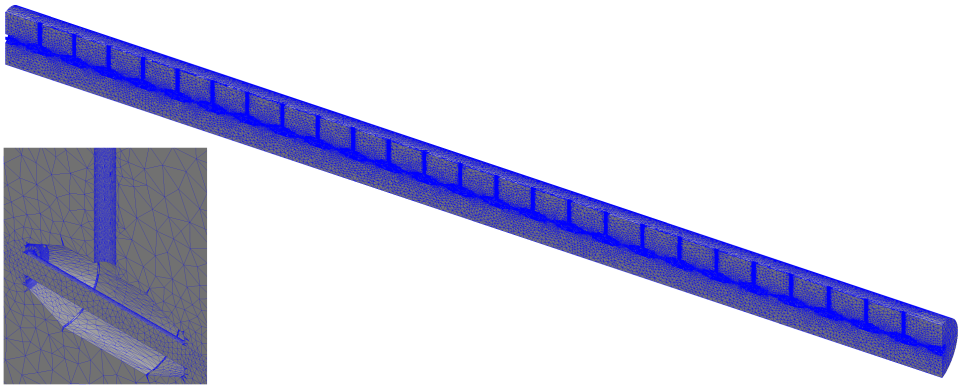

Fig. 1.8: Drift Tube Linac HFSS simulation: the meshing elements (tethraedrons) used for the cavity representation are visible.

the modelling, development and test of RF structures devoted to acceleration that possesses high gradient of particles through metal and dielectric devices.

Due to electrical breakdown of metals in the presence of high electric fields, conventional particle accelerators, which consist of metal cavities driven by high-power microwaves, typically operate with accelerating fields from 10 to several dozens of MV/m. Because of the high power loss in metals at optical frequencies, dielectrics are the only viable candidate for confinement of the electromagnetic energy in such schemes. The DLA eliminate the issues of metallic accelerators when operating at high frequency, such as the power dissipation on the metallic walls, and allow the reaching of higher accelerating gradients (to the order of the GeV).

Dielectric laser acceleration with driving wavelengths in the optical and near-infrared region requires electron beams with normalized emittance of a few nanometers so that the beams can be fed into and kept inside the structure channel. In addition, for most applications, particularly for free-electron laser applications, high peak currents are mandatory, requiring high-brightness electron beams.

For electron beams, the source is a piece of conducting material that forms the cathode. Electrons are accelerated across the potential difference in the diode and emerge through a hole in the anode. The cathode may be either heated (thermal emission) or cold (field emission) or the electrons may be produced by photoemission.

The beam brightness is defined as the number of particles, or the total beam current, with a given emittance [3].

For DLA the beam brightness is defined as [4]

$$B_n = \frac{B}{\beta^2\gamma^2} = \frac{2I}{\pi^2\epsilon_n^2} \tag{1.9}$$

where B is the geometric brightness, I is the electron bunch peak current, $\gamma = \sqrt{(1-\beta^2)}$ and $\epsilon_n = \beta\gamma\epsilon$ is the normalized emittance.

High gradient rf photo-injectors have been a key development to enable several applications of high quality electron beams. They allow the generation of beams with very high peak current and low transverse emittance, and in the past years photo-injectors with very good performances have been proposed [5].

1.3 Particle Acceleration in RF fields

Multicell ion LINACs are designed to produce a given velocity gain per cell. Particles that have the correct initial velocity will gain the right amount of energy to maintain synchronism with the field. Usually three phases can be defined: one for which the velocity gain is equal to the design value S, one earlier E and the last one later L than the crest of the accelerating wave inside the gap, as seen in Fig. 1.9.

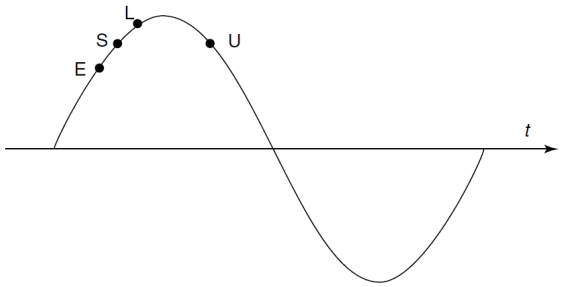

Fig. 1.9: Early (E), stable (S), late (L) and unstable (U) particle phases.

The earlier phase is called the synchronous phase and is the stable operating point. It is a stable point because nearby particles that arrive earlier than the synchronous phase experience a smaller accelerating field, and particles that arrive later will experience a larger field. This provides a mechanism that keeps the nearby particles oscillating about the stable phase, and therefore provides phase focusing or phase stability. The particle with the correct velocity at the stable phase is the synchronous particle, and it maintains exact synchronism with the accelerating fields. As the particles approach relativistic velocities, the phase oscillations slow down, and the particles maintain a nearly constant phase relative to the travelling wave. After beam injection into electron LINACs, the velocities approach the speed of light so rapidly that hardly any phase oscillations take place.

The final energy of each electron with a fixed phase depends on the accelerating field and the value of the phase. In contrast, the final energy of an ion that undergoes phase oscillations about a synchronous particle is approximately determined not by the field, but by the geometry of the structure, which is tailored to produce a specific final synchronous energy. For an ion linac built from an array of short independent cavities, each capable of operating over a wide velocity range, the final energy depends on the field and the phasing of the cavities, and can be changed by changing the field, as in an electron linac.

1.3.1 Figures of merit of a linear accelerator

Let's consider an accelerating gap as shown in Fig. 1.10. The electric field experienced by a particle travelling along the gap (radius $r = 0$) with a velocity v can be written as

$$E_z(r = 0, z, t) = E(0, z)\cos(\omega t(z) + \phi) \tag{1.10}$$

where $t(z) = \int_0^z v(z)dz$ is the time at which the particle is found at the position z. Here we chose $t = 0$ when the particle is in the gap center and at this instant the phase of the field relative to the crest is ϕ.

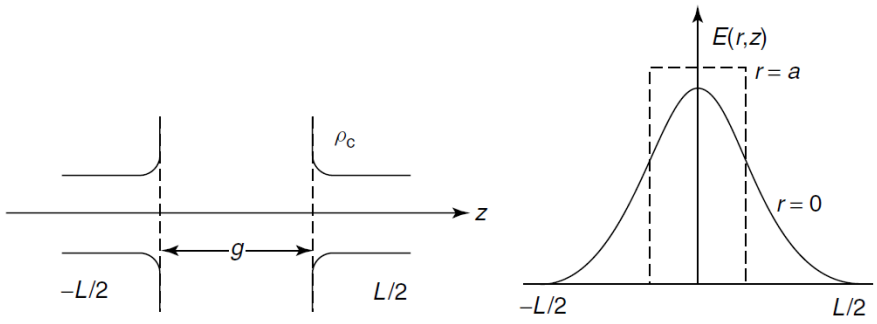

Fig. 1.10: Accelerating gap of length g. The field inside the gap is also shown.

The energy gain of an arbitrary particle with charge q that travels through the gap is

$$\Delta W = \int_{-L/2}^{L/2} E(0, z)\cos(\omega t(z) + \phi)dz \tag{1.11}$$

That, after the application of some trigonometry, can be written as

$$\Delta W = qV_0 T \cos\phi \tag{1.12}$$

$V_0 = \int_{-L/2}^{L/2} E(0,z)dz$ is the axial RF voltage. The quantity T is the *transit time factor*, defined as

$$T = \frac{\int_{-L/2}^{L/2} E(0,z)\cos\omega t(z)dz}{\int_{-L/2}^{L/2} E(0,z)dz} - \tan\phi \frac{\int_{-L/2}^{L/2} E(0,z)\sin\omega t(z)dz}{\int_{-L/2}^{L/2} E(0,z)dz} \tag{1.13}$$

Regardless of the phase ϕ, the energy gain of a particle in a harmonically time-varying field is always less than the energy gain in a constant dc field equal to that seen by the particle at the center of the gap. This is known as the transit-time effect, and the transit-time factor T is the ratio of the energy gained in the time-varying RF field to that in a dc field of voltage $V_0 cos\phi$. Thus, T is a measure of the reduction in the energy gain caused by the sinusoidal time variation of the field in the gap.

Usually one can define an average axial accelerating field as $E_0 = \frac{V_0}{L}$. V_0 is the voltage gain that would be experienced by a particle passing through a constant dc field equal to the field in the gap at time $t = 0$ and E_0, which is an average field over the length L, does depend on the choice of the latter. So, when a value of E_0 is quoted for a cavity, it is important to specify the corresponding length L. For a multicell cavity, the natural choice for L is the geometric cell length.

If we call $E_0 T$ the accelerating gradient, we can write the sometimes called Panofsky equation, that is the energy gain in terms of the average accelerating field

$$\Delta W = qE_0 LT cos\phi \tag{1.14}$$

Of course, the peak energy gain experienced by the particle occurs when it passes through the center of the gap, for $\phi = 0$.

Usually $E(z)$ is an even function about the geometric center of the gap. In this case the transit time factor expression simplifies as

$$T = \frac{\int_{-L/2}^{L/2} E(0,z)\cos\omega t(z)dz}{\int_{-L/2}^{L/2} E(0,z)dz} \tag{1.15}$$

The transit-time factor increases when the field is more concentrated longitudinally near the origin, where the cosine factor is largest. Thus, the larger the gap between drift tubes and the more the field can penetrate into the drift tubes, the smaller the transit-time factor. The practice of constructing drift tubes with nose cones that extend further into the gap forces a concentration of the field near the center of the gap, and raises the transit-time factor.

By writing $\omega t \simeq \omega \frac{z}{/} v = \frac{2\pi z}{\beta\lambda}$, with $\beta\lambda$ the distance that the particle travels in an RF period, the transit time factor simplifies in

$$T = \frac{\int_{-L/2}^{L/2} E(0,z)\cos(\frac{2\pi z}{\beta\lambda})dz}{\int_{-L/2}^{L/2} E(0,z)dz} \tag{1.16}$$

In order to characterize accelerating cavities, in the following some of the most important figures of merit will be defined.

For a metallic cavity with total stored energy U and average power loss on the walls P, one can define the well known cavity factor as

$$Q = \frac{\omega_0 U}{P} \tag{1.17}$$

We define the *shunt impedance* as an index of the effectiveness of producing an axial voltage V_0 for a given power dissipated. It is usually expressed in MOhm.

$$r_s = \frac{V_0^2}{P} \tag{1.18}$$

Remembering that the maximum energy gain of the particle occurs when it is placed at the center of the gap (when $\phi = 0$), the *effective shunt impedance*, a parameter measuring the effectiveness per unit power loss in delivering energy to the particle, can be defined as

$$r = (\frac{\Delta W_{\phi=0}}{q})^2 \frac{1}{P} = \frac{(V_0 T)^2}{P} = r_s T^2 \tag{1.19}$$

For long cavities it is often preferable to use a figure of merit that is independent of both the field level and the cavity length L. Thus, it is also convenient to introduce *shunt impedances per unit length*

$$Z = \frac{r_s}{L} = \frac{E_0^2}{P/L} \tag{1.20}$$

and the *effective shunt impedances per unit length*

$$ZT^2 = \frac{r}{L} = \frac{(E_0 T)^2}{P/L} \tag{1.21}$$

The last two usually are in the order of MOhm/m. Especially for normalconducting cavities, one of the main objectives in cavity design is to choose the geometry to maximize effective shunt impedance per unit length. This is equivalent to maximizing the energy gain in a given length for a given power loss.

In the case of a dielectric accelerator, a *characteristic interaction impedance* can be defined as [4], [6]

$$Z_c = \frac{(E_{acc}\lambda)^2}{P} \tag{1.22}$$

and it is a measure of the effective accelerating field E_{acc} that acts on the electrons for a given electromagnetic power flowing into the system P. As for metallic accelerators, high Z_c values corresponds to a more efficient accelerator. The Z_c is distinguished from the shunt impedance r_s of metallic accelerators because the latter uses the power loss on the metallic walls instead of the power flowing into the system. A possible way to increase the interaction impedance in a dielectric accelerator is to use a material with high ϵ_r or to properly tune the guiding channel practiced into the dielectric.

For the dielectric accelerators an *effective characteristic impedance* can be defined in a similar fashion of that defined for metallic accelerators:

$$Z = \frac{(E_{acc}\lambda T)^2}{P} \tag{1.23}$$

and the quantity $E_{acc}T$ is called accelerating gradient.

Part I

Metallic accelerating structures

In the previous section the differences between proton and electron LINACs have been discussed. In the context of the ESS Drift Tube Linac realization, chapter 2 of this thesis deals with the analytical and numerical approaches used for the RF tuning of these large standing wave cavities, while chapter 3 presents the experimental results obtained with the realized cold model of the DTL tank 2. Finally, in chapter 4 a novel X-band structure for electron acceleration is presented and the experimental results obtained on a realized prototype are discussed.

2

Numerical study of metallic accelerators

In order to simulate the DTL cavities of the ESS LINAC, a set of representation methods have been developed. These methods, analytical and numerical, have the aim to find equivalent volumes in the way to simplify the simulation (i. e. to exploit rotational symmetry to simulate object slices) and, in conjunction or in alternative, to derive an analytic frequency error prediction formula, through structure symmetry exploitation, that ensures the required precision in real structure 3D representation, while using fair amount of computational resources. Both methods have been successfully applied to design of the European Spallation Source (ESS) DTL cavities, now under construction.

2.1 Problem definition

3D simulators are becoming very useful nowdays, when a structure experimental tuning is required, to reduce the cost and time delay. When modelling complex structures in 3D FEM solvers, the real structure is discretized in a finite number of mesh elements, usually tethraedrons. This results in an approximation of the real structure that in many situation introduces a systematic geometrical error as in the case of curved boundaries presence. In order to have a faithful description it is always possible to have a finer and finer mesh by reducing the mesh size and increasing the mesh elements. However, computational resources impose a limit to this process.

A common choice/workaround to reduce the total number of mesh elements is to use simplified models (i.e. coarse mesh). Examples are mesh that neglect some geometric detail of the structure or mesh that follow curved or jagged boundary with low precision. A different approach is to use a2D reduced model exploiting symmetries, when present; in this case a virtually exact result is obtained with order-of-magnitude-less mesh elements. However, in general, simplified model may lead to inaccurate result if some important geometrical detail is lost or if the symmetry is only partially

verified. Beside the possibility to work on a reduced computational domain, another approach to follow, also in combination with the above one, is to determine beforehand the appropriate geometric approximations to have both a minimum number of mesh elements and, at the same time, a numerical error below a fixed threshold. This scheme is very effective when compared to automated standard approach that refine the mesh during subsequent passes (i.e. with successive iterations until the required precision is reached). This automatic process is time consuming and, in general, may lead to mesh refinements also where not necessary.

In this section we apply a combination of the above discussed strategies: symmetry exploitation and predetermined geometric approximation. Through this section, as an example, we refer to a Drift Tube Linac (DTL) cell (see Fig. 2.3) but the methods have been successfully applied to the entire DTL tanks of the ESS project. Moreover the methodology is general; for instance, in [7] a similar approach is applied to a Radio Frequency Quadrupole accelerator (RFQ) as well.

The proposed method, presented in [8], allowed us to reach the correct simulation parameter to keep frequencies error below a prefixed threshold.

2.1.1 Symmetry and 2D reduced models

To exploit any symmetry problem to greatly reduce the total number of mesh elements while maintaining an accurate geometrical description is always a good choice.

Reflection (or mirror) symmetries [9], translational invariance [10] and rotational symmetries [11] can effectively reduce the computational domain and thus the size of the numerical problem.

For example it is well known that in a $a \times b$ rectangular waveguide the height b influences the waveguide loss but not other properties such as the cut-off frequency. This is due to the y-transnational in-variance of the fundamental mode TE10 and such property can be used in numerical simulations and also in practical realization of non standard wave-guides: examples are reduced-height waveguide to increase the mode overlap in launchers [12] and reduced-height waveguides in waveguide arrays to save physical space [13] or larger-height waveguides to accommodate higher power [14]. This y-invariance can be easily exploited also when solving numerical problems with PEC boundaries and no surface losses (with a huge reduction of the mesh size). In [10] this property has been applied to a finite conductivity rectangular waveguide by using a reduced computational domain while retaining an accurate prediction of the losses thanks to an appropriate correction factor.

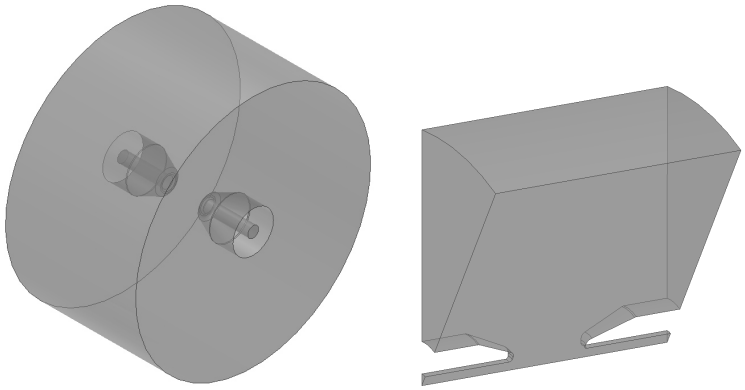

(a) (b)

Fig. 2.1: 3D representation of a Drift Tube Linac cavity cell: (a) full structure and (b) slice.

Circular waveguides and rotational symmetric cavities such as the DTL cavity shown in Fig. 2.1(a) can also exploit a reduced 2D simulation domain with virtually exact simulation results. Moreover, differently than in the rectangular waveguide case, also the conductor losses are correctly predicted even if a small angular sector of the cavity is simulated without the need any correction factor (see Fig. 2.1(b)).

We will refer to the 3D simulation of a small angular sector as a quasi-2D simulation.

For a DTL cavity without stem it is actually possible to exploit the rotational symmetry of the geometry and to use a quasi-2D simulation in a small angular sector of the full 3D-structure or even a 2D code cell representation. The resulting 2D (rotationally symmetric) problems can be solved with standard numerical approaches such as Finite Difference Time Domain (FDTD) and Finite Element Method (FEM). We used a code for 2D simulations, already available to the accelerator community, called Superfish [15], [16].

When, thanks to an exact symmetry, a 3D problem can be reduced to a 2D one without any approximation, the significant reduction of the problem dimension in term of mesh elements, makes possible to refine the mesh with standard brute force approach and to obtain rapidly converging results toward the "ideal" resonant frequency with small computational time. This frequency value is virtually exact and can be considered as a reference for benchmarking the 3D simulations.

2.1.2 Curved surfaces and mesh

Fig. 2.2(a) shows the front view of a circular "pillbox" DTL cavity. When representing the structure using a 3D simulator such Ansys HFSS [17] the mesh engine creates a

regular polygon mesh inscribed inside the cylindrical real structure. Whatever the mesh size/precision chosen, the simulated volume will be lower than the real cylindrical volume. The more the mesh is coarse, the greater the geometrical error will be and thus the frequency and field errors will results, since the inscribed polygon fails to represent the real structure in a satisfactory and coherent way.

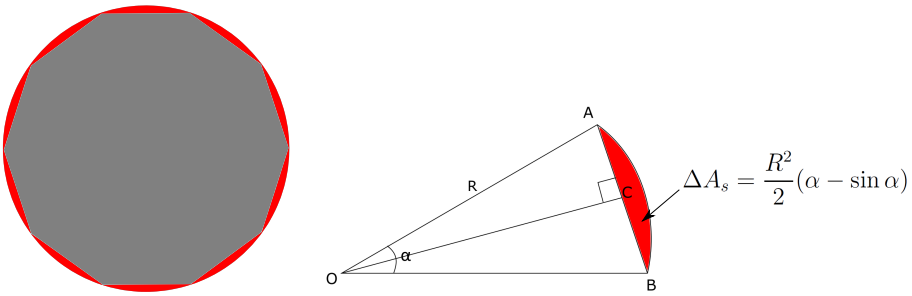

(a) (b)

Fig. 2.2: (a) Front view of a simulated circular cavity. Highlighted in red is the difference between real and simulated profile. (b) Circular sector of a cylindrical cavity.

Obviously, if the mesh density is increased, the real structure can be represented in a more accurate way and thus the simulated results will be more accurate. 3D simulators allow users to set the beginning mesh density, but for complex structures it is not straightforward to choose between a coarse mesh that could lead to inaccurate results, and an overly accurate mesh that could cost in resources and simulation time.

When is possible to exploit the rotational symmetry and to perform 2D simulations, the above described error is not introduced because 2D rotations are analytically considered in the 2D formulation. However, as already discussed, when stems (in the case of a DTL cavity) or other geometrical details break the rotational symmetry, the cavity cannot be simulated with 2D codes (see Fig. 2.3).

2.2 Proposed approach

In a cavity at the resonance frequency f_0, the stored electric and magnetic energies are equal.

When the cavity is perturbed (in our case a perturbation will be either the stem or the coarse mesh on the outer wall) this will produce an unbalance of the latters and the frequency will shift to restore the balance [18], [19]. If this frequency shift is in relation with a coarse or incomplete description of the simulated geometry, it can

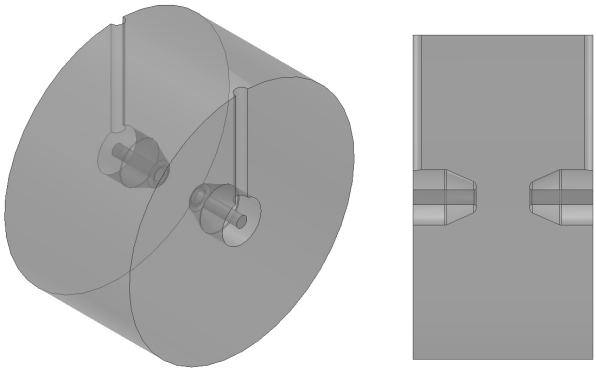

(a) (b)

Fig. 2.3: Rotational symmetry and stem: (a) 3D and (b) side view of a DTL cell model. Central element is called drift tube and is attached to the cavity outer wall through a metal cylinder called stem. The presence of stem breaks axial rotation symmetry and this makes necessary full 3D simulations.

be considered as a frequency error on the simulated structure. From the theory we have [20], [18, Eq. (5.88), pag. 165], [19, Eq. (6.19), pag. 252]:

$$\frac{\Delta f_0}{f_0} = \frac{\Delta \omega_0}{\omega_0} = \frac{\int_{\Delta V}(\mu H^2 - \epsilon E^2)\mathrm{d}V}{\int_V (\mu H^2 + \epsilon E^2)\mathrm{d}V} = \frac{\Delta U_m - \Delta U_e}{U} \tag{2.1}$$

where

$$\Delta U_m = \frac{1}{4}\int_{\Delta V} \mu H^2 \mathrm{d}V \tag{2.2}$$

and

$$\Delta U_e = \frac{1}{4}\int_{\Delta V} \epsilon E^2 \mathrm{d}V \tag{2.3}$$

are, respectively, the time average of the stored magnetic and electric energy removed by the perturbing object and

$$U = \frac{1}{4}\int_V (\mu H^2 + \epsilon E^2)\mathrm{d}V \tag{2.4}$$

is the total stored energy inside the cavity.

We will use (2.1) to derive an analytical formula that can be employed to correct or predict the frequency error introduced by the structure discretization in the 3D simulator.

2.2.1 2D reference simulation

The first step was to simulate the 2D version of the DTL cell using Superfish simulator. Stem presence and its frequency effect are not directly considered in Superfish, but

can be added later, directly within the code, through an automatic calculation based on Slater theorem (2.1).

Without the physical stem presence, we obtain an object that possesses a rotational symmetry and so we can use a very accurate mesh, located on the sheet of Fig 2.4(a), to obtain a virtually error free reference simulation.

In Fig 2.4(b) the accelerating electric field E_z on the cavity axis is also shown for half cell.

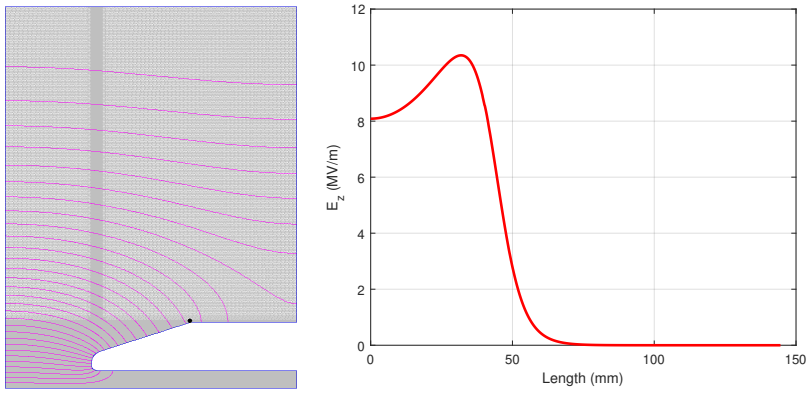

(a) (b)

Fig. 2.4: (a) Superfish DTL cell representation. Thanks to the rotational symmetry, only half of the structure is actually simulated by using an extremely fine mesh. (b) Electric field E_z obtained for the considered cell.

2.2.2 3D curved boundaries and mesh error prediction

Fig. 2.2(b) shows how a generic tetrahedron edge approximate an actual curved boundary in 3D simulators.

The frequency error $\Delta f_0 = f_0 - f_{mesh}$, where f_0 is the correct cavity resonant frequency while f_{mesh} is the perturbed frequency of the 3D model, can be related to the difference in volume ΔV between real profile and simulated one by using (2.1).

It is clear that if a coarse mesh is used a large volume error is introduced. This "subtracted" volume, ΔV, is "large" at the outer DTL wall where the stored magnetic energy predominate, i.e. in the "subtracted" volume $\Delta U_m \gg \Delta U_e$ and then, by using (2.2) on equation (2.1), one can write

$$\frac{\Delta f_0}{f_0} = \frac{1}{4U} \int_{\Delta V} \mu H^2 \mathrm{d}V \tag{2.5}$$

In order to calculate ΔV, we consider the cross section area difference between the real cavity profile and the simulated one, highlighted in red in Fig. 2.2(b), where the

edge AB approximates the real circumference arc; the quantity α, known as normal deviation angle[1], is a specific curved mesh quality parameter that can be enforced in Ansys HFSS to be lower than a fixed value in order to give a good geometrical approximation of the curved surfaces [17]. The objective of this section is to find an appropriate value of α that corresponds to a minimum but computationally reasonable frequency shift Δf_0. Then, by setting α, accurate electromagnetic results are obtained in virtue of (2.5).

We call V the real cavity volume. After the numerical discretization the new volume becomes V_{mesh} and we can define the quantity $V - V_{\text{mesh}} = \Delta V$. The permittivity ϵ and permeability μ of the medium are not varied and can be assumed constant. Also, we assume that the magnetic field, H, is constant inside ΔV. A case of particular interest occurs when the volume exhibits a cylindrical symmetry and the operational frequency f_0 corresponds to a mode with a little field variation along the axis. This is the case of TM_{010} mode, which is typically used in RF cavities employed as elements composing linear particle accelerators. In this case, if L is the cavity length and U the e.m. energy stored inside the cavity, by imposing $\Delta V = \Delta A L$ equation (2.5) reads

$$\frac{\Delta f_0}{f_0} \simeq \frac{1}{4U}\mu H^2 \Delta A L \tag{2.6}$$

where ΔA is the difference, referred to the circular cavity base, between the real profile and the discretized one. With reference to Fig. 2.2(b), let $N = \frac{2\pi}{\alpha}$ be the number of segments of the regular polygon inscribed inside the circle. So the precedent equation becomes

$$\frac{\Delta f_0}{f_0} \simeq \frac{1}{4U}\mu H^2 \Delta A_s N L \tag{2.7}$$

where ΔA_s is the difference, referred to a circular sector, between real curved DTL cross section area and the discretized cross section.

From Fig. 2.2(b), it can be seen that $\Delta A_s = A_{s1} - A_{s2}$. A_{s1} is the area of the circular sector and A_{s2} is the area of triangle AOB.

- For the calculation of A_{s1}, we know that

$$A_{sector} : A_{circle} = ang_{sect} : 2\pi \tag{2.8}$$

so

$$A_{s1} = \frac{R^2 \alpha}{2} \tag{2.9}$$

where R is the cavity (circle) radius.

[1] The normal deviation angle is defined as the maximum angular deviation between the normals of the faceted triangles and the normals of the true surfaces they represent.

- For the calculation of A_{s2} we can consider it the sum of two small triangles. Let's take the AOC one:

$$OA = R \tag{2.10}$$

$$AC = R\sin\frac{\alpha}{2} \tag{2.11}$$

$$OC = R\cos\frac{\alpha}{2} \tag{2.12}$$

Then $\frac{A_{s2}}{2}$ is

$$\frac{A_{s2}}{2} = \frac{R^2}{2}\sin\frac{\alpha}{2}\cos\frac{\alpha}{2} = \frac{R^2}{4}\sin\alpha \longrightarrow A_{s2} = \frac{R^2}{2}\sin\alpha \tag{2.13}$$

Therefore we obtain

$$\Delta A_s = \frac{R^2}{2}(\alpha - \sin\alpha) \tag{2.14}$$

Substituting (2.14) into (2.7) we obtain

$$\begin{aligned}\frac{\Delta f_0}{f_0} &\simeq \frac{1}{4U}\mu H^2\alpha\frac{R^2}{2}(1-\frac{\sin\alpha}{\alpha})NL = \\ &= \frac{1}{4U}\mu H^2\pi R^2(1-\frac{\sin\alpha}{\alpha})L\end{aligned} \tag{2.15}$$

and so, by imposing α inside the previous equation, the frequency error Δf_0 due to 3D circular structure representation can be controlled and minimized, of course keeping also in mind the computational resources available.

It is clear that (2.15) requires the knowledge of the field H at the point where the volume is subtracted. In our case this value can be determined through a 2D simulation, as a reference.

2.3 Numerical validation

2.3.1 Mesh error prediction formula application

In the following section we test equation (2.15) on the DTL cell (see Fig. 2.3). The cell has the following specifications, obtained by using a 2D Superfish simulation taken as reference (as described in §2.2.1) and by considering a mean accelerating field $E_0 = 3.04$ MV/m inside it: $U = 0.81$ J, total stored energy inside the cell, $R = 0.2605$ m, cell radius, $H = 3745$ A/m, average magnetic field on the cavity outer wall, $L = 0.289$ m, cell length, $f_0 = 351.266$ MHz, cell operating frequency taken as ground truth.

The frequency error calculation procedure can be summarized as follows:

1. obtain all the needed global specifications with an accurate 2D simulation;

2. insert these reference values, obtained with the 2D simulation, inside equation (2.15) and derive some α values in the way to obtain the estimated frequency error Δf_0;
3. when a satisfactory Δf_0 is chosen (depending on structure tolerances and application) impose the corresponding α value in the 3D simulation in order to obtain electromagnetic results with a controlled frequency error;
4. if the selected α value leads to unreasonable heavy 3D simulation, repeat the previous step with relaxed precision requirements (higher α value, worse 3D representation).

In Table 2.1, for different values of α_i, we report the value of $f_{mesh} = f_0 + (\Delta f_0)_i$ estimated through the semi-analytical formula (2.15) and the correspondent results from full wave HFSS simulations. The agreement is very good.

Table 2.1: DTL cell resonant frequency f_0 obtained through analytical calculation and HFSS simulation for different values of α.

α_i	f_i (analytical) (MHz)	f_i (HFSS) (MHz)
10°	351.88	351.72
5°	351.42	351.272

In Fig. 2.5 the difference in mesh between the use of $\alpha = 10°$ and $\alpha = 5°$ can be observed. The bad representation of the cavity outer wall obtained by using a coarse mesh lead to an unacceptable frequency error and will have an impact on the overall DTL tank simulation both in terms of frequency and field precision.

2.3.2 Equivalent volume method

As stated before, the cavity stem breaks the rotational symmetry and causes a frequency error with respect to the real one. This error can be predicted as detailed in §2.3.1 and a countermeasure can be applied in terms of mesh utilization to represent the model.

A possible alternative approach could be the use of an equivalent stem volume that introduces the same frequency shift without breaking the rotational symmetry [21].

The method adopts a model representing the DTL cell with a "modified stem volume" that correctly accounts for the frequency shift but, not breaking the rotational symmetry, also allows the use of periodic boundary condition to simulate only a cell slice instead of the entire structure. This equivalent volume can be found by relating

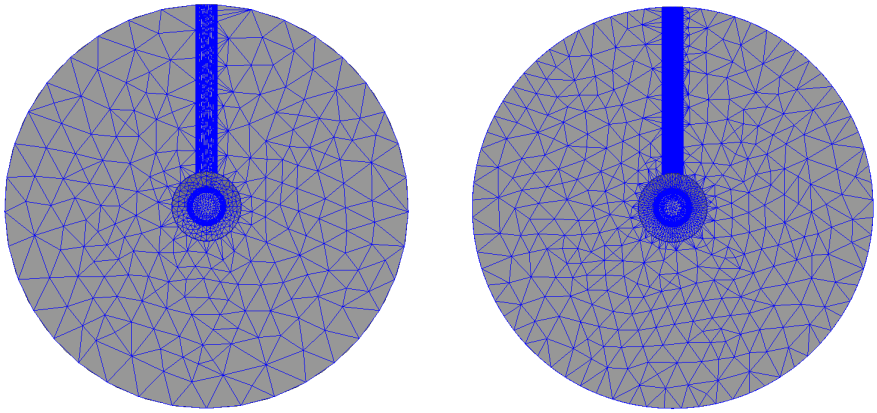

(a) (b)

Fig. 2.5: (a) HFSS cell front face mesh using $\alpha = 10°$. (b) HFSS cell front face mesh using $\alpha = 5°$

the magnetic field at the point where it is subtracted with the average field along the real stem.

Both the real and virtual stem lay in a region with low electric field, E, so the following reasoning is made considering only the unbalance in magnetic field, H, and in particular to correct the frequency shift we require:

$$\int_{\Delta V_{\text{real stem}}} \mu H^2 \mathrm{d}V = \int_{\Delta V_{\text{virtual stem}}} \mu H^2 \mathrm{d}V$$

that can be approximated as

$$\Delta S \underbrace{\int_{\Delta L_{\text{real stem}}} \mu H^2 \mathrm{d}L}_{=H_{line-avg}\Delta L} = \underbrace{\int_{\Delta V_{\text{virtual stem}}} \mu H^2 \mathrm{d}V}_{=H_{V-avg}\Delta V}$$

$$(\Delta S \Delta L)_{\text{real stem}} H_{line-avg} \approx (\Delta V)_{\text{virtual stem}} H_{V-avg}$$

Let's consider Fig. 2.3: here a real stem of radius $r = 14$ mm and height $\Delta L = 215.5$ mm is inserted. If we calculate the average magnetic field along its height, we have a value of $H_{line-avg} \simeq 1194$ A/m. The rotational symmetric volume that will represent the real stem could be of any form: for simplicity, let's take a simple triangular area and consider a volume obtained by rotating this area around the cell axis. As second step, by knowing that in a DTL cell the magnetic field has its maximum concentrated practically only in the center of the drift tube outer wall at coordinates $r = r_{DT}$, $z = L/2$ (or $z = -L/2$, see reference system of Fig. 2.3), a simulation has been performed and it has been found that a proper magnetic field value at these coordinates is $H_{V-avg} = 9417$ A/m. The objective of this method is to

find the exact dimensions of the "equivalent volume" in the way that, when weighted with H_{V-avg}, it has the same frequency effect of the real stem volume weighted with $H_{line-avg}$, that is:

$$\frac{(\Delta V)_{\text{virtual stem}} H_{V-avg}}{\pi r^2 H_{line-avg}} = 1 \tag{2.16}$$

Solving (2.16), we obtain $(\Delta V)_{\text{virtual stem}} \simeq 78000$ mm^3. Now, by arbitrarily fixing the triangle height $h = 25$ mm, by simple mathematical steps the triangle base can be determined in the way to obtain the proper triangle volume. In our case, the determined triangle base is $b = 9.3$ mm and, by making a full 3D simulation with these volumes as shown in Fig. 2.6, we found an operating frequency $f_0 = 351.276$ MHz that is in excellent agreement with that found with the mesh error prediction formula and reported in Table 2.1 for $\alpha = 5°$.

The application of the equivalent volume method has been applied on the DTL cell in a HFSS simulation, but the method can also be applied in 2D simulations.

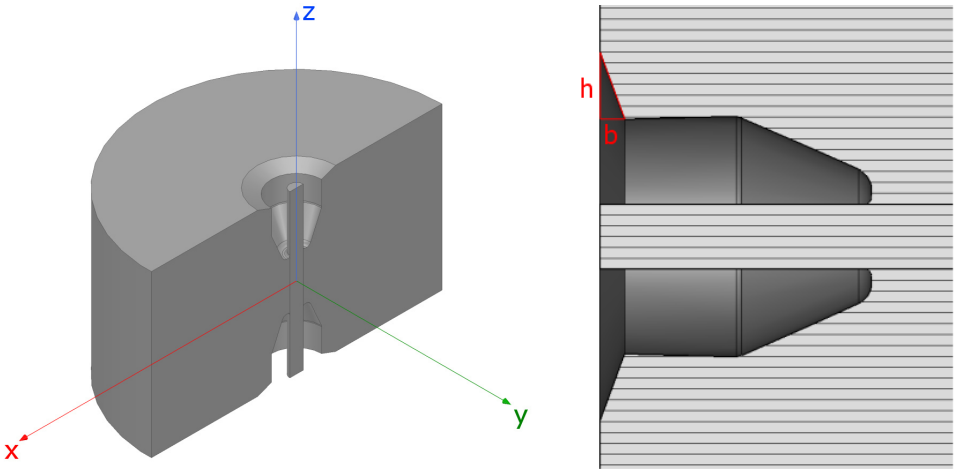

Fig. 2.6: Application of the equivalent volume method to half DTL cell in HFSS. A normal deviation angle of $\alpha = 5°$ is also used to ensure accurate results.

NOTE: in the application of this method one has to be careful when inserting the equivalent volume. In the case of the DLT cell we are interested only in the accelerating on axis electric field, that is mainly located between the two drift tube halves. So, the electric field is not affected from the insertion of a triangular solid equivalent volume instead of the real stem. But this could not be the case if one considers different geometries.

2.4 Final considerations

The numerical resolution of a complex model like the DTL cell previously introduced is clearly not a simple task, especially considering a whole tank composed of dozens of these cavities. In §2.2.1 and §2.3.1 we applied two methods to simulate such structure and obtain accurate results:

1. perform a 2D simulation without directly taking in account stem geometry (due to the rotational symmetry that the 2D model needs to have in order to be solved)
2. analytically calculate the frequency error Δf_0 by taking into account a proper 3D simulator quality mesh parameter, the so called *normal deviation angle* or α.

The first method has the advantage of using a 2D simplified model that can be resolved with an extremely fine mesh and, by knowing the stem frequency effect a priori, one can obtain a fairly accurate operational frequency result. The disadvantage is that, by not directly taking into account the stem presence inside the model, the electric field obtained with the 2D simulation could be inaccurate (depending on the considered model).

The second method has the advantage of an accurate frequency error control, so one can get accurate results in 3D simulators both for frequency and field (because in the 3D simulation the real stem geometry is taken into account). However, if the model is particularly complex, an accurate 3D simulation may require lot of computational resources in order to converge toward the correct results.

A third approach, the equivalent volume method described in §2.3.2, combines the previous methods, taking both advantages of the two. It consists in the utilization of *equivalent volumes* for the model parts that don't possess rotational symmetry around the cavity axis (the stem in our case). This third method can be used in 3D simulations.

3

Fabrication, assembly and experimental validation of ESS DTL tank 2 cold model

The numerical method described previously have been adopted for the tuning of a 'cold model' of the ESS DTL tank 2. This prototype has also been constructed with the following purposes: 1) to test the bead-pull measurement setup necessary for field measurements, 2) to develop specific software for data acquisition/post processing and 3) to develop a field stabilization/tuning procedure, necessary to counteract random perturbations that can affect the quality of the acceleration process. The entire procedure, performed at INFN-LNL from November 2017 to November 2018, can be divided into the following steps:

- **Model assembly and alignment**. In this step, every cavity module (four in total) has been positioned on its sled and each drift tube, including its stem for mechanical support, has been aligned by the use of a laser tracker. When all the drift tubes have been aligned, the four cavity modules have been connected together and the cavity has been closed with two flanges.
- **Axial electric field measurement setup**. In this step, the setup necessary for the measurement of the axial electric field (by the use of the bead-pull technique, see 3.2) has been mounted on the tank 2 cold model: two support plates have been attached to the cavity low and high energy ends and a thin dielectric wire has been passed along the structure axis through a hole made on the closure flanges. The wire runs for the entire tank length. A little metallic bead has been mounted on the wire, whose movement is controlled by a motor through a specifically created LabView program that also acquires the scattering parameters (i. e. the desired field measurement) at every bead step.
- **Data analysis and post processing**. In order to analyze the bead-pull measured data, a post processing program has been created using MATLAB. The program deals with the following issues: a) correction of the acquired phase measure drift due to temperature change, wire loosening, etc; b) conversion of the acquired phase

measure into axial electric field; c) calculation of tilt sensitivity curve, necessary to evaluate field stability.

- **Stabilization procedure**. In order to make the accelerating field uniform (flat) along the cavity axis and to make it robust against random perturbations or manufacturing errors, a *field stabilization* technique is required. The stabilization is possible through the use of the so called post-couplers. A stabilization procedure has been carried out on the cavity; it consists of a proper post-coupler insertion and observation of tilt sensitivity as a quality parameter. At the end of the stabilization campaign, an accelerating electric field possessing amplitude within a range of $\pm 5\%$ with respect to its average has been obtained.

3.1 Cold model assembly and alignment

In Fig 3.1 the cold model, complete with its bead-pull setup, can be observed. The initial cavity tuning has been performed by numerical simulations through the use of the previously developed numerical methods (see §2). Cavity operating frequency, with all post-couplers set at initial length $l_{pc} = 190$ mm, and all tuners initially set at zero penetration, is $f_0 \simeq 351.2$ MHz, in very good agreement with the simulation results and with ESS requirements.

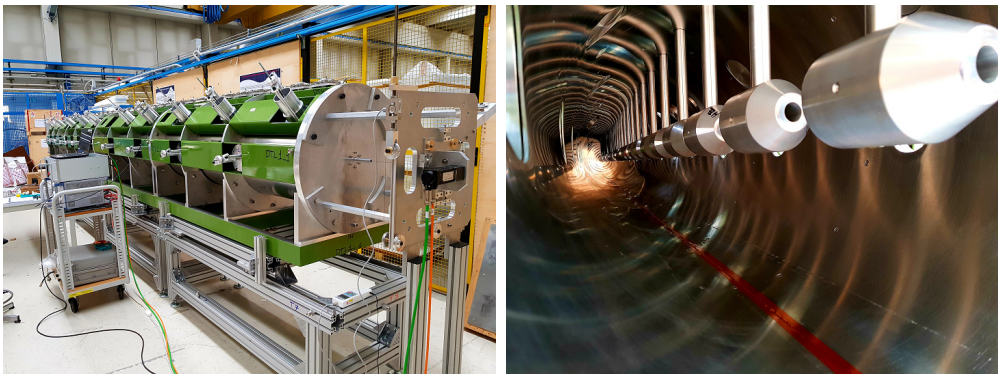

(a) (b)

Fig. 3.1: ESS DTL tank 2 cold model: (a) assembled model comprehensive of post-couplers and tuners; (b) internal view of the cavity with mounted drift tubes.

Drift tubes and tank modules alignment has been done by the use of a laser tracker (see Fig 3.2). At the end of alignment process, all the pieces composing the model have been assembled with a precision equal to $\simeq 0.1$ mm with respect to the fiducial coordinates. This precision has been found sufficient for RF tuning purposes.

(a) (b)

Fig. 3.2: DTL tank 2 assembly steps: (a) drift tubes and modules alignment; (b) the used laser tracker with its control laptop.

3.2 Bead pull measurement technique

It is known that perturbations of a simple oscillator resulting in a change in the system stored energy will generally result in a resonant frequency shift [18]. For a cavity on resonance, the electric and magnetic stored energies are equal. If a small perturbation is made on the cavity wall, this will generally produce an unbalance of the electric and magnetic energies, and the resonant frequency will shift to restore the balance.

The Slater perturbation theorem describes the shift of the resonant frequency when a small volume ΔV is removed from the cavity of volume V.

The general result that relates the frequency shift with the perturbation applied, is

$$\frac{\Delta\omega_0}{\omega_0} = \frac{\int_{\Delta V}(\mu_0 H^2 - \epsilon_0 E^2)\mathrm{d}V}{\int_V(\mu_0 H^2 + \epsilon_0 E^2)\mathrm{d}V} = \frac{\Delta U_m - \Delta U_e}{U} \tag{3.1}$$

where U is the total stored energy inside the cavity, ΔU_m and ΔU_e are the time average of the stored magnetic and electric energies removed due to the presence of the perturbing object. The frequency increases if the perturbing volume is subtracted where the magnetic field is large and it decreases if the electric field is large where the perturbing volume is subtracted.

This result is easier to remember if one identifies a decrease in the effective inductance where the magnetic field is large and an increase in the effective capacitance where the electric field is large.

The Slater theorem provides the basis for field measurements in cavities. If a small bead is inserted into the cavity, the perturbation shifts the resonant frequency. For a spherical bead of volume ΔV, the frequency shift is given as a function of the unperturbed field amplitudes E and H, which are assumed to be constant over the bead, by

$$\frac{\Delta\omega_0}{\omega_0} = -\frac{3\Delta V}{4U}\left[\frac{\epsilon_r - 1}{\epsilon_r + 2}\epsilon_0 E^2 + \frac{\mu_r - 1}{\mu_r + 2}\mu_0 H^2\right] \tag{3.2}$$

where ϵ_r and μ_r are the dielectric constant and magnetic permeability of the material relative to vacuum.

If a dielectric bead is chosen, then $\epsilon_r > 1$ and $\mu_r = 1$. So the previous equation reduces to

$$\frac{\Delta\omega_0}{\omega_0} = -\frac{3\Delta V}{4U}\frac{\epsilon_r - 1}{\epsilon_r + 2}\epsilon_0 E^2 \tag{3.3}$$

If one choses a spherical bead of radius r, then $\Delta V = \frac{4}{3}\pi r^3$.

$$\frac{\Delta\omega_0}{\omega_0} = -\frac{\pi r^3}{U}\frac{\epsilon_r - 1}{\epsilon_r + 2}\epsilon_0 E^2 \tag{3.4}$$

The quantity $F = \pi r^3 \frac{\epsilon_r - 1}{\epsilon_r + 2}\epsilon_0$ is called form factor of the spherical bead. This quantity is function of the bead volume and the material chosen for it.

The bead-pull measurement system, visible in Fig 3.3, consists of a small dielectric or metallic bead, attached to a thin dielectric wire, being pulled through a cavity while the electric and/or magnetic field measure versus position is performed. A step motor and a pulley system guide the motion of the bead through the cavity while a VNA is used to take the RF measurements. A LabView program has been created in order to coordinate the step motor's movement, acquire data via the VNA and save the measure.

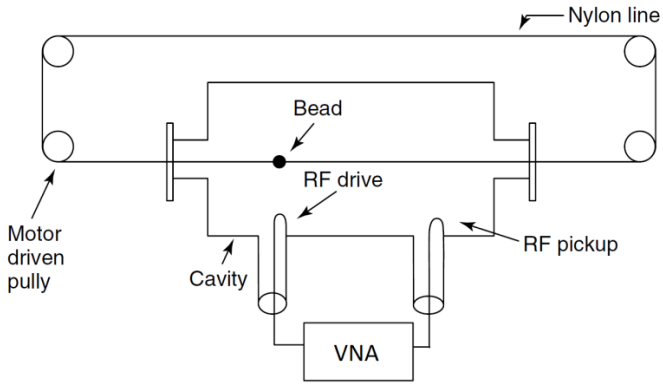

Fig. 3.3: Typical bead-pull setup for field measurement: a small dielectric or metallic bead, attached to a thin dielectric wire, is pulled through a cavity while the electric and/or magnetic field measure versus position is performed.

3.2.1 Field measurements through phase shift

For small perturbations, shifts in the peak of the cavity response are hard to measure. For this reason, usually shift in the phase of the considered mode are much easier to measure.

A way to measure the field is the phase measurement of the $|S_{21}|$ parameter of the mode being considered, at any bead position. From the phase shift measurement one can determinate the field value at every sampled point.

$|S_{21}|$ can be obtained as [22]:

$$|S_{21}| = \frac{2\sqrt{\beta_1\beta_2}}{(1+\beta_1+\beta_2)+j\gamma(f)} \tag{3.5}$$

where

- $\gamma(f) = jQ_L\left[\frac{f}{f_0} - \frac{f_0}{f}\right]$ is called detuning factor of the cavity. On resonance, $\gamma = 0$;
- f_0 is the cavity resonance frequency;
- f is the VNA drive frequency;
- β_1 and β_2 are the resonator-to-guide coupling factors, respectively for the input (RF drive) and the output (signal pickup) guide;
- $Q_L = \frac{\omega_0 U}{P_0+P_{ext}}$ is the loaded quality factor, defined as the ratio, at resonance, of cavity stored energy to power dissipated on the cavity walls P_0 plus emitted or externally dissipated power P_{ext}. It can be rewritten in the form $Q_L = \frac{Q_0}{1+\beta_1+\beta_2}$;
- $Q_0 = \frac{\omega_0 U}{P_0}$ is the quality factor proper of the cavity, unloaded by the external resistance;
- $P_0 = P_{in} - P_r - P_{out}$, where P_{in} is the input power at RF drive (default 1dBm for VNAs), P_r is the reflected power and P_{out} is the transmitted power at RF pickup.

The phase of S_{21} is the argument of complex part:

$$\phi(S_{21}) = -Q_L \left[\frac{f}{f_0} - \frac{f_0}{f} \right] + \phi_{ref} \tag{3.6}$$

The term ϕ_{ref} is a reference phase that takes in account cable lengths and junction effects, both not included in VNA calibration. Obviously this term can be properly set by the user, by inserting a VNA phase offset, when the measurement process begins. So it will be omitted from next calculations. When there is no bead inside the cavity, it can be assumed that $f \simeq f_0$, so there is no phase shift. But when the bead is introduced, the cavity resonance frequency shifts of a value $\Delta f(z)$ and then $f \simeq f_0 + \Delta f(z)$. In this case, supposing that $\Delta f(z) \ll f_0$, it results:

$$\begin{aligned} \Delta\phi(z) &= -Q_L \left[\frac{f_0 + \Delta f(z)}{f_0} - \frac{f_0}{f_0 + \Delta f(z)} \right] \\ &= -Q_L \left[\frac{{f_0}^2 + 2\Delta f(z) f_0 - \Delta f(z)^2 - {f_0}^2}{f_0(f_0 + \Delta f(z))} \right] \\ &\simeq -2Q_L \frac{\Delta f(z)}{f_0} \end{aligned} \tag{3.7}$$

Substituting (3.7) into (3.4), the amplitude of the electric field in function of the phase shift can be obtained, for every z picked sample.

$$-\frac{\Delta\phi(z)}{2Q_L} = -\frac{\pi r^3}{U} \frac{\epsilon_r - 1}{\epsilon_r + 2} \epsilon_0 E(z)^2 \tag{3.8}$$

And finally

$$E(z) = \sqrt{\frac{\Delta\phi(z)}{2Q_L} \frac{U}{\epsilon_0 \pi r^3} \frac{\epsilon_r + 2}{\epsilon_r - 1}} \tag{3.9}$$

Fig. 3.4 shows a typical VNA output after a bead-pull measurement. Reference phase, without bead insertion, is 0 deg. When the bead is inserted and moves along the cavity axis z, it produces a phase shift $\Delta\phi(z)$. By accurately sampling the phase along z axis, and through (3.9), the amplitude of electric field $E(z)$ can be obtained. Obviously, the phase shift does not depend on the field level, but only on the geometric and physical parameters of the cavity, via the Q_L value. **Therefore, the above result is independent on $E(z)$ normalizing factor**.

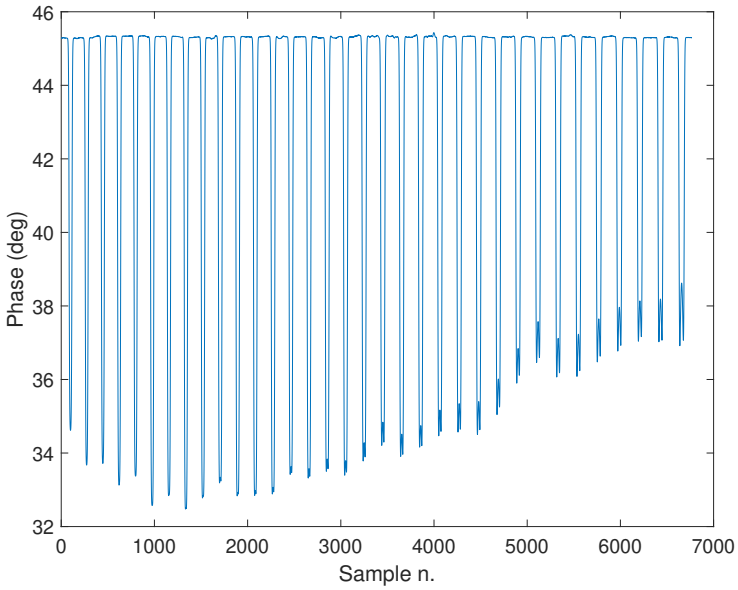

Fig. 3.4: Bead pull measure ($\angle|S_{21}|$ vs bead position) of the operation mode TM_{010} in a DTL cavity.

3.2.2 Perturbator radius estimation

Once the bead material and form have been chosen, it is possible to make an estimation of the required perturbator dimensions. For a spherical dielectric bead, from (3.9) the radius can be written as

$$r = \sqrt[3]{\frac{\Delta\phi}{2Q_L}\frac{U}{\epsilon_0 {E_0}^2 \pi}\frac{\epsilon_r + 2}{\epsilon_r - 1}} \tag{3.10}$$

For an early estimation, some parameters are needed in (3.10): these values can be obtained through 2D or 3D simulation results.

As an example, let's calculate the circular bead diameter for the DTL cell reported in Fig. 3.5, supposing that the maximum phase shift the bead causes when it enters inside the cavity is $10° = \frac{\pi}{18}$ rad (realistic value), and supposing to already know β_1, β_2 (typical values are 0.25).

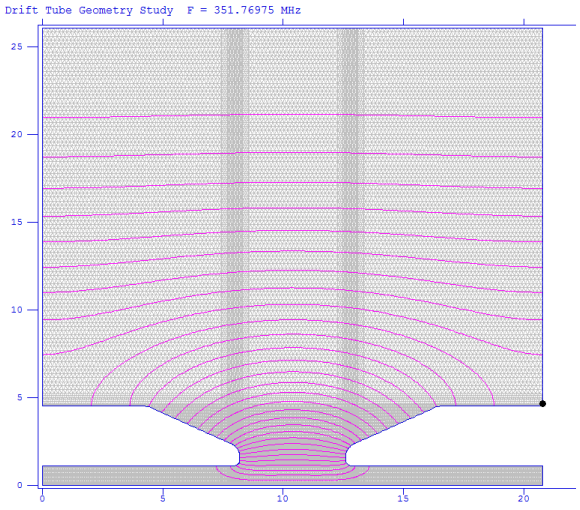

(a)

```
Superfish output summary for problem description:
Drift Tube Geometry Study
ess200.MDT ESS21   1-gap problem
Problem file: C:\Users\Admin\Desktop\Nuova cartella (2)\ESS21.AM  2-23-2017  11:44:40
--------------------------------------------------------------------------------
All calculated values below refer to the mesh geometry only.
Field normalization (NORM = 0):     EZERO =      3.16000 MV/m
Frequency                                =    351.76975 MHz
Particle rest mass energy                =   938.272029 MeV
Beta =  0.2444297          Kinetic energy =      29.351 MeV
Normalization factor for E0 =  3.160 MV/m =    38759.684
Transit-time factor                      =    0.8892598
Stored energy                            =    0.6298209 Joules
Using standard room-temperature copper.
Surface resistance                       =      4.89317 milliOhm
Normal-conductor resistivity             =      1.72410 microOhm-cm
Operating temperature                    =      20.0000 C
Power dissipation                        =      48.1721 kW
Q    =   28897.5          Shunt impedance =      43.128 MOhm/m
Rs*Q =   141.400 Ohm              Z*T*T =      34.105 MOhm/m
r/Q  =   245.554 Ohm  Wake loss parameter =     0.13568 V/pC
Average magnetic field on the outer wall  =      3866.22 A/m, 3.65707 W/cm^2
Maximum H (at Z,R = 0.0,4.5)             =      10674.9 A/m, 27.8796 W/cm^2
Maximum E (at Z,R = 12.6664,1.99206)     =      25.7781 MV/m, 1.39887 Kilp.
Ratio of peak fields Bmax/Emax           =       0.5204 mT/(MV/m)
Peak-to-average ratio Emax/E0            =       8.1576
```

(b)

Fig. 3.5: (a) Drift Tube Linac cell and (b) parameters (Superfish simulation).

The needed parameters are

- $Q_L = \frac{Q_0}{1+\beta_1+\beta_2} = 19265$
- $U = 0.6298209$ J
- $\Delta\phi = \frac{\pi}{18}$ rad
- $E_0 = 3.16$ MV/m (average electric field inside the cell).

Using (3.10) and choosing a dielectric spherical Teflon bead with $\epsilon_r = 2.09$, the bead radius results $r = 3.37$ mm. Of course, if a dielectric material with higher ϵ_r is chosen, smaller bead radius will be obtained.

An example of dielectric bead used for early bead pull measures is shown in Fig 3.6.

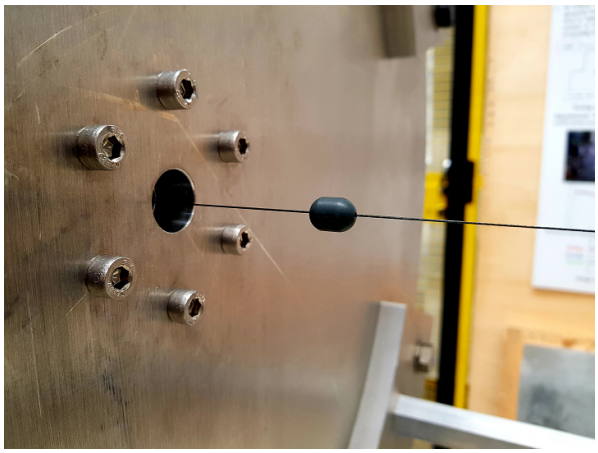

Fig. 3.6: Example of Teflon bead used for bead-pull measures on the ESS DTL tank 2 cold model.

3.2.3 Bead pull setup for tank 2 cold model

Fig 3.7 shows the used measurement setup. Rhode and Schwartz VNA is connected to a motor (central device) that drives the wire through the cavity. The phase shift measurement VS bead position is automated and performed by using a LabView script.

Fig. 3.7: Setup used for bead pull measurements. VNA and motor are controlled through a LabView script that acquires and saves the measures.

3.3 Data analysis and post processing

Once the phase measure is acquired, a necessary number of post processing and data analysis operations are required in order to obtain the cell by cell average accelerating field E_{0i} (where i represents the i-th cell) and to calculate the quality parameters for the successive post-coupler stabilization, such as the tilt sensitivity. In order to exploit these elaboration steps, a MATLAB script has been created and in the following the performed operations will be discussed in detail.

The script performs the following steps:

- import the raw phase data from a measure file;
- corrects the phase drift that could happen during the measure;
- calculates the cell by cell average field E_{0i};
- calculates the tilt sensitivity curve from two perturbed measures;
- evaluates the $TS_n^{'}$ used for the field stabilization procedure.

3.3.1 Phase drift correction

Due to variation in room temperature, wire slippage, ecc, the measured phase can make a drift from its reference value (the zero reference i. e. the phase value measured when the bead enters the cavity). This could lead to inaccurate accelerating field results in the subsequent data processing; in fact, because we know that for the i-th cell $E_{0i} = \frac{V_{0i}}{L_i} = \frac{\int_0^{L_i} E_i(z)dz}{L_i}$, the integral could return inaccurate field values if the zero reference shifts from its value along i-th cell length L_i and in particular along the drift-tube length.

A way to correct the phase drift occurred into a measure could be the use of the information that the field has 0 value inside the drift tubes. An array of correction values has been created; each value is the mean between two points taken in each drift tube interval, where we know that the field is not present (has zero or near-zero value). The i-th correction value is then subtracted to each measured sample of the i-th cell, and this process is performed for every cell of the cavity. In this way the local phase shift is corrected for the i-th cell, i. e. the measure retrieves its correct 0-baseline. Fig. 3.8 shows a measure, before (a) and after (b) the phase correction: it can be seen that the original acquired measure starts with a phase value of about 51.8 deg but, as the bead moves along the cavity axis, this value shifts from the initial one, creating a curve with an incorrect amplitude, especially inside the drift tubes of the final cells. When the phase correction is applied on the measure it can be seen that the correct reference value is bought back for all the cells, so every cell now have

the correct 0 value inside its drift tube and the E_{0i} calculations will return the correct values.

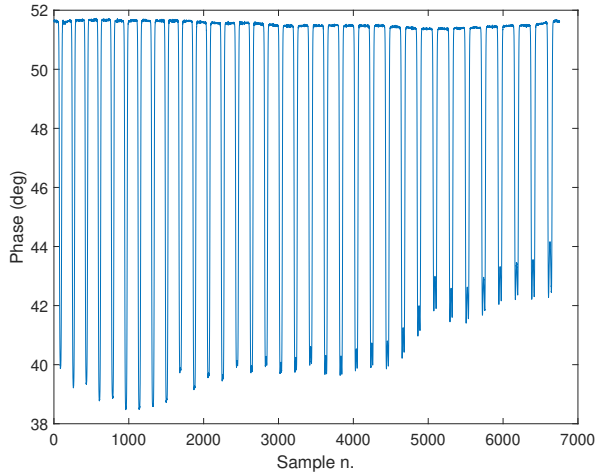

(a)

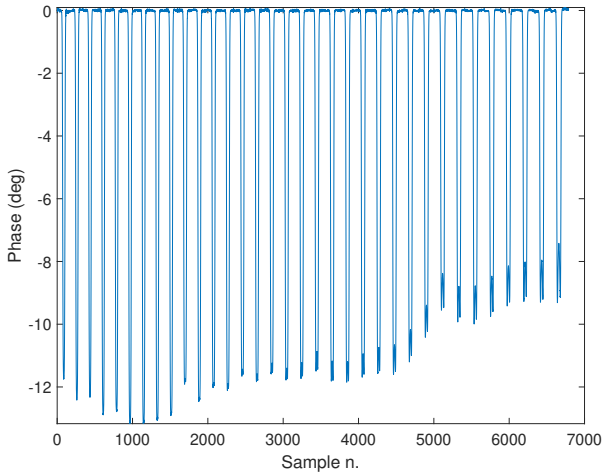

(b)

Fig. 3.8: Phase shift correction: (a) original acquired measure, (b) measure with phase correction applied.

3.3.2 Accelerating field evaluation: integral method vs peak field method

For measurement purposes it is useful to define an average axial electric field amplitude $E_0 = \frac{V(z)}{L} = \frac{1}{L}\int_{-L/2}^{L/2} E(z)dz$ as defined in §1.3.1, where $V(z)$ is the axial RF voltage, L is the cell length and $E(z)$ is the axial field along the cell axis.

In the way to obtain the cell by cell average accelerating axial field E_{0i}, two methods have been compared and used: direct integration of the axial electric field $E(z)$ and a more accurate technique, called Peak Field Method [23].

The Peak Field Method has been extensively studied in [24] and successfully applied to the LINAC4 DTL as reported in [25]. For the stabilization procedure of the ESS DTL tank 2, the formulation used by Khalvati et. al. has been applied and will be reported in the following.

In this technique, the peak field values, or $\mathrm{pfv_i}$ are extracted from the measured phase shift and the relevant average axial field values are obtained by comparing these values with the simulated peak field coefficients, or $\mathrm{pfc_i}$.

In the case when the bead center is located at the peak of the phase shift (i. e. the cell center), for the i-th cell the peak field value is defined as

$$\mathrm{pfv_i} = \oint_{V_{bead}} (E(z))^2 dz \tag{3.11}$$

where i is the cell number and V_{bead} is the bead volume. The $\mathrm{pfv_i}$ are in essence the cell by cell average field values calculated only along the bead length, when the bead is at cell center, where the axial field has maximum amplitude. The peak field coefficients, that can be calculated by using a 2D simulator such as Superfish, are defined as

$$\mathrm{pfc_i} = \frac{\int_{z_{peak}-(l_{bead}/2)}^{z_{peak}+(l_{bead}/2)} E^2(z)dz}{(\int_0^{L_{cell}} E(z)dz)^2} \tag{3.12}$$

The peak field coefficients depend from the cell geometry L_i and the bead length l_{bead}, but not from other perturbations applied inside the cell (tuner insertion, vacuum port, etc) has no effect on these coefficients.

Once both coefficients have been calculated for the i-th cell, the axial field results in

$$E_{0i}^2 = \frac{\mathrm{pfv_i}}{\mathrm{pfc_i} \times {L_i}^2} \tag{3.13}$$

In Fig. 3.9, an example of average axial field obtained by direct integration is compared to the one obtained with peak field method. Both measures refers to the same cavity.

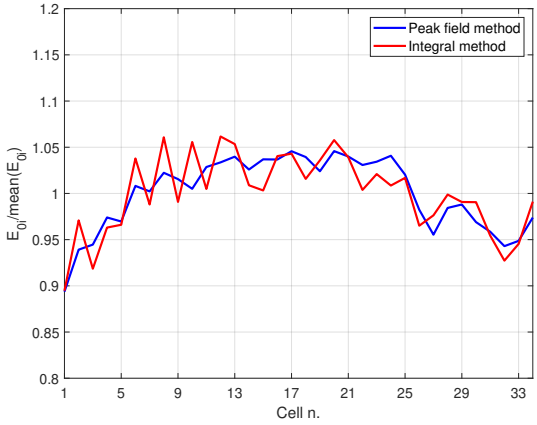

Fig. 3.9: Comparison of average axial field of DTL tank 2 cold model: direct integration (red curve) VS peak field method (blue curve).

Peak field method presents some advantages over direct integration:

- The measure is free of errors that can occur when a complete integration over the entire cell length is performed. In fact, the measure could presents some undesired noise in the lower field value cell areas (for example just outside a drift tube noose) that is taken into account when a direct axial field integration over L_{cell} is performed. By integrating only into an interval placed at the field maximum one can eliminate this inaccuracies without any process error, because only the field at its peak will be experienced by the particle during acceleration.
- The effect of bead length is taken into account because the $\mathrm{pfc_i}$ obtained in simulation uses the real bead length, the one used in actual measurements.

3.3.3 Tilt sensitivity

The actual field distribution of a cavity is affected by fabrication errors and other perturbations. Field tilts and other distortions can occur, and these effects increase as the total cavity length increases [18].

Tilt-sensitivity (TS) is a figure of merit that determines the sensitivity level of the axial field in a perturbed DTL cavity [26]. It can be defined as [25]:

$$TS_i = \frac{1}{\Delta f}(E_{0i}^{he} - E_{0i}^{le}) \tag{3.14}$$

Where E_{0i}^{he} and E_{0i}^{le} refer to axial field values of the i-th cell in the case of a perturbation at the high energy (i. e. at the cavity end cell) and low energy (i. e. at the cavity first cell) of the tank. From the TS curve one can observe the sensitivity level of each cell and investigate the axial electric field stability, or flatness.

In the TS calculation, the first thing to do is to set the frequency ω_{op} of the operation mode, in our case the TM_{010} mode. The cavity is then deliberately perturbed by inserting a simple hollow metal pipe at one end of the structure; doing so, the operating frequency shifts from the nominal value of a quantity $\Delta\omega$. Then, the field can be extracted through a bead pull measurement. The process is repeated when the same perturbation is applied at the other end of the structure. With these two measures, TS can be evaluated.

Fig. 3.10 shows a typical TS curve. If the i-th cell is stabilized, then the effect of any perturbation on the cavity shouldn't affect the local field and so, from TS definition, the more the local field is stabilized, the more the TS curve approaches zero value.

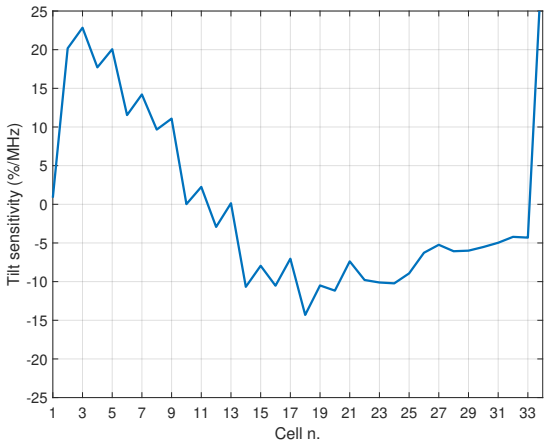

Fig. 3.10: Tilt-sensitivity curve for a particular configuration. For the i-th cell, approaching zero value means a stronger local field stabilization.

Local tilt sensitivity

For our purposes, it is useful to introduce the so called **local tilt sensitivity**, or $TS_n^{'}$, as [25]:

$$TS_n^{'} = TS_{i+1} - TS_i \tag{3.15}$$

Equation (3.15) can be understood as a difference of two TS values, and thus can be thinked as a local tilt sensitivity parameter. In the following the $TS_n^{'}$ will be used as the main quality parameter to check/validate the cavity stabilization level.

3.4 Post-coupler stabilization

In real cavities, there are always different kind of perturbations that may alter the required quality parameters from the design optimal values. Among these perturbations, manufacturing errors cannot be simulated in the design stage. Also, because of variation in cell length, DTL needs to be simulated in total, not in cells. Therefore, optimization of a whole DTL using 3D simulations is not quick and straightforward. Hence, it is interesting to learn how one can stabilize the axial field with respect to an unknown distributed group of perturbations [25].

Post-couplers are the solution used for stabilization of the accelerating mode (the TM_{010} mode) in DTL cavities, by applying the resonant coupling method, as will be explained in §3.4.1. In this case the resonant coupling elements are internal metallic rods (the post-couplers), which extend from the outer cavity wall towards the drift tube, without touching the latter [27]. Fig. 3.11 shows the tuners and the post-couplers used with the tank 2 cold model. The post-coupler arrangement for the tank 2 is shown in Fig. 3.12.

Fig. 3.11: Post-couplers (lower photo side) and tuners (upper photo side) used for the RF tuning of the ESS DTL tank 2 cold model.

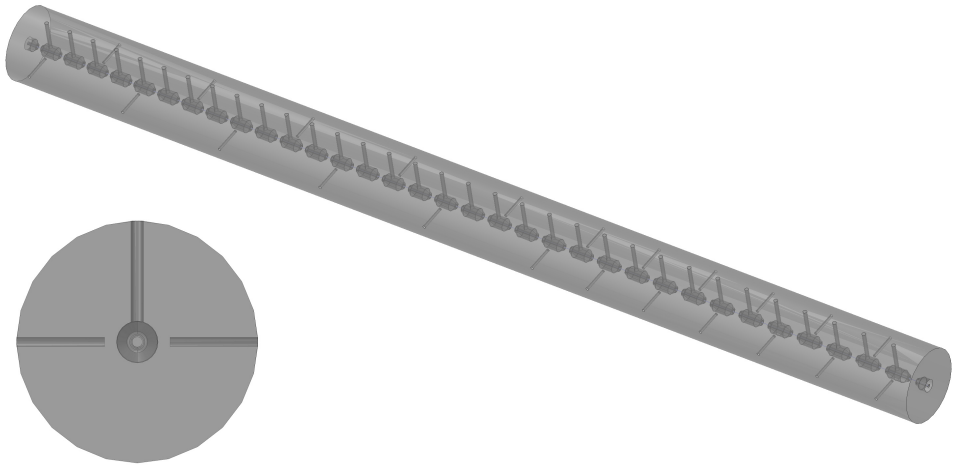

Fig. 3.12: Post-coupler arrangement for ESS DTL tank 2 simulated model: in the image, the low energy side of the tank is on the left, while the high energy side is on the right. The front view is visible in the inset: vertical bars are the stems while the horizontal bars are the post-couplers used for the field stabilization.

In the way to stabilize the field inside the DTL cavity, a campaign of measures has been performed, with the objective of the TS curve flattening.

At first, all the post-couplers have been set to the same equal length of 190 mm. Fig. 3.13 shows low end and high end perturbed axial field as well as the TS curve for this configuration. As one can see the TS varies between $\pm 50\%$, so this configuration is far from good in terms of field stabilization.

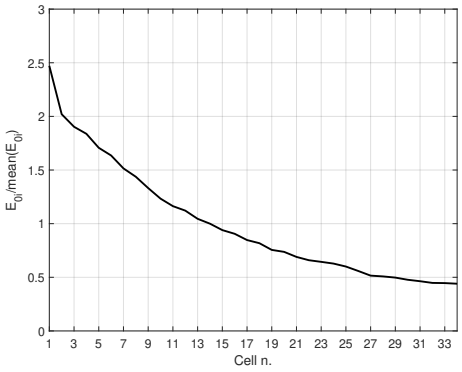

(a) Low energy (LE) perturbed axial field. The perturbator has been inserted inside the gap of the first cell.

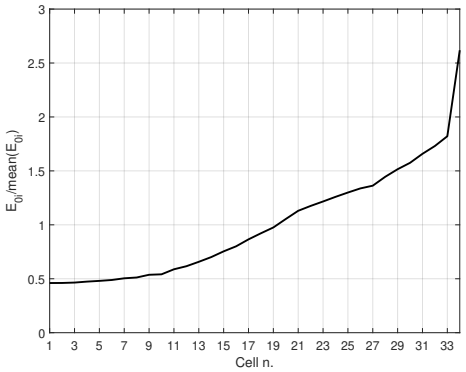

(b) High energy (HE) perturbed axial field. The perturbator has been inserted inside the gap of the last cell.

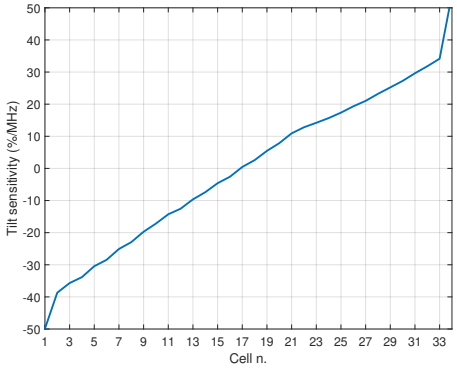

(c) Tilt-sensitivity.

Fig. 3.13: Post-couplers with $l_{pc} = 190$ mm: perturbed fields and tilt-sensitivity.

3.4.1 Resonant coupling

From the theory of the coupled oscillators ([18]-pag. 99) it can be seen that a cell array of oscillators, such as the DTL cavity, can operate in three different modes that have the following normal-mode eigenfrequencies Ω_q defined as follows:

- the 0-mode, where all oscillators have zero relative phase difference

$$\Omega_0 = \frac{\omega_0}{\sqrt{1+k}} \tag{3.16}$$

- the $\pi/2$ mode

$$\Omega_1 = \Omega_0 \tag{3.17}$$

- the π mode

$$\Omega_2 = \frac{\Omega_0}{\sqrt{1-k}} \tag{3.18}$$

where Ω_0 is the resonant frequency of the individual oscillators if they were uncoupled and k is the coupling constant between cells. All the other modes have frequencies between the 0 and π mode frequencies. The field distribution of the three modes, with respect to its phase, is shown in Fig. 3.14 for a seven-cell cavity. When operating in the 0-mode, there is zero-degree phase shift from cell to cell, so fields in adjacent cells are in phase: this is the classical operation mode of the DTL. When operating in the π-mode, there is 180-degrees phase shift from cell to cell: this mode is usually employed in superconducting cavities. The $\pi/2$-mode operates with 90-degrees phase shift from cell to cell and in practice the structure becomes bi-periodic, with a set of accelerating cells and a set of coupling cells. As we will see later, this is the preferred mode for long multicell structures because of the good field stability of this operation mode.

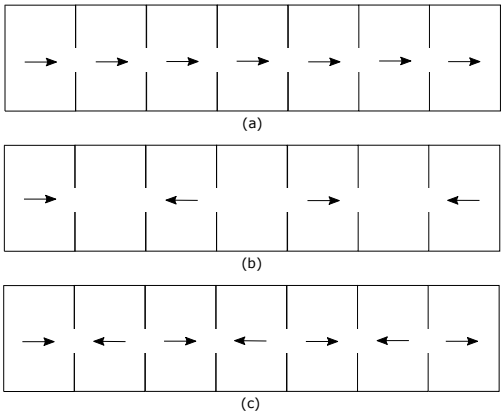

Fig. 3.14: Field distribution of the (a) 0-mode, (b) $\pi/2$-mode and (c) π-mode for a seven-cell cavity.

From the perturbation theory it can be demonstrated that the $\pi/2$ mode is different from the others and has unique properties that are advantageous if we force the accelerating cavity to operate in such mode.

As an example, Fig. 3.15 shows the dispersion diagram of a system composed by seven oscillators. The permitted frequencies of the system are those found on the depicted curve. It can be seen that there are 7 modes, which increases when other oscillators are inserted into the system: the more cells (oscillators) are inserted, the more modes will be present, the more they will become closely spaced into the diagram. This leads to the problem that, for a given set of oscillator errors, modes that are closer together in frequency contribute larger perturbations to the fields than modes that are farther apart and from Fig. 3.15 it can be seen that the spacing

between the 0-mode (or the π-mode) and the closest mode is small because at that point the dispersion curve slope is almost zero. Little changes in the frequency of the operating mode (due for example to machining errors) forces the system to introduce components from the adjacent modes, perturbing the characteristics of the operating one.

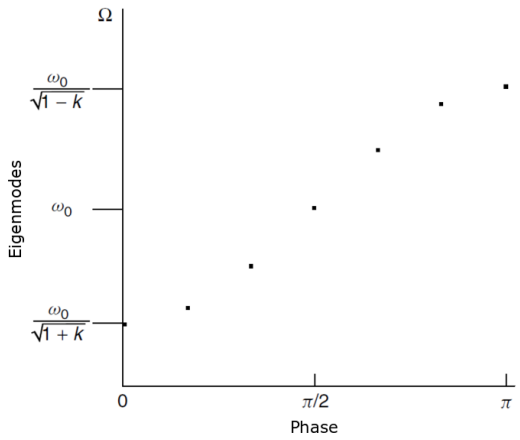

Fig. 3.15: Dispersion diagram (frequency vs. phase) of a system composed by seven oscillators.

On the contrary, the spacing between the $\pi/2$-mode and the closest modes is large because at that point the dispersion curve has a sharper slope. By simple field measurements it can be seen that the two modes adjacent to the $\pi/2$-mode (the perturbing modes) have the same field distributions (they are symmetric), so an error in the chain of resonators working in the $\pi/2$-mode will be compensated thanks to the symmetric components of the modes higher or lower in frequency.

When a perturbation is introduced into the system, the $\pi/2$-mode has some key advantages that can be evaluated from the perturbation theory [18](pp. 101-104), [28]:

- the frequency errors of the single cavities when a frequency perturbation is applied to them affects the whole system, in terms of field amplitude, less than for the 0 and π-modes which in contrast are very sensitive to frequency errors;
- in the $\pi/2$-mode, the power dissipation on the metallic walls into one cavity does not produce any phase shift in the adjacent cells (called power-flow phase shift), while the phase shift is present for 0 and π-modes.

In general, the perturbation theory demonstrates the sensitivity of the 0 and π modes to oscillator frequency errors and power flow along the oscillator chain: the

frequency errors cause distortions of the nominally uniform field amplitudes and the power flow along the system causes relative phase shifts between adjacent oscillators.

As said, the $\pi/2$ mode is very insensitive to these errors, so its properties can be suitable in terms of overall field stability in an accelerating cavity, especially one with a large number of cells.

To retain the advantages of the $\pi/2$ mode in a DTL cavity, one could think to insert a second chain of 'coupled cavities' into a system of accelerating cavities, to obtain a structure with the field as in Fig. 3.14. Half of the cavities are excited (the accelerating cavities) and half are not (the coupling cavities). A bi-periodic chain of oscillators is formed in this way: the accelerating cavities resonates with frequency ω_1 and the coupling cavities resonates with the frequency ω_2. If the two frequencies does not match, a stop band will open into the dispersion diagram as depicted in Fig. 3.16.

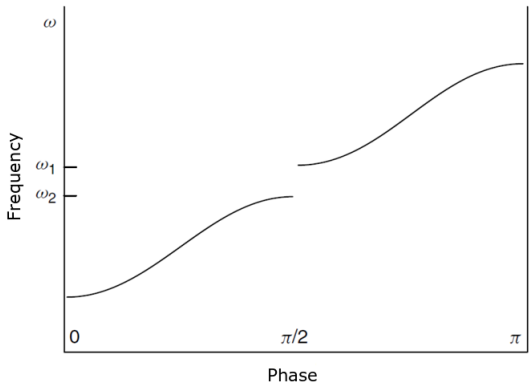

Fig. 3.16: Dispersion curve of a system composed by two set of oscillators. If the resonating frequencies of the two sets of oscillators do not match, a stop band opens in the curve.

In general there are two branches, which are called the lower and upper pass-bands. Between them is the stop-band, within which there are no normal-mode solutions. Because the stop-band opens at the $\pi/2$ mode point, the advantages of this mode over the other two vanishes if the stop-band is not closed. When the system is tuned in the way that $\omega_1 \simeq \omega_2$, the discontinuity is removed and the dispersion curve at the *confluence* point changes to produce a non-zero slope, similarly to the one of a periodic structure.

A practical way to make a cavity working in the $\pi/2$ mode could be the insertion of unexcited cells between excited ones, as seen in Fig. 3.14. This configuration does not lead to a high shunt impedance, because with the fields concentrated in only half of the available space, the net power dissipation is larger than for the 0 or π modes,

where all of the cells can contribute acceleration to produce the same energy gain. More practical ways to obtain better performances (high shunt impedance) are the shortening of the coupling cells with respect to the accelerating ones (this will not affect the TM_{010} resonating frequency because it depends on the cavity radius, not its length) or to removing the coupling cells from the beam line, leaving the beam axis completely composed of excited accelerating cells, as in the case of Coupled Cavity Linac (CCL) depicted in Fig. 3.17. Another possibility, usually employed in the DTL cavity, is the introduction of a second chain of resonator in the form of metallic bars that extends from the cavity wall to the drif-tube wall: the so called post-couplers (see Fig. 3.11). The post-coupler resonator chain introduces a second curve into the dispersion diagram, as explained earlier and the first objective in the DTL stabilization procedure is closing the stop-band by a cavity tuning that allows the confluence of the 0-modes of the two chain of resonators. All of these solutions retain the unique properties of the $\pi/2$ mode of the periodic cavity chain, and provide high shunt impedance values, that is a characteristic of the 0 or π modes.

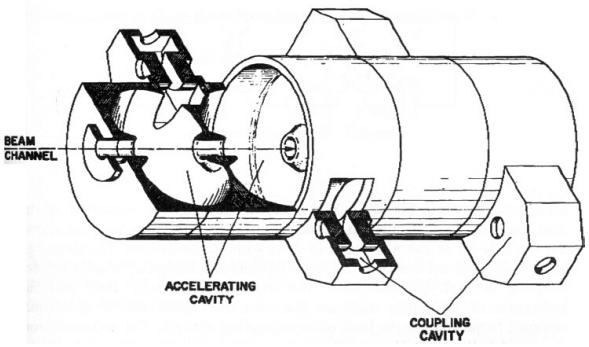

Fig. 3.17: Sketch of a Coupled Cavity Linac (CCL). Accelerating and side coupling cells are visible.

3.4.2 Stabilization procedure

It is now clear that the goal of the stabilization procedure is the reaching of the confluence point between the transverse magnetic mode (TM) passband and the post-coupler mode (PC) passband in the way to utilize an accelerating mode that possesses the perturbation insensitivity of the $\pi/2$ mode, i. e. to exploit the mutual error cancellation between the TM_{011} mode and the PC1 mode. However, because the DTL cell lengths increases with the relativistic velocity β, it is necessary to obtain the correct stabilization length for every single post-coupler along the cavity.

To reach a good stabilization profile for the axial field, a few hundred of measures have been performed.

In the following, the stabilization procedure will be detailed and experimental results will be presented.

The procedure can be divided into the following steps [25]:

1. set all post-couplers to the same initial length such that the post-coupler passband approximately closes in confluence with the cavity mode passband (see §3.4.3). This point is reached when the first post-coupler mode PC1 is as much in frequency below the TM_{010} mode as the TM_{011} mode is above;
2. perform a first perturbated cavity measure and analyze the tilt sensitivity;
3. measure the resonance length of all the post-couplers of one cavity side (left or right cavity side). Move each post-coupler until the post-coupler mode is in full resonance with the TM_{010} mode. Return the post-coupler to the previous length and continue with the next post-coupler on the same side;
4. calculate the stabilization lengths of all the post-couplers of the cavity side taken into account by using the resonance lengths data: the objective, for the n-th post-coupler, is to find a point where the local tilt sensitivity, or $(TS^{'})_n$ have a value near to the 0 value;
5. set all post-couplers to the calculated values and measure the tilt sensitivity again;
6. repeat the procedure for the other cavity side.

3.4.3 Cavity confluence

The general approach of using resonant oscillators as coupling elements to stabilize the field distribution of a multicell standing-wave cavity is called resonant coupling. Because of the existence of a second resonator chain, the structure dispersion curve has now two pass-bands, separated by a stop-band. If the cavities are tuned in order to remove the stop-band, the structure gets the desired $\pi/2$ mode properties. Such a

joining up of two pass-bands is called confluence. The modes that are joined may be either the 0 or the π modes [29].

What happens as a result of confluence is that the tuning process improves the power flow, which is directly related to the local mode spacing. The creation of a finite slope where the pass-bands join, produces the desired increased mode spacing at the operating point, and usually this procedure leads to a symmetrical or nearly symmetrical spacing between the nearest modes. The symmetry produces a first-order cancellation of the error-induced contributions from the nearest modes according to perturbation theory (see [18]-chapter 4).

It is found experimentally that if the azimuthal positions of sequential post-couplers is alternated by 180 degrees from one side of the drift tubes to the other, the post-mode passband is widened, resulting in a larger mode spacing near the accelerating mode at confluence, and a better-stabilized structure.

Here we discuss the stabilization procedure for the tank 2 DTL cavity of the ESS project.

The first thing done in the way to obtain tank 2 stabilization has been the search of the confluence point. In this phase, all the post-couplers are moved together of the same length and the distance of the first cavity mode (the TM_{011}) and the first mode (the PC_1) from the cavity 0-mode is observed. When the two modes are found at the same distance from the cavity 0-mode, the confluence point is reached.

We started with all the post-couplers at a length of 190 mm, then moved simultaneously all of them of the same amount until reaching the point of confluence, in the presented case occurring when all the post-coupler lengths are equal to 175.2 mm. The confluence can be easily controlled by checking the three modes of interest on the VNA, as shown in Fig. 3.18; it can be clearly seen that the PC_1 and the TM_{011} modes are equally distanced from the TM_{010} mode. The point of confluence can also be spotted by observing the post-coupler 1-mode (PC_1) and the cavity 1-mode (TM_{011}) symmetry from the corresponding phase measures, as seen in Fig. 3.19.

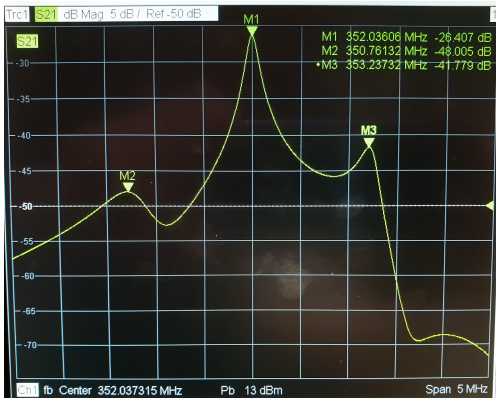

Fig. 3.18: Photo of the VNA screen: cavity 0-mode (TM_{010}) is marked with M1, cavity 1-mode (TM_{011}) is marked with M3 while post-coupler 1-mode (PC_1) is marked with M2. The cavity reaches the confluence point when all the s are inserted of 175.2 mm.

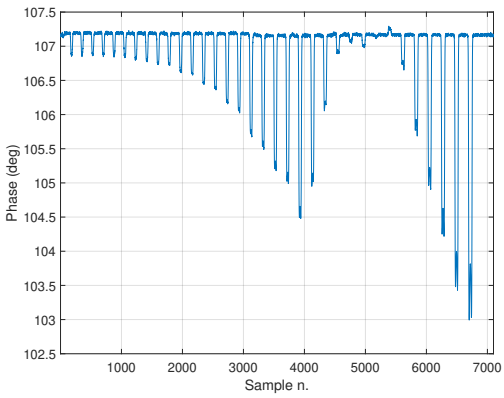

(a) PC_1 mode, $f_{-1} = 350.761$ MHz

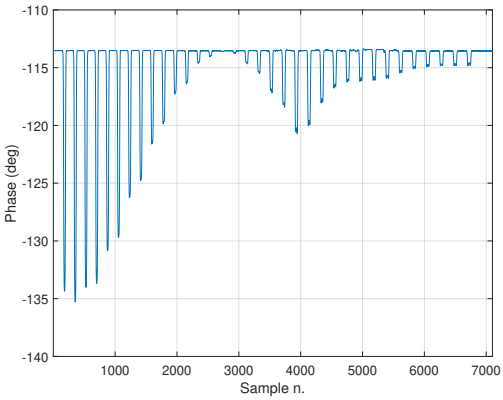

(b) TM_{011} mode, $f_1 = 352.036$ MHz

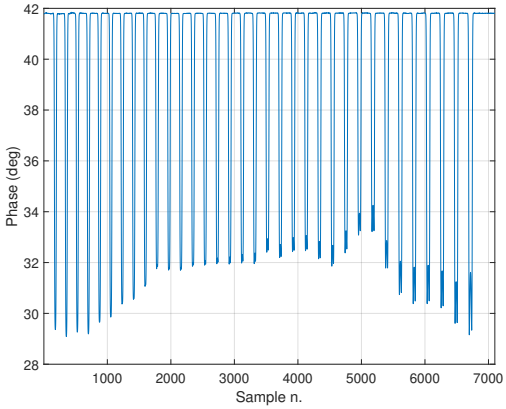

(c) TM_{010} mode, $f_0 = 353.237$ MHz

Fig. 3.19: Phase measures of the post-coupler 1-mode (a), cavity 1-mode (b) and cavity 0-mode (c). The confluence can be observed from the symmetry of the first two modes.

3.4.4 Post-coupler resonance lengths

After the confluence point evaluation, the search for the resonance lengths for the post-couplers of the even side of the DTL cavity (post-couplers 2, 4, 6, 8, etc) has been started. At first, each post-coupler of the even cavity side has been inserted starting from its reference length of 175.2 mm. For each post-coupler, a curve of TM_{010} operating frequency vs. PC length has been evaluated.

For example, let's consider post-coupler 2. Moving the 2-nd post-coupler leads to a frequency change in the TM_{010} mode and, when the PC_1 mode confluences with the TM_{010} mode, the resonance passes through a point of strong variation; at the same point, the $TS_2^{'}$ relative to the 2-nd post-coupler has a pole where it changes suddenly from positive to negative infinite values. Resonance length curve and correspondent $TS^{'}$ curve for post-coupler 2 are visible in Fig. 3.20.

As said, the more the tilt sensitivity curve approaches the 0 value, the more the cavity is stabilized (more field insensitivity against random perturbations). Because the $TS_n^{'}$ is the **local** tilt sensitivity for the n-th post-coupler, it is clear that the optimum stabilization point for the n-th post-coupler is found when $TS_n^{'}$ approaches 0. In the analyzed case, the optimum stabilization length for post-coupler 2 is found at $l_2^s \simeq 164$ mm.

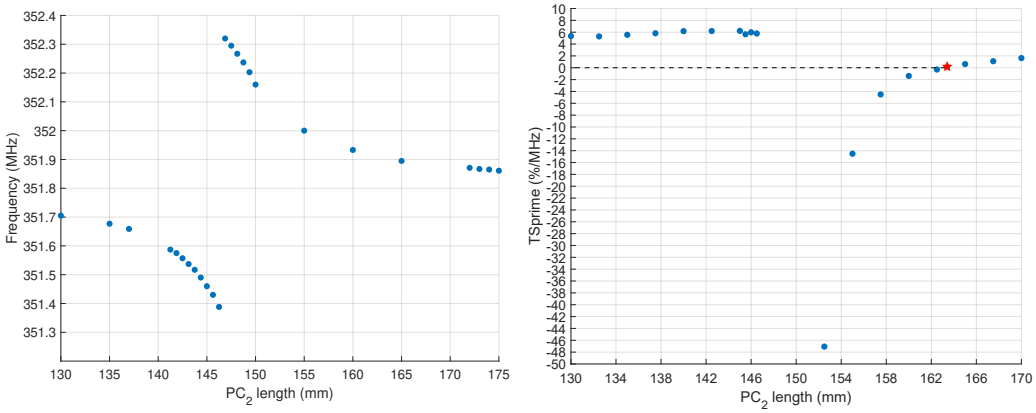

(a) (b)

Fig. 3.20: (a) TM_{010} resonance frequency vs. insertion length plot for the 2-nd post-coupler of the DTL tank 2. The resonance length is found around 147 mm. (b) $TS_2^{'}$ vs. insertion length plot for the 2-nd post-coupler of the DTL tank 2. The curve has a pole around 147 mm, where it changes sign, and reaches 0 value around a length of 164 mm.

Fig. 3.21 shows the resonance length plot of other post-couplers from the even side of the cavity.

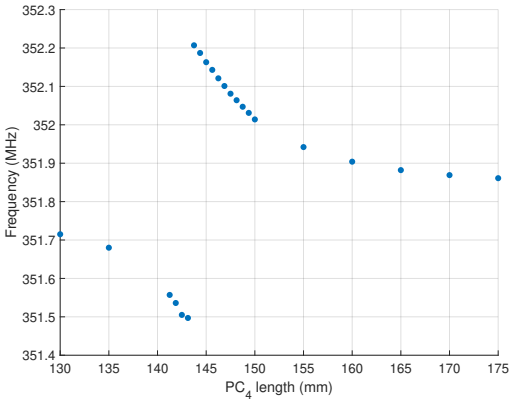

(a) Resonance frequency vs. length plot for the 4-th post-coupler of the DTL tank 2.

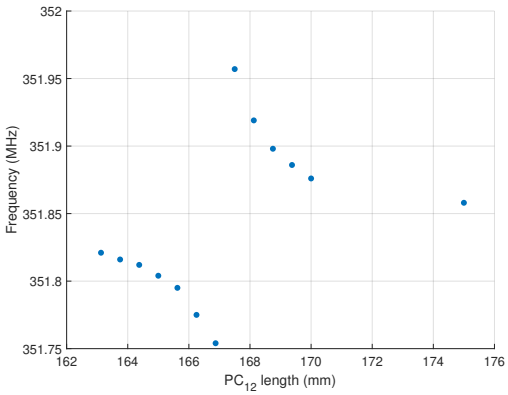

(b) Resonance frequency vs. length plot for the 12-th post-coupler of the DTL tank 2.

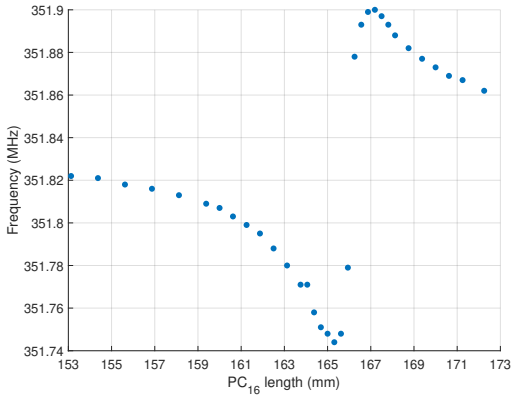

(c) Resonance frequency vs. length plot for the 16-th post-coupler of the DTL tank 2.

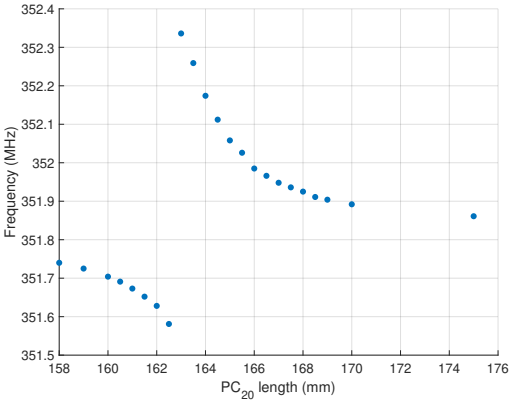

(d) Resonance frequency vs. length plot for the 20-th post-coupler of the DTL tank 2.

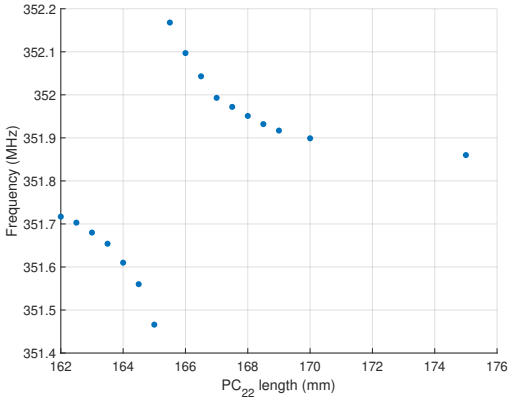

(e) Resonance frequency vs. length plot for the 22-th post-coupler of the DTL tank 2.

Fig. 3.21: Resonance frequency vs. length and equivalent $TS_n^{'}$ vs. length curves for post-couplers 4, 12, 16, 20, 22.

3.4.5 Post-coupler stabilization lengths

After the resonance lengths has been found, the next step has been the calculation of the stabilization lengths l_n^s for the post-couplers residing on the even side of the DTL cavity. The procedure to calculate these lengths can be related to the calculation of the resonance length and the corresponding $TS_n^{'}$ relative to the n-th post-coupler. In fact, by remembering that the pole of the $TS_n^{'}$ curve is found around the resonance length of the n-th post-coupler, by knowing the resonance length one can obtain the starting point for the search of the stabilization length, which will be found at higher post-coupler penetration (on the right of the curve pole), when the $TS_n^{'}$ approaches 0 value.

So, by knowing the initial n-th post-coupler length l_n^r, the stabilization length can be found by calculating few $TS_n^{'}$ values for few lengths. At first, only three values of $TS_n^{'}$ for three lengths are sufficient: from these values one can evaluate the slope of the $TS_n^{'}$ and then, with few other measures, can shrink the interval where the stabilization length resides. For example, if the first three $TS_n^{'}$ return, in sequence, two negatives and a positive value, one can tighten the stabilization length interval to the two last values.

The stabilization procedure by $TS_n^{'}$ minimization required less than a hundred of measures for the even side of the ESS DTL tank 2 cold model. Each calculated $TS_n^{'}$ value requires a TS curve evaluation, composed by two bead-pull measurements of the perturbed cavity, each perturbation applied at the low energy (LE) and at the high energy (HE). In the following the entire procedure will be reported. As operating frequency for the cavity 0-mode, $f_0 = 352.1$ MHz has been chosen in accord to ESS specifications, while the perturbation applied through the hollow core metal cylinder for TS calculation has been chosen equal to 100 KHz. It is known that, when a perturbation is applied in the 'bore' area of the DTL, the operating frequency f_0 decreases because that is an electric field dominated area.

As objective of the stabilization campaign, an axial field range of $\leq \pm 5\%$ around the average value has been chosen for optimal target.

We started from the confluence situation: all the post-couplers with equal length $l_{confluence} = 175.2$ mm. From Fig. 3.22 it can be seen that the tilt sensitivity for this configuration is far from optimal and its range is equal to $\pm 30\%$.

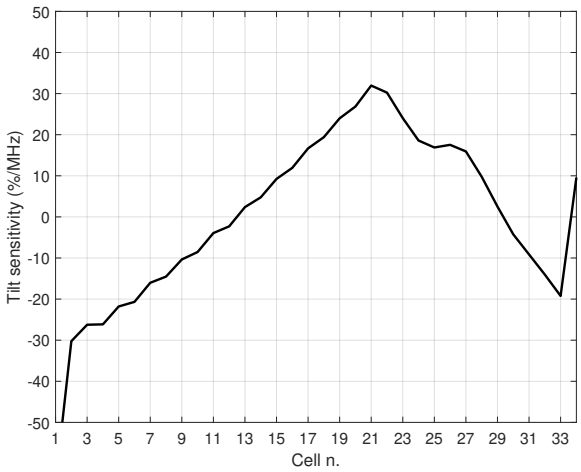

Fig. 3.22: Tilt sensitivity curve relative to the post-coupler configuration with equal penetration length of $l_{confluence} = 175.2$ mm.

Then, by following the $TS_n^{'}$ minimization method, a stabilization campaign has been performed for the even cavity side. The optimal post-coupler stabilization lengths l_{even}^{s}, listed in Tab. 3.1 have been found at the end of the procedure.

Table 3.1: Post-coupler even side stabilization lengths.

PC n.	(value) mm
2	165.2
4	157.5
6	151
8	150
10	148
12	186.3
14	181.2
16	180.9
18	186.1
20	184.1
22	184.3

However, as we can see from Fig. 3.23(a)(b), first impressions suggest that the stabilization procedure is not working properly: we have an unperturbed axial field with a range higher that $\pm 15\%$ and a corresponding tilt sensitivity in the range of $[-60; +80]\%$.

The fact that the field is not stabilized is also visible by the observation of Fig. 3.23(c)(d), where the perturbed axial field (LE and HE) is plotted: it can be noticed that, when a 100 KHz perturbation is applied at LE or at HE ends of the

cavity, the error due to this perturbation propagates to the other cells, resulting in a noticeable field tilt (way outside the desired interval).

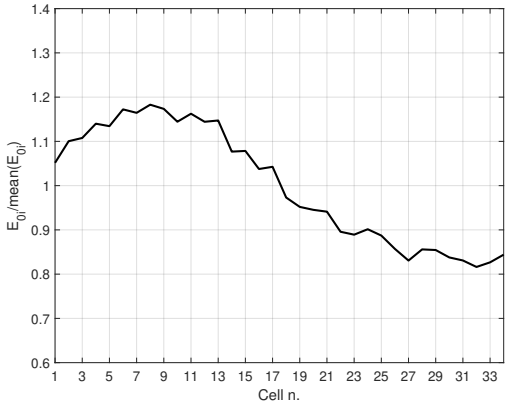

(a) Unperturbed mean axial electric field.

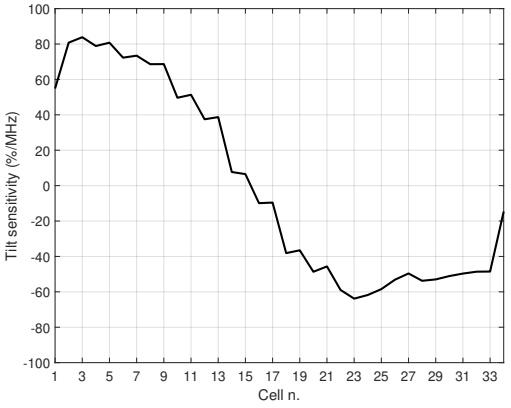

(b) Tilt sensitivity curve.

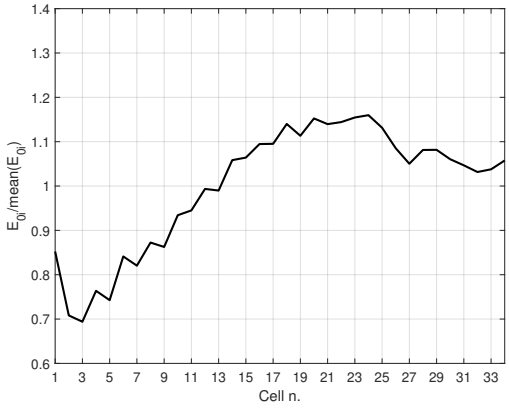

(c) Axial field with low energy (LE) perturbation applied.

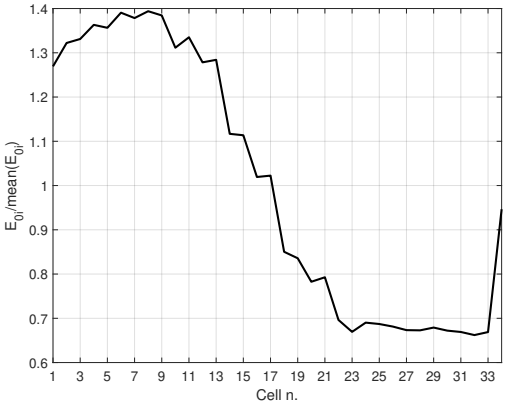

(d) Axial field with high energy (HE) perturbation applied.

Fig. 3.23: Results obtained at the end of the stabilization campaign.

The solution to the previous discrepancy can be found by considering that, since the objective is to stabilize the field along the tank, the influence of neighbouring post-couplers needs to be taken into account.

Let's again consider post-coupler n. From spectral measurements and from circuital considerations [25] it can be easily shown that the movement of the next neighbour post-couplers $n-1$ and $n+1$ results in a strong change of the resonance length l_n^r for post-coupler n. Instead, changing the length of the second next neighbours, i. e. post-couplers $n-2$ and $n+2$, has no influence on l_n^r. One can thus conclude that other post-couplers except the nearest neighbours don't have any effect on $TS_n^{'}$ of the n-th post-coupler.

With this consideration in mind, a *resonance length check* on the odd cavity side post-couplers has been performed: the objective has been to find if some post-coupler stabilization length on the even side leaded to resonance length in the corresponding next neighbours on the odd cavity side. The undesired resonance length can be easily spotted if a subtle movement of that odd from its reference length (175.2 mm) results in a quick confluence (a 'mode exchange') between the TM_{010} mode and the PC_1 mode; this, of course, can be observed in real time on the VNA.

After the resonance length check it has been found that, with the application of the optimal stabilization lengths for the even cavity side, post-couplers 1, 7, 9, 11 on the odd side reached the resonance point due to the next neighbours new lengths. To counteract this effect, the penetration of these post-couplers has been increased in order to drive them away from their resonance length. In particular, after few attempts, the lengths have been set as follows: $l_1 = 183$ mm, $l_7 = 180$ mm, $l_9 = 180$ mm, $l_11 = 180$ mm. In Fig. 3.24 are shown the optimal stabilization results for the cavity even side with the previous correction applied.

It can be seen that the unperturbed axial field now has a range below $\pm 5\%$ around the average value and the corresponding tilt sensitivity resides in a $\pm 10\%$ range. The positive effect of field stabilization can also be observed from Fig. 3.24(c)(d): a perturbation at the LE cell and in particular at the HE cell leads to low (LE) or even none (HE) error propagation to the other cells field.

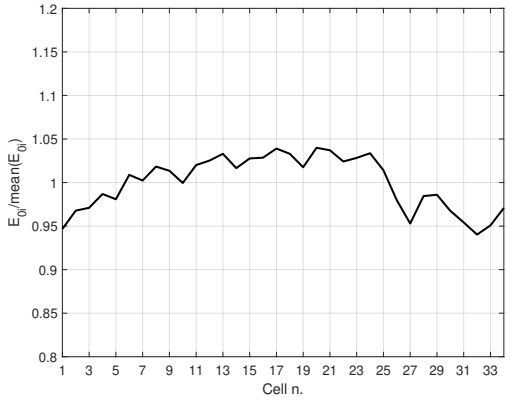

(a) Unperturbed mean axial electric field, odd post-couplers length correction applied.

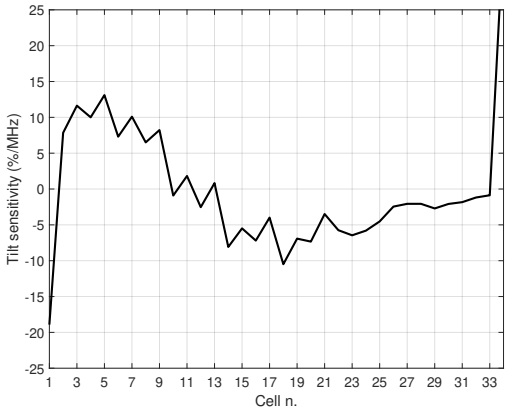

(b) Tilt sensitivity curve with odd post-couplers length correction applied.

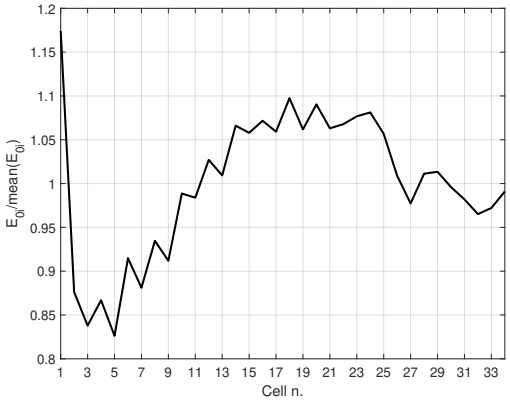

(c) Axial field with low energy (LE) perturbation applied, odd post-couplers length correction applied.

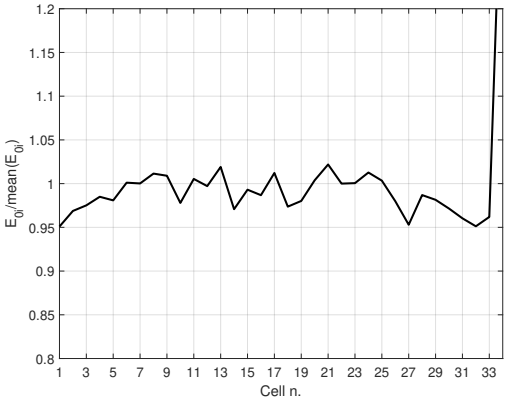

(d) Axial field with high energy (HE) perturbation applied, odd post-couplers length correction applied.

Fig. 3.24: Results of the stabilization campaign with odd post-couplers length correction applied.

4

X-Band Mode Launcher

In chapter 1 the difference between proton and electron accelerating structures has been explained, while in chapters 2 and 3 the study of a proton accelerating structure has been presented. In this chapter a launching-accelerating travelling wave structure for electron acceleration will be presented. In particular, the experimental results that validates both the mode launcher design and the field measurement setup, based on the bead-pull technique, will be presented.

The research on high gradient radiofrequency devices is aimed to develop innovative accelerating structures and achieve higher accelerating gradient in order to increase brilliance of accelerated bunches. Recent research has shown that accelerating gradients up to 250 MV/m are feasible using cryogenically cooled copper accelerating structures. A high brilliance requires high field quality in the RF photoguns and in its power coupler. Moreover, the higher is the electric field on the cathode surface of the gun, the lower the beam emittance needs to be.

In the framework of the collaboration between INFN-LNS, INFN-LNF and SLAC (USA), a novel X-band mode launcher structure has been developed: this structure, presented in [30], is composed of a power coupler which consists of a mode launcher that converts the rectangular TE_{10} mode into the circular TM_{01} accelerating mode [14]. The proposed structure adopts a fourfold symmetry in order to minimize both the dipole and the quadrupole RF components in the way to mitigate the emittance growth in the early stages of the acceleration process.[31, 32].

The structure, operating at the frequency of 11.42 GHz, accelerates electrons through a central circular waveguide section that operates in the TM_{01} mode: the axial and azimuthal electric fields have been measured in a similar fashion to those presented in §3.4, but this time in a travelling wave structure.

The experimental characterization has been performed in the framework of the Di-Electric and METallic Radiofrequency Accelerator (DEMETRA) activities and conducted at INFN-LNS. In particular, the "cold" test measurements of two identical

mode launchers joined in a back-to-back configuration will be discussed. This configuration allows a direct measurement of S-parameters as well as electric field using a two-port vector network analyzer (VNA).

The HFSS model of the structure is shown in Fig. 4.1: it is based on four symmetric sidewall coupling apertures that reduce the converter length and allow on-axis power coupling of the azimuthally symmetric TM_{01} mode. The symmetry of the configuration removes all non-fourfold symmetric modes i. e. dipolar components (as the standard mode launcher does) and quadrupole components. In our case, in order to couple a TM mode, the branching network lays in the H-plane: the adopted original and compact layout keeps the maximum surface electric and magnetic fields sufficiently low to guarantee multi-MW delivery (200 MW) to a device using this structure.

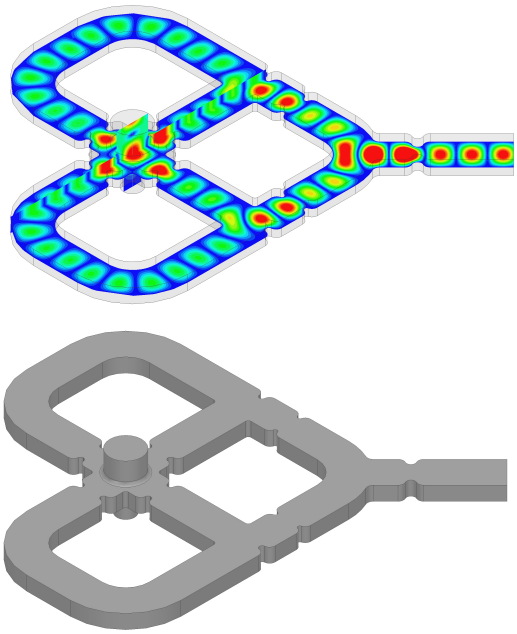

Fig. 4.1: HFSS 3D model of the X-band mode launcher structure.

4.1 The Steele non-resonant perturbation theory

In §3.2 the Slater perturbation theorem has been explained and applied for the electric (or magnetic) field measurement in standing wave structures: if a small perturbing object is introduced and moved inside a cavity, its movement causes a shift in the resonance frequency that is proportional to the electric field in the point where the bead is found. However, in some cases the electric field measurement is desired in devices in

which resonance cannot be employed, for example a lossy device that don't supports resonance. Another example is a field measurement under non-resonant conditions (like the measure of a travelling wave into a waveguide).

So it is desirable a technique that allows to measure the electric field under non-resonant conditions, where the frequency at which the measure is made remains fixed. The non-resonant techniques can be classified into two categories:

- those in which the reflection coefficient (ot the $|S_{11}|$) is measured;
- those performed in two port deviced in which the transmission coefficient (or the $|S_{12}|$) is measured.

As stated before, the d. u. t. can be a transmission line, a waveguide or in general a device that: a) has electromagnetic power entering in it only through a single port while the field measurement are being made, b) a single TE, TM or TEM mode is excited in the part of the structure where the reflection (or transmission) coefficient is being measured, c) the walls of the device have very high degree of isolation between its interior and its exterior (highly conducting metal walls), and d) the device walls have linear and isotropic electrical parameters.

A typical travelling wave device on which the field can be measured through the non-resonant perturbation theory is shown in Fig. 4.2.

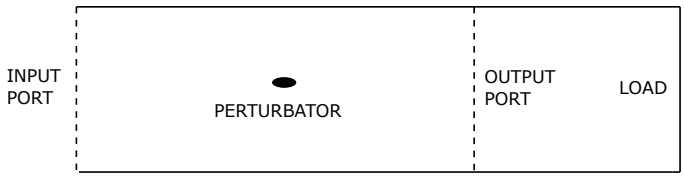

Fig. 4.2: Schematic of a device in which the field have to be measured. It has just one waveguide (or transmission line) port through which electromagnetic energy is permitted to pass into its interior. It can have any size or shape.

Like in the Slater perturbation theorem, the basic formulation of the non-resonant perturbation theorem considers two different electromagnetic fields inside the device being measured: a field in absence of the perturbing object and a field in presence of the perturbing object. Unlike Slater perturbation theorem, these two field have the same frequency.

The mathematical process to relate the fields to the perturbing object introduced into the device is found in [33] and will be omitted here for the sake of brevity. The final result can be written as

$$2P_i(\Gamma_p - \Gamma_u) = -j\omega(k_1 E^2 - k_2 H^2) \tag{4.1}$$

where P_i is the incident wave power level, Γ_p, Γ_u are, respectively, the reflection coefficients in presence and in absence of the perturbation, E, H are the field components in absence of perturbation and k_1, k_2 are two weight terms depending on electric and magnetic dipole moments.

By considering an usual accelerating mode, TM_{01}, as in the case at hand, (4.1) can be related to the $|S_{11}|$ and we obtain [34]

$$\Delta|S_{11}| = |S_{11}|_p - |S_{11}|_u = \frac{-j\omega k_1}{P_i} E^2 \tag{4.2}$$

since the magnetic field vanishes on axis, where the perturbator is placed, in the TM_01 mode.

In (4.2), $|S_{11}|_u$ is the value taken in absence of the perturbation (i. e. the value acquired with the bead placed outside of the device), while $|S_{11}|_p$ are the values acquired at each position of the perturbator. All the $|S_{11}|$ values are taken at a fixed frequency, usually the operating frequency of the device. In the end, the electric field value can be related to the square root of the difference $\Delta|S_{11}| = |S_{11}|_p - |S_{11}|_u$.

4.2 Cold model prototype

The designed and manufactured mode launcher is composed of two separate aluminum halves: a milled plate where the waveguide branching is machined (see Fig. 4.3(a)) and a plane cover. Being the "cold-test" aluminum structure based on two pieces, it requires a large number of screws to ensure good conducting contact and to avoid leakage. The milling of aluminum blocks has been operated by COMEB [35] using a tolerance of 10 μm and a surface roughness of 100 nm. All the edges have been rounded to minimize the peak surface fields. When the two halves are joined together, they form the complete ML. Two identical aluminum prototypes (Fig. 4.3(b)) have been fabricated and measured in three back-to-back configurations for three different circular waveguide connection lengths (30, 60 and 120 mm) through an Agilent VNA. Fig. 4.3(c) shows the final assembled identical converters connected back-to-back.

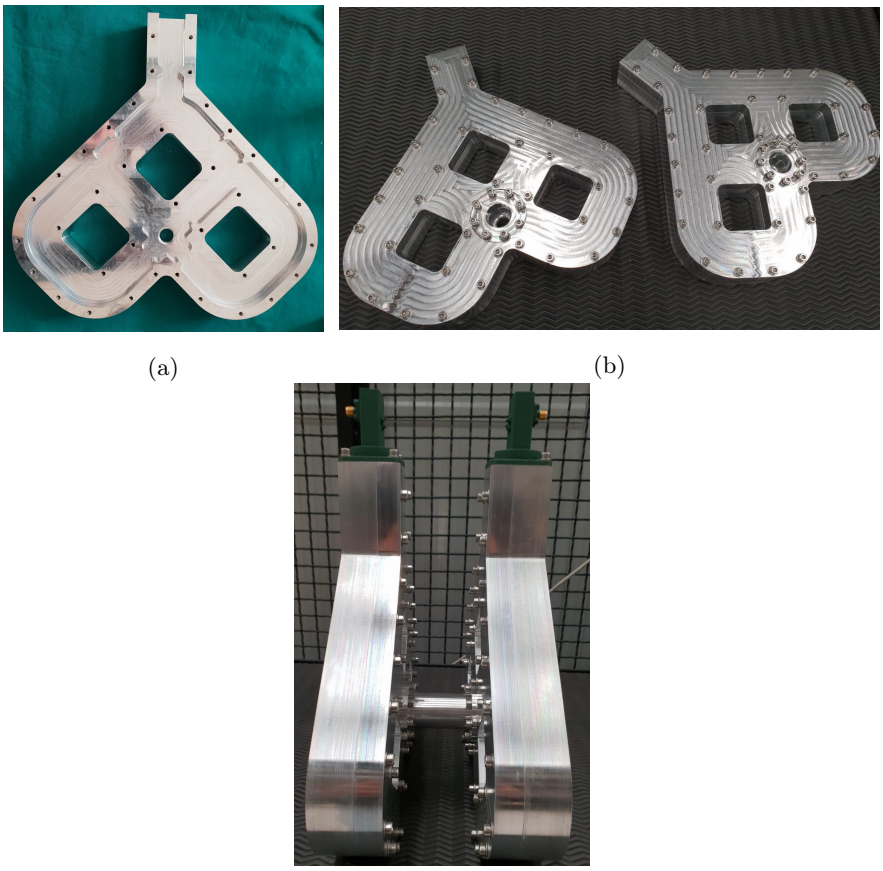

(a) (b)

(c)

Fig. 4.3: Manufactured aluminium mode launchers for cold tests: (a) inside of the single mode launcher, (b) two mode launchers with mounted cover, (c) mode launcher assembled in back-to-back-configuration.

4.2.1 S-parameters measurement

For the two X-band mode launchers back-to-back connected, VNA measurements of the scattering parameters have been performed and compared with HFSS simulations, as shown in Fig. 4.4. As said, the two identical mode launchers have been jointed back-to-back through three different uniform circular waveguides of 30, 60 and 120 mm.

The -10 dB operating bandwidth is [11.3 - 11.5] GHz and the $|S_{11}|$ is below -40 dB at the operating frequency of 11.42 GHz for all the three considered configurations. Back-to-back measurement shows that the average insertion loss at the operating frequency is around $\simeq 0.3$ dB for the three configurations, higher than the one predicted by simulations: this is due to the loss resulting from fabrication tolerances and assembly errors present in this cold test prototypes. In the measurements, we can also observe secondary resonance peaks in the S parameters. These peaks are

caused by multiple reflections that forms a resonance between the two identical arms: it can be seen that by changing the distance between the two structure halves, the resonant frequencies of these peaks make a shift, as expected and observed in [36, 37].

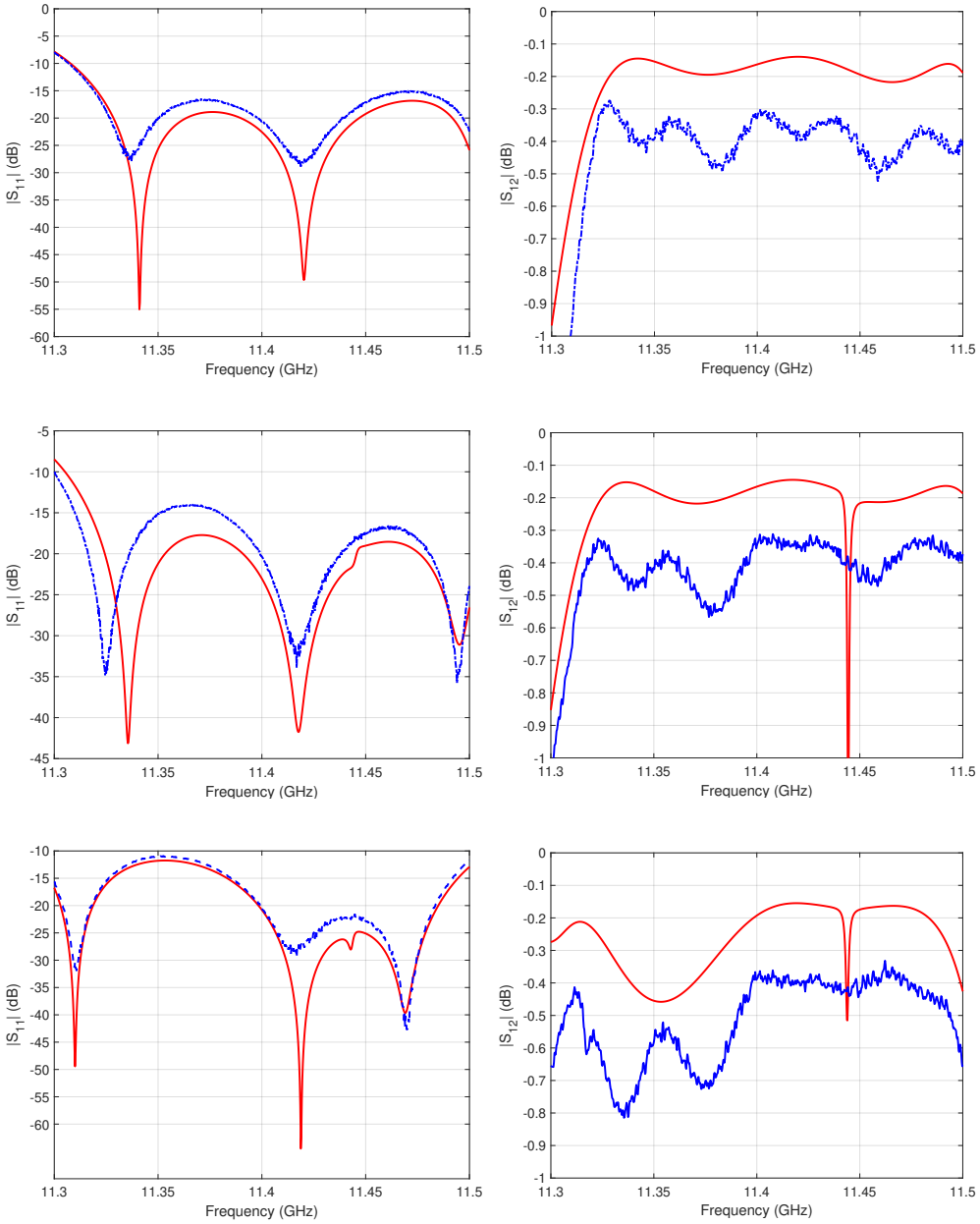

Fig. 4.4: Simulated (red curves) vs. measured (blue curves) S-parameters for the full devices in back-to-back configuration: $|S_{11}|$ on the left column, $|S_{12}|$ on the right column. A very good agreement between the two is visible, despite some numerical simulation spikes.

4.2.2 Electric field measurement

In addition to the S-parameters measurements, axial and azimuthal field measurements have been performed, inside the circular waveguide, through the use of the bead-pull technique and by relying on the Steele non-resonant perturbation theory [33]. A small metallic bead (the perturbing object) is driven along the waveguide axis and, for each bead position, the $|S_{11}|$ value is acquired. As explained in §4.1, the quantity $\sqrt{\Delta|S_{11}|}$ will be proportional to the local field at each bead position.

Fig. 4.5(a) shows the bead-pull setup used for the electric field measurement: it is composed of a 2-port Agilent N5230A PNA-L Microwave Network Analyzer, a bead-pull measurement plate comprised of a stepped motor used to drive along the structure the wire that sustains the bead, and a Labview program that, by interfacing the stepped motor and the VNA, controls the wire movement and the signal sample rate. The mode launcher has been connected to the VNA in back-to-back configuration and we fixed the measurement frequency to the operanting one (11.42 GHz), without changing it; in fact, the Steele non-resonant perturbation theory states that the field (i. e. the $\sqrt{\Delta|S_{11}|}$) measurement is independent from the frequency. Through the Labview program one can set the sample interval, the number of samples to take within the selected interval and the sample rate.

For the axial field measurement, a sample interval of 100 mm has been chosen, with a sample rate of 1 mm, starting from the circular waveguide cut-off aperture. A metallic bead has been used to take the desired values.

For the azimuthal field measurement, a circular flange visible in Fig. 4.5(b), has been employed. The flange has been rotated with a 10° step and the $|S_{11}|$ has been taken for every step along a circumference of radius $r = 4$ mm at the axial position $z \simeq 90$ mm.

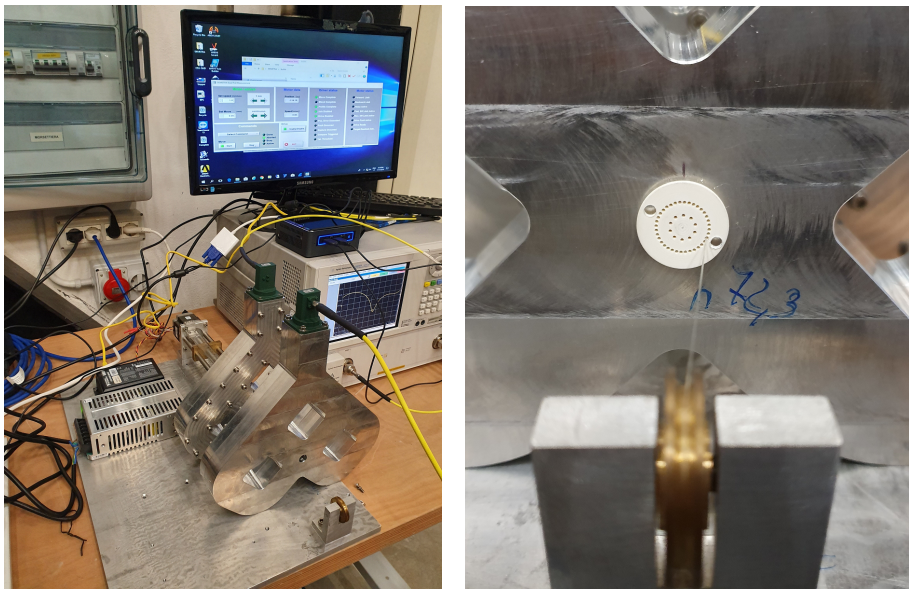

(a) (b)

Fig. 4.5: (a) Bead-pull setup used for the field ($\sqrt{\Delta|S_{11}|}$) measurements on the mode launcher. (b) Circular flange used for the azimuthal field measurements.

Fig. 4.6 shows the axial and azimuthal $\sqrt{\Delta|S_{11}|}$ vs. bead position measurements performed on a full device in back-to-back configuration with the corresponding electric field HFSS simulations. The curves are normalized with respect to their maximum value in order to make a proper comparison.

From Fig. 4.6 it can be seen that the simulated field curves and the measured ones presents very good agreement between each other.

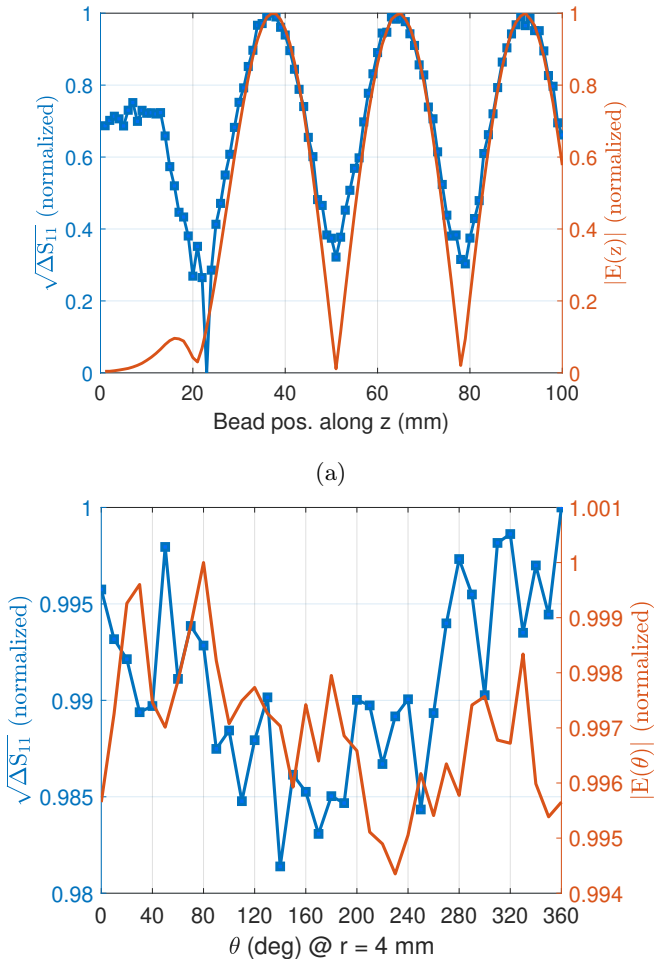

Fig. 4.6: Measured $\sqrt{\Delta|S_{11}|}$ values vs. bead position (blue curves) and comparison with HFSS electric field simulations (red curves). (a) The $|S_{11}|$ values have been taken along the circular waveguide axis, on an interval of 100 mm starting from the cut-off flange, for the axial measurement. (b) The $|S_{11}|$ values have been taken along a circumference of radius $r = 4$ mm at the axial position $z \simeq 90$ mm for the azimuthal measurement.

Part II

Towards a Dielectric Laser Accelerator

The first part of this thesis dealt with radio frequency metallic proton accelerators and a Drift Tube Linac has been presented as a case of study. Because of electrical breakdown of metals in the presence of high electric fields, conventional metallic particle accelerators, which consist of metal cavities driven by high-power microwaves, typically are operated with accelerating fields ranging from 10 to 30 MV/m. Charged particle devices based upon conventional RF technology are often large and expensive due to the accelerator length and total stored energy needed to accelerate particles to high energy. Size and cost reductions are also required for many applications. The main advantages of a Dielectric Laser Accelerator (DLA) compared to standard RF metallic accelerator can be summarized as follows: high efficiency, high accelerating gradient, high brillance, low cost and smaller size, low power dissipation [4]. The second part of this thesis is organized in the following way: chapter 5 gives a brief introduction on the dielectric laser accelerators (DLA) and their advantages over the metallic ones. Section 6 gives an example of a dielectric Photonic Crystal (PhC) based coupler able to create an "accelerating mode" from an injected "telecom mode". Section 7 describes the the electromagnetic band gap (EBG) structures and the principle of mode confinement into a periodic pattern. Chapter 8 is dedicated to the EBG structure studied in this thesis: the woodpile structure. After a brief description of the main characteristics and fundamental parameters, the numerical study and optimization is discussed. The band diagram of the structure has been obtained with the use of the MIT Photonic Bands (MPB) [38] package, taking also in account the introduction of the hollow core defect that allows to trap a guided mode. After the study of the infinite periodic woodpile, the structure has been truncated and fed by rectangular ports in order to characterize it in terms of S-parameters with the Ansys HFSS full-wave simulator. Further optimization concerned the launching metallic waveguide setup and the obtaining of better mode confinement by a lateral dimension increase. Finally, in chapter 9 the experimental results obtained with a realized prototype are presented, showing the excellent agreement with the 3D simulations in terms of S-parameters and axial electric field.

All the above study has been scaled up at optical frequencies and chapter 10 presents the simulated and experimental results obtained with a silicon woodpile structure operating at W-band: this device will be used as the telecom waveguide in a future coupling structure of a W-band accelerator.

5

Introduction

The widespread use of high energy particle beams in research, medicine, and X-ray generation coupled with the large size of modern radio frequency accelerator devices has motivated a strong need for alternative accelerators operating at higher and higher frequencies (reaching optical regime).

In fact, it is well known that conventional metallic RF accelerating structures suffer from electrical breakdown in the presence of strong electric fields, therefore in the recent years an alternative based on dielectric accelerators has been proposed to overcome this limitation.

The two main advantages of the dielectric laser accelerators are the larger damage threshold of dielectrics with respect to metals, and the potential reduction of cost and size of particle accelerators working at higher frequencies; in particular, a DLA can operate in the optical regime where perfect conductors do not exist. In this framework, Photonic Crystals have opened the way to the realization of compact dielectric devices operating in different frequency regimes. PhC waveguides offer the possibility of carefully engineering the dispersion properties of the guiding structures, thus have been proposed for molding phase and group velocity in controlled ways. This can be also useful in applications concerning linear accelerators. PhC waveguides seem to be the ideal choice for the realization of a dielectric accelerator: in particular, they allow hollow-core guiding of the spatially overlapped particle and light beams, the phase velocity can be tuned in order to get synchronous acceleration, the group velocity can be engineered based on the desired interaction length and higher-order modes can be efficiently suppressed. The interest in PhC guiding structures is not limited to the case of a single waveguide; in fact, PhC couplers obtained by placing several waveguides side-by-side have already been analyzed in depth.

Linear accelerators based on two-dimensional (2D) PhC waveguides, Bragg waveguides, woodpile waveguides, and photonic crystal fibers have already been proposed and studied in the literature.

6

2D PhC coupler

In a DLA, as in a metallic accelerator, the particle is accelerated into a waveguide excited with a mode possessing a predominant longitudinal component (for example, in the case of a Bragg fiber, the accelerating mode needs to possess the electric field directed along the waveguide axis i. e. TM_{01}-like, as in the case of metallic accelerators). Coupling such accelerating mode into a dielectric accelerator from a gaussian laser beam is not a simple task because the laser mode and the accelerating mode have a poor overlap. To this aim, a 2D PhC coupler composed of a dielectric periodic structure and two hollow waveguides has been studied and numerically validated. This structure supports a complete conversion of the input power (from the input waveguide) into a TM_{01}-like uniform accelerating mode (in the accelerating waveguide) with a longitudinal field component synchronous with relativistic electrons.

Fig. 6.1 shows the 2D PhC. The structure, presented in [6], is a directional coupler formed by two adjacent vacuum waveguides that are practiced in an alumina PhC quasi-2D structure: in order to have an efficient energy exchange between the two waveguides, the two linear defects have been singularly designed and tuned so that the interacting modes have the same propagation constant [39]. This 2D PhC is based on a triangular lattice of periodically arranged vacuum holes for which the lattice period d (i. e. the distance between the centers of two adjacent holes) is chosen in the way to have a band-gap around the working frequency. The defect size has been chosen in the way to synchronize the accelerating mode with the particle beam.

For the structure, the accelerating waveguide has been named WG1 and the launch waveguide has been named WG2.

The structure has been tuned with the supercell method considering an infinite periodic two-channel waveguide, then has been truncated at the appropriate beat length and validated through the use of full-wave electromagnetic simulators, from which the electric field has been computed. From Fig. 6.1 it can be seen that WG1 has a strong longitudinal electric field component, denoted as "the accelerating mode",

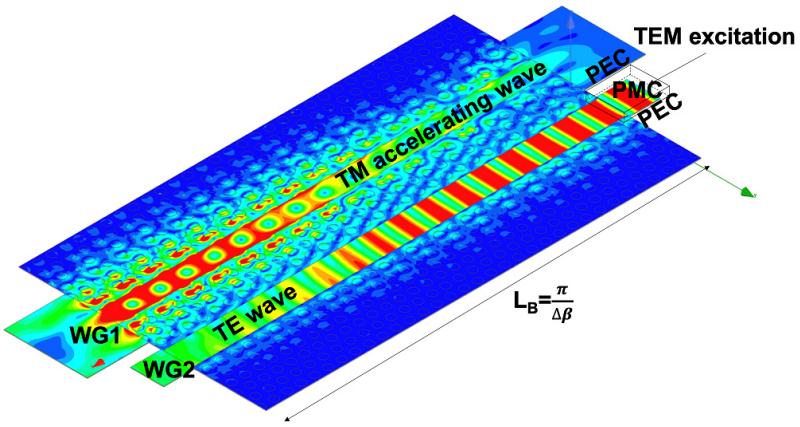

Fig. 6.1: 3D model of the simulated 2D directional coupler based on the triangular lattice. The telecom waveguide, named WG2, possesses a TE_{10} mode that, after a beating period, transfer itself into the accelerating waveguide, named WG1, becoming a TM-like mode that have a predominant field component along the waveguide axis and is thus suitable for particle acceleration.

as it allows the propagation of a TM-like mode suitable for accelerating particles, similarly to a standard metallic LINAC. The field in the larger waveguide WG2 has a strong transverse electric field component similar to the classic TE_{10} mode or gaussian mode, denoted as "telecom mode": the use of this mode is necessary in this structure because a TM-like mode cannot be easily coupled with a standard telecom laser Gaussian mode or the TEM mode of a parallel plate metallic waveguide since the overlap integral [40] with such mode would be zero.

It is worth to note that the structure of [6] works at X-band and in particular at the frequency of 11 GHz. The aim of the study was to demonstrate concepts like the coupling between the two waveguides but this behaviour is also valid at higher frequencies, in particular in the optical regime and the structure can be scaled up at optical frequencies to provide a dielectric coupler suitable for laser acceleration.

The previous study of a 2D accelerating structure has the limit of confining the accelerating mode only in two dimensions: for this reason, the use of full 3D PhC, having a complete band-gap in all the three dimensions, is preferable when one wants to employ this technology for dielectric laser accelerators. The main advantages in the use of a 3D photonic crystal are the capacity to control the field in all the three directions and the possibility to employ standard TEM-like waveguides for launching the field inside the telecom waveguide, as will be explained in §8.1.1. In this thesis, the well known woodpile crystal has been chosen as the full 3D band-gap PhC; it can

be employed to create a coupling structure between the telecom waveguide, that in particular has been chosen as the case of study, and the accelerating waveguide.

Fig. 6.2 shows a possible geometry for a full 3D PhC coupler based on the woodpile crystal. This structure is actually under study.

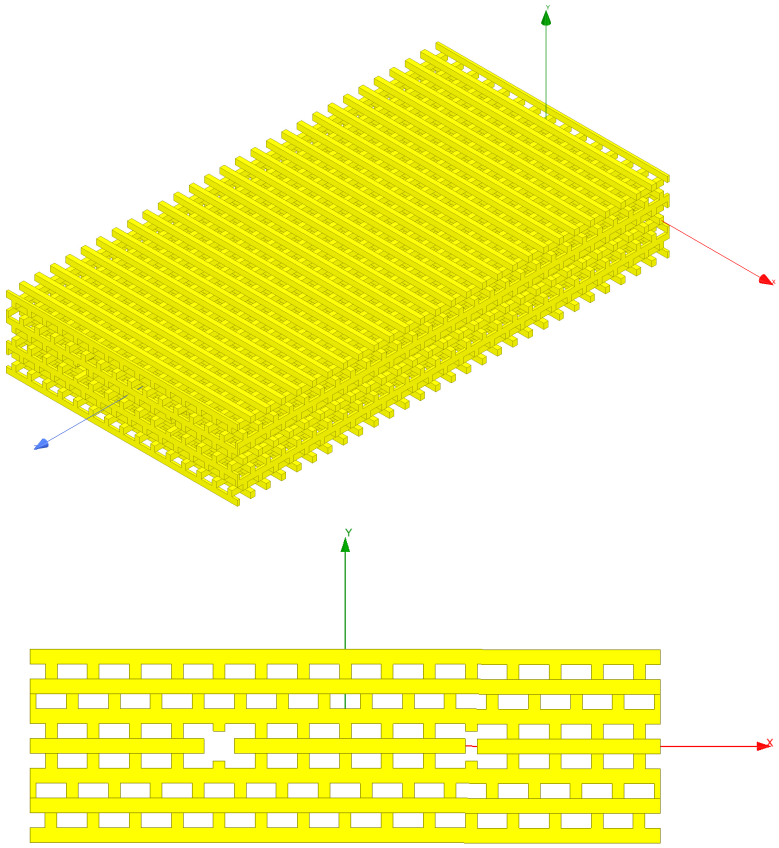

Fig. 6.2: 3D and front view of a PhC coupler based on the woodpile crystal. Two defects has been practiced on the dielectric structure: on the left is placed the telecom waveguide and on the right is placed the accelerating waveguide.

7

Electromagnetic Band Gap (EBG) structures

A crystal is a periodic arrangement of atoms or molecules. The pattern with which the atoms or molecules are repeated in space is the crystal lattice, as seen in Fig. 7.1. Inside the crystal, electrons propagate as waves. Lattice structures can also prohibit the propagation of certain waves. There may be gaps in the energy band structure of the crystal, meaning that electrons are forbidden to propagate with certain energies in some directions. If the lattice potential is strong enough, the gap can extend to cover all possible propagation directions, resulting in a complete band gap. Just as atomic crystals lead to a band structure for electron eigenstates, photonic crystals (PhC) lead to a band structure for electromagnetic eigenmodes. In particular, we are interested in photonic crystals with photonic band gaps, preventing light from propagating in certain directions with specified frequencies. To develop this concept further, consider how metallic waveguides and cavities relate to photonic crystals. Metallic waveguides and cavities are widely used to control microwave propagation; it would be extremely useful to have these same capabilities for electromagnetic waves with frequencies outside the microwave regime, such as visible light. However, visible light energy is quickly dissipated within metallic components, which makes this method of optical control impossible to generalize. Photonic crystals allow the useful properties of cavities and waveguides to be generalized and scaled to encompass a wider range of frequencies. We may construct a photonic crystal of a given geometry with millimetre dimensions for microwave control, or with micron dimensions for infrared control.

If, for some frequency range, a photonic crystal prohibits the propagation of electromagnetic waves of any polarization travelling in any direction, we say that the crystal has a complete photonic band-gap. Usually, in order to create a complete photonic band-gap, one must arrange for the dielectric lattice to be periodic along three axes, constituting a three-dimensional photonic crystal.

Although there are an infinite number of possible geometries for a 3D photonic crystal, we are especially interested in those geometries that promote the existence of

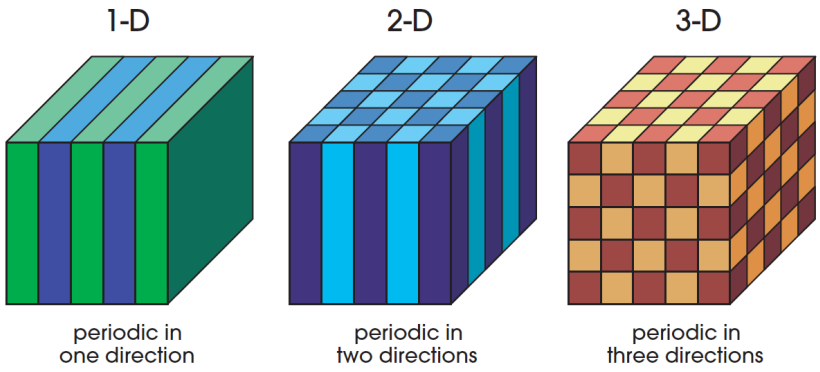

Fig. 7.1: One-, two- and three-dimensional photonic crystals, having periodicity along one or more axes. Different colors in each crystal represents materials with different dielectric constants.

photonic band-gaps, such as those based on the Face Centered Cubic (FCC) lattice (see Fig. 7.2), that exhibits a complete 3D band-gap.

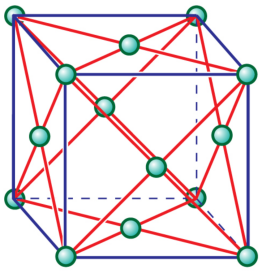

Fig. 7.2: The FCC lattice.

Let's consider a PhC that possess a band gap $[\omega_1, \omega_2]$: if a wave with frequency ω_g, with $\omega_1 < \omega_g < \omega_2$ impinges on this PhC, the wave cannot couple (or transfer) energy to any propagating modes in the PhC and therefore is completely reflected. In such situation only evanescently decaying fields penetrate the PhC, and they transport no energy. A material with a photonic band-gap thus acts like a frequency-selective mirror, completely reflecting frequencies residing inside the band-gap. If a so called defect is introduced into the structure by removing or altering one element or more elements of it, then any fields excited at frequencies within the band-gap will be trapped near the defect, because they cannot propagate away. The term defect does not refer to a manufacturing error, but rather to a deliberate, localized change that breaks the structure symmetry. The trapped fields decay evanescently into the crystal. As long as the surrounding crystal is infinite, the evanescent fields carry away no

energy. However, if the surrounding crystal is finite, then fields can "tunnel" through the crystal, emitting a propagating wave outside the crystal that does carry away energy ("diffractive" or "radiative" losses).

For an optical accelerator, the defect is typically a linear hollow channel, and the accelerating mode must have a longitudinal electric field along the axis of the particle trajectory, with the phase velocity equal to the particle velocity.

8

Numerical study of an EBG device: the woodpile structure

As said before, different periodic arrangements of dielectric and vacuum can be tuned to create a photonic crystal with a frequency band-gap where no electromagnetic propagation is allowed [39, 41, 42, 43].

This thesis is focused on the study of the woodpile crystal: the work here discussed has been presented in [12], [44] and [45].

This structure, the first three-dimensional photonic crystal with a complete band-gap to be fabricated on micron scales for light at infrared wavelengths [46], can be thought as composed by a "pile" of rectangular $w \times h$ bricks with alternating orthogonal orientations, which can be practically obtained from layers properly stacked together, as seen in Fig. 8.1.

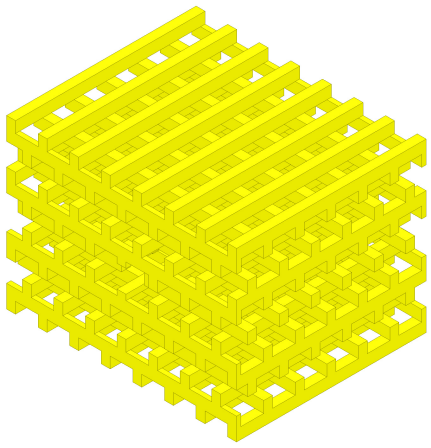

Fig. 8.1: The woodpile structure: it is composed of layers of bricks (or rods) stacked together with alternating orthogonal orientation.

The whole woodpile structure consists of several layers (in our case made of alumina) stacked in the vertical y direction; each layer is shifted by half lattice period $d/2$ in both x and y directions with respect to the layer below [42].

The structure repeats itself every four layers, creating a large frequency band-gap where the electromagnetic propagation is suppressed [42].

The first step in the study of the woodpile crystal has been to obtain the band (dispersion) diagram of the infinite structure. This study has been performed through the use of the MPB package. The woodpile band structure can be studied and tuned adopting the face centered cubic (FCC) lattice [46]. Here, for the sake of simplicity, a more practical tetragonal lattice representation has been adopted (see Fig. 8.2); in this way, the woodpile structure has been brought back on a conventional Cartesian reference system. This approach introduces a different band folding than the FCC representation, however the two band diagrams are related [47] and the band gap edges remain the same.

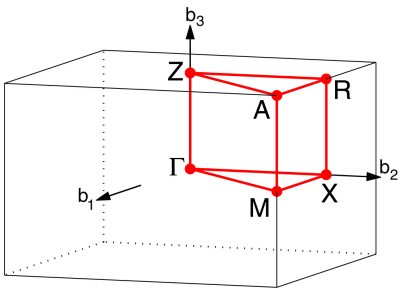

TET path: Γ-X-M-Γ-Z-R-A-Z|X-R|M-A

[Setyawan & Curtarolo, DOI: 10.1016/j.commatsci.2010.05.010]

Fig. 8.2: Simple tetragonal lattice. The first Brillouin zone is the path highlighted in red.

The woodpile infinite structure can be easily obtained by constructing a primitive cell, as seen in Fig. 8.3(a), and by infinitely repeating it into the free space. Subsequently, by choosing a proper normalization for the structure dimensions and the dielectric material (in our case alumina with $\epsilon_r = 9.8$), the band structure can be obtained as shown in Fig. 8.3(b).

The proposed structure operates at 18 GHz. This frequency has been selected with two purposes: 1) to validate the design at "lower" frequencies before bringing it to the optic regime and 2) to employ the device as a DC-break that can be used in microwave ion sources to break the DC-path from the generator to the RF source, as will be explained in detail in §9.4. The structure has been found very robust to fabrication errors and thus, in a second step, has been scaled-up at optical frequencies, as explained in §10.

Following [42] and [46, pag. 102], for the dielectric contrast 9.8:1 the dimensions ratio that gives the largest band-gap has been chosen, that is $w = 0.2\sqrt{2}d$, $h =$

$0.25\sqrt{2}d$. In this way, the band-gap has been found centered around the normalized frequency of $\frac{f_c d}{c} \approx 0.4$. By choosing the lattice period d (i. e. the distance between the centers of two adjacent bricks located in the same layer), the band-gap can be centered at the frequency of interest; in our case, in order to operate at $f_c \approx 18$ GHz, we choose $d \approx 6.73$ mm. The other characteristic dimensions can now be automatically evaluated as $w = 0.2\sqrt{2}d = 1.9$ mm and $h = 0.25\sqrt{2}d = 2.38$ mm.

For the band-gap evaluation a four-layer primitive cell with half-period offset $d/2$ between brick centers has been adopted (see Fig. 8.3(a)).

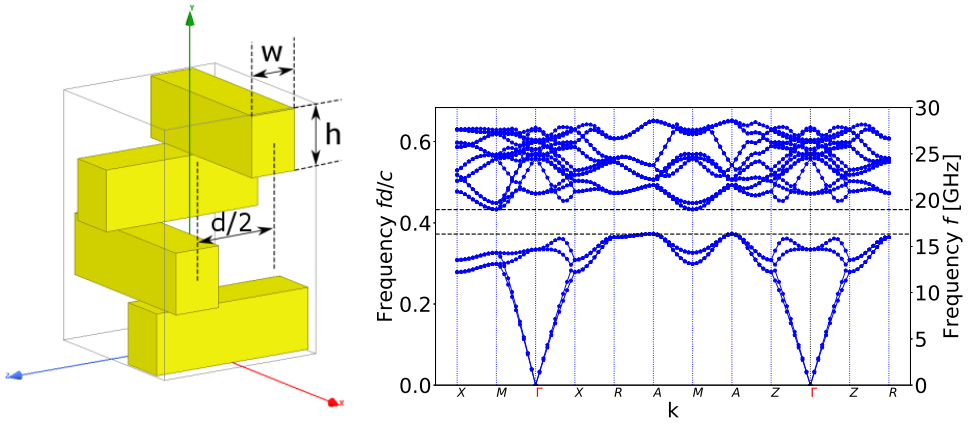

(a) (b)

Fig. 8.3: (a) Woodpile structure primitive cell with its geometrical parameters: brick width w, height h, and lattice period d. The structure repeats itself every four layers, along y direction. (b) Calculated band structure. The complete photonic band-gap reaches a maximum value of 15.2% when $w = 1.9$ mm and $h = 2.38$ mm.

Once the configuration that presents the largest band-gap has been found, a *defect* has been created by removing some material from the structure. This properly tuned defect can support an electromagnetic mode that can be guided along the structure in the way to form a waveguide (as in the case at the hand) or trapped inside to form a resonant cavity. Fig. 8.4 shows a structure front view where a $w_d \times h_d$ central defect has been introduced: again, the defect can be tuned by the use of MPB in the way to trap a guided mode inside it. For the proposed structure the optimal dimensions have been found as $w_d = 4.911$ mm and $h_d = 4.7588$ mm.

The infinite z-periodic guiding structure can be studied with the supercell method. Here we are interested in the band structure *projected* along the propagation direction z: this projected band diagram can be again obtained through the MPB package. In Fig. 8.5 the projected band diagram for the presented symmetric woodpile waveguide

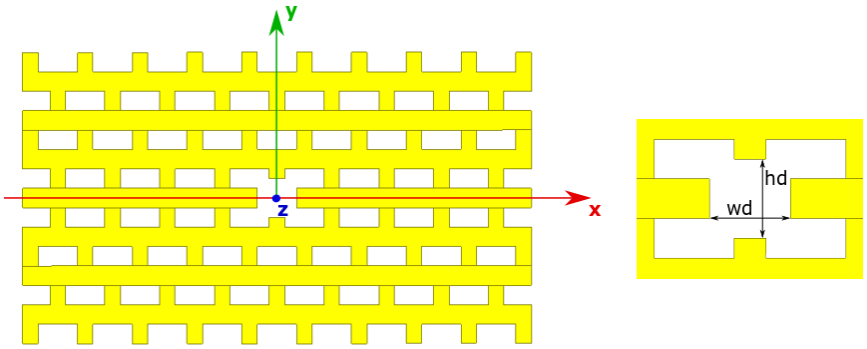

Fig. 8.4: Woodpile waveguide front view: the structure has been made symmetric in the vertical direction (xz symmetry plane) for better mode confinement. A rectangular $w_d \times h_d$ defect has been practiced in the structure center in order to confine a guided mode.

structure is shown: the red curve represents the guided mode which resembles the one of a metallic standard waveguide.

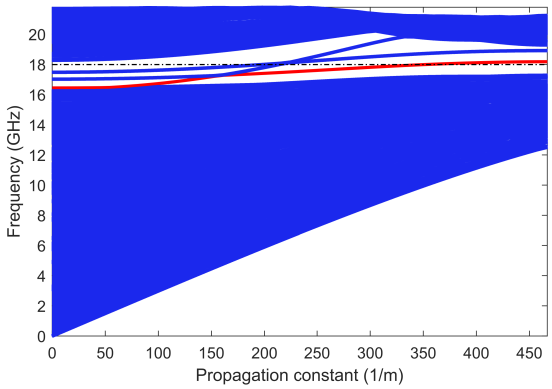

Fig. 8.5: Projected band diagrams for the designed structure. By imposing $d = 6.73$ mm the dispersion curve (in red) of a guided mode intersects the frequency of interest (black horizontal line). The other two blue curves visible inside the band-gap are the dispersion curves of two additional modes supported by the hollow core EBG structure. However, they are not coupled in the presented setup due to the different polarization, propagation constant and symmetry with respect to the exciting TE10 mode.

8.1 3D full wave simulations

The woodpile waveguide structure has been simulated and validated by the commercial full-wave simulators Ansys HFSS [17] and CTS Microwave Studio. In particular, the dielectric woodpile waveguide has been truncated and fed by a WR62 standard

rectangular waveguide supporting the TE10 mode. The dielectric length along the defect axis (the z direction) has been fixed equal to $l_z = 6d = 40.38$ mm and the insertion loss (IL) bandwidth at 0.5 dB has been chosen as the main quality parameter.

8.1.1 Optimization of the launch metallic waveguides

In order to feed the structure, a simple metallic waveguide-to-woodpile transition has been adopted, as visible in Fig. 8.6: in the chosen implementation at microwave frequencies, standard WR62 metallic waveguides mounted over a flat flange, are juxtaposed to the dielectric woodpile waveguide to couple electromagnetic waves into the defect channel. This approach is simpler to realize when compared to the solutions adopted in [41] and [48], where the the input and output metallic waveguides are inserted into the EBG crystal.

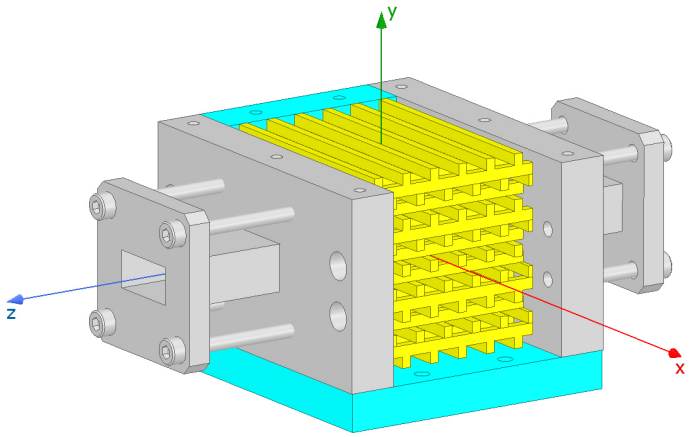

Fig. 8.6: 3D model of the woodpile device. In order to feed the structure, two standard WR62 metallic waveguides (grey components) are adopted. Plexiglass lateral enclosure (light blue components) is also visible.

The transition losses between metallic and dielectric waveguides can be minimized by maximizing the hybrid scalar product, or overlap integral C_{wp-wg} [40], between the woodpile mode $\underline{\mathbf{e}}_{wp}$ and the TE10 mode of the rectangular waveguide, $\underline{\mathbf{e}}_{wg}$.

We define this two-dimensional "overlap" integral over the access port cross-section S of the structure as it follows:

$$C_{wp-wg} = < \underline{\mathbf{e}}_{wp} \cdot \underline{\mathbf{e}}_{wg} > = \int_S \underline{\mathbf{e}}_{wp} \cdot \underline{\mathbf{e}}^*_{wg} \, dS \tag{8.1}$$

The transverse field vectors of the woodpile and metallic waveguide, $\underline{\mathbf{e}}_{wp}$ and $\underline{\mathbf{e}}_{wg}$ respectively, are normalized to unity and consequently the values of (8.1) are in

the $[0, 1]$ range, being one when the two modes are identical and, on the contrary, zero when the two modes are "orthogonal". Starting from standard WR62 waveguide dimensions ($a = 15.8$ mm, $b = 7.9$ mm) and choosing after numerical optimization $b_{opt} = 6$ mm, which actually consists in a tapered version of the WR62 waveguide, a maximum overlap integral value of $C_{wp-wg} = 0.49$ has been found [12]. Hereinafter, standard dimensions will be considered ($a = 15.8$ mm, $b = 7.9$ mm) to be consistent with measurements performed by using standard WR62 waveguides, presented in the next chapter.

In Fig. 8.7(a) the transverse electric field, $\underline{\mathbf{e}}_{wg}$, of the TE10 mode of a standard WR62 waveguide is shown. In Fig. 8.7(b) the transverse electric field, $\underline{\mathbf{e}}_{wp}$, of the EBG woodpile waveguide mode is shown at the interface between the metallic waveguide and the EBG waveguide, $z = 0$ mm in our reference system (see Fig. 8.4), which corresponds to a half brick of width $w/2$. It is clear that at $z = 0$ mm the selected EBG-waveguide mode has a dominant polarization along the y axis (thanks to the introduced symmetry plane, see Fig. 8.4) which well matches the transverse electric field of a standard WR62 operating in the fundamental TE_{10} mode. A different cut along the z direction results in a poor overlap integral. In Fig. 8.7(c) the transverse electric field, $\underline{\mathbf{E}}_t$, at $z = d/2$ is shown: in this case it is difficult to couple field into the woodpile waveguide, as confirmed by full wave simulations.

Fig. 8.8 shows the S-parameters of a woodpile structure when using standard metallic WR62 waveguides and when using custom metallic waveguides with height $b = 6$ mm: a clear increase of 0.5 dB IL bandwidth is visible.

8.1.2 Study of the lateral dimension of the crystal

As seen in the previous subsection, a way to increase the transmission bandwidth is to properly modify the input and output metallic waveguides. As can be expected, another important parameter that is related to the wave confinement inside the crystal defect is its dimension in the plane transversal to the propagation direction. The structure behaviour vs. its lateral dimension has been studied through numerical simulations and it has been found that a way to increase the woodpile 0.5 dB IL bandwidth is to enlarge the structure in the plane transversal to the z-propagation direction (xy plane). Fig. 8.9 shows the S-Parameters for the studied structure with propagation length $l_z = 6d$ and different dimensions in the xy plane. In particular, starting from a base structure composed of 9 periods along x and 15 layers along y, configuration (a) of Fig. 8.4, three different geometries, hereinafter configuration (b), (c) and (d), have been studied in simulation:

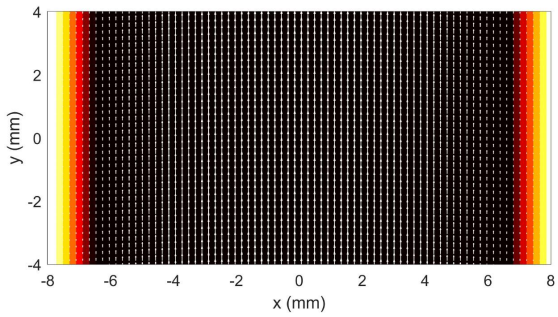

(a)

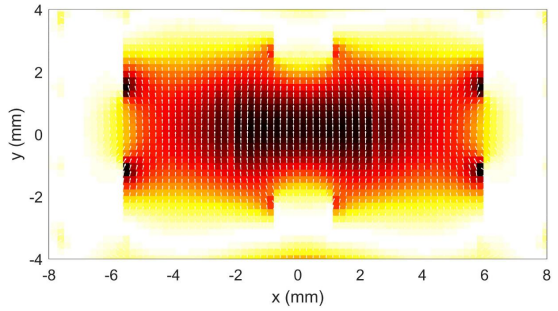

(b)

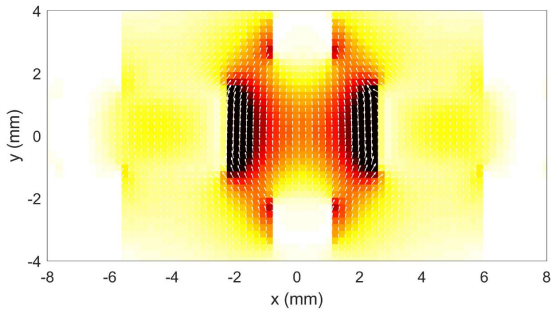

(c)

Fig. 8.7: (a) Transverse mode profile $\underline{\mathbf{e}}_{wg}$ of the WR62 waveguide (standard height $b_{WR62} = 7.8994$ mm. (b) Mode profile of the woodpile waveguide ($z = 0$ mm cut): $\underline{\mathbf{e}}_{wp}$ vector field superimposed to the field color-map showing that both the obtained polarization and field distribution resemble the $\underline{\mathbf{e}}_{wg}$ of the feeding WR62 waveguide. (c) Mode profile of the woodpile waveguide ($z = d/2$ cut): $\underline{\mathbf{e}}_{wp}$ vector field superimposed to color-map.

(b) enlargement along $\pm y$ by adding 3 h-thick layers of rods along $+y$ and 3 h-thick layers of rods along $-y$;

(c) enlargement along $\pm x$ by adding 2 periods along $+x$ and 2 periods along $-x$;

(d) the union of both enlargements along $\pm x$ and $\pm y$: (b) plus (c).

It can be seen that, by making the structure larger, the $|S_{12}|$ bandwidth at -0.5 dB increases.

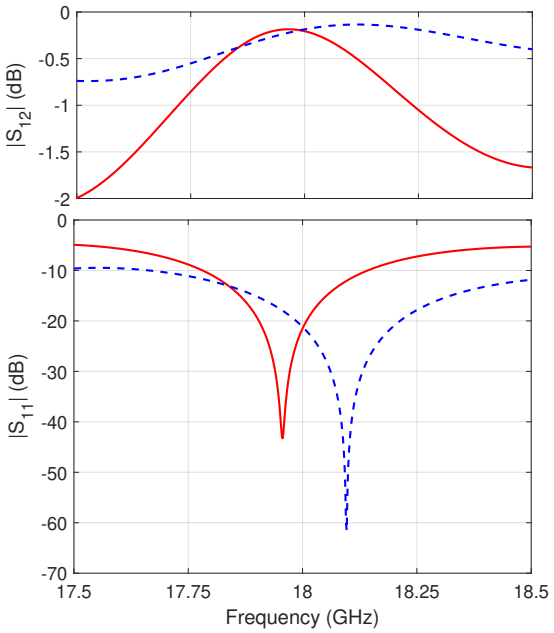

Fig. 8.8: Woodpile waveguide S-parameters, standard WR62 waveguides (red curves) vs. custom metallic waveguides with $b = 6$ mm (blue dashed curves). $|S_{12}|$ (top) and $|S_{11}|$ (bottom).

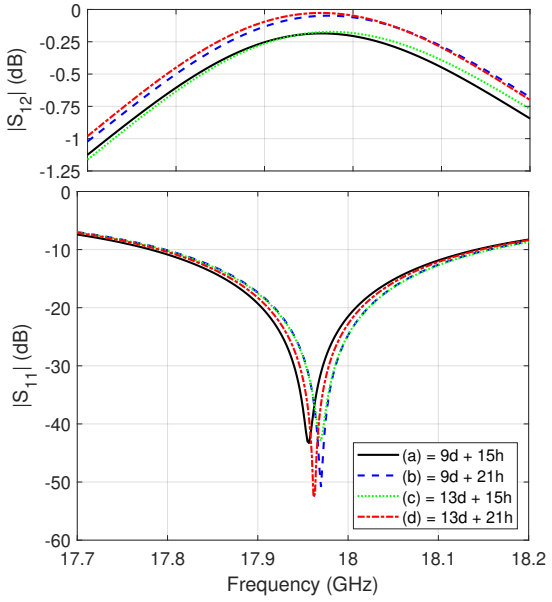

Fig. 8.9: Simulated $|S_{12}|$ (top) and $|S_{11}|$ (bottom) of the woodpile waveguide with $l_z = 6d = 40.38$ mm length and different EBG transversal size (on the xy plane). WR62 standard metallic waveguides are used.

In Table 8.1, the operating frequency and the percent bandwidth at 0.5 dB IL versus the xy plane dimensions are reported. All the simulations have been performed

with standard metallic waveguide sizes (a = 15.80 mm, b = 7.9 mm). The largest 0.5 dB IL BW is found to be 2.1% for a structure composed of 13 periods along x and 21 layers along y. In Fig. 8.10 the simulated electric field of the structure with $l_z = 6d$ is shown for xz and yz plane cuts.

Table 8.1: Central frequency f_0 and percent BW (at 0.5-dB IL) for different xy dimensions. Structure length along z is $l_z = 6d = 40.38$ mm and standard WR62 metallic waveguides are used.

xy dimensions	f_0 (GHz)	%BW
(a) 9d × 15h	17.96	1.6
(b) 9d × 21h	17.97	2
(c) 13d × 15h	17.97	1.67
(d) 13d × 21h	17.96	2.1

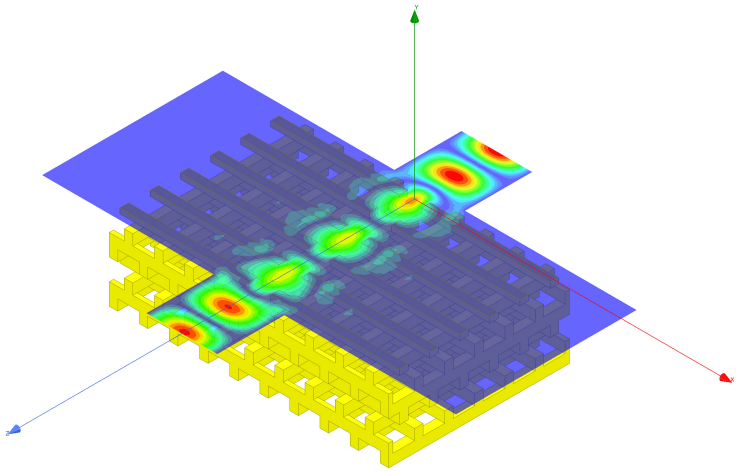

Fig. 8.10: Simulated electric field inside the structure (xz plane cut).

9

Experimental results

An alumina prototype of the EBG waveguide has been realized and experimentally characterized. The length of the device along z has been chosen equal to six periods ($\simeq 40.38$ mm). The lateral extension of the structure along the xy plane has been fixed to: 7 periods ($7d$) along x and $17h$ along y. For the realization it has been chosen to use standard WR62 launching metallic waveguides with dimensions $a = 15.8$ mm, $b = 7.9$ mm.

9.1 Fabrication of the 18 GHz woodpile waveguide

The alumina woodpile structure is shown in Fig. 9.1(a). In a second step, see Fig. 9.1(b), the alumina structure has been embedded in a box made of plexiglass with metallic input and output WR62 waveguides and flanges. The plexiglass box is also necessary in order to properly align the metallic and the woodpile waveguides.

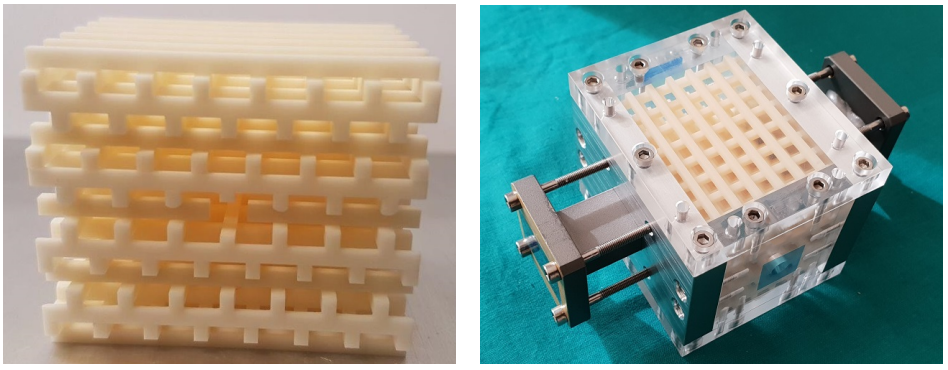

(a) (b)

Fig. 9.1: (a) Manufactured dielectric EBG woodpile structure. (b) Final device including metallic WR62 waveguides and flanges plus top, bottom, right and left side plexiglass enclosure.

The structure has been realized by stacking together 9 alumina layers with height equal to $2h$ (double layers), as shown in Fig. 9.2. Each layer has dimensions of $7d \times 6d$ in the xz plane, which corresponds to $47.11 \times 40.38\ mm^2$. The total height of the structure is fixed at $17h \simeq 40.46$ mm.

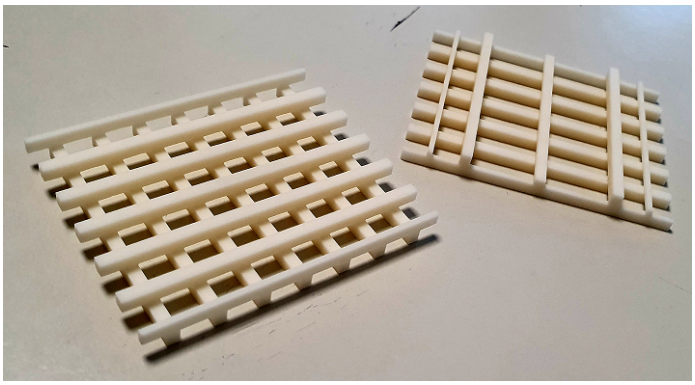

Fig. 9.2: Photo of two alumina layers used for the realization of the woodpile structure shown in Fig. 9.1.

Fig. 9.3 shows the exploded view of the realized alumina woodpile. Each layer has been worked with a milling machine and it is a single woodpile piece; as pointed before, the structure has been made symmetric along the zx plane so in the figure the symmetric layers are represented with the same colour. However, in order to create the central hollow channel, two separate pieces of a single layer have been used (orange layer). In order to fix these two pieces to the rest of the structure, two "half shaped" joints have been derived from two opposite bricks, as highlighted in Fig. 9.3. Then, by enclosing the woodpile into the final box (see Fig. 9.1(b)), the two lateral plexiglass walls act as "mechanical stop walls" for the central layer of the structure, preserving the necessary alignment.

9.2 S-parameters measurement

The experimental measurements have been carried out by means of a 2-port VNA; the setup can be seen in Fig. 9.4. The operating bandwidth is centered around 18.25 GHz and the measured scattering parameters are almost overlapped with the full wave simulations carried out with Ansys HFSS, as reported in Fig. 9.5.

The measured percent bandwidth at 0.5 dB insertion loss is 1.42%, in perfect agreement with the full wave simulation. The frequency shift of 250 MHz is due to the slight difference in lateral dimensions of the prototype with respect to the

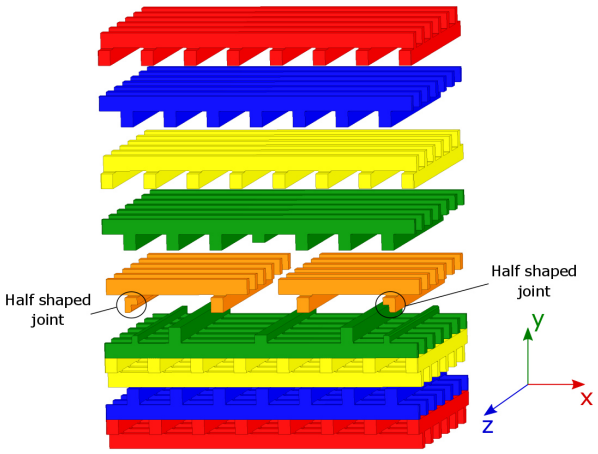

Fig. 9.3: Exploded view of the realized alumina woodpile. The structure has been made symmetric along the horizontal plane, so the red, blue, yellow and green layers are mirrored with respect to the xz plane. In order to create the central hollow channel, two separate pieces of a single layer have been used, here coloured in orange: to fix these two pieces to the rest of the structure, two "half shaped" joints have been derived from two opposite bricks, with the lateral plexiglass enclosure preserving the necessary alignment.

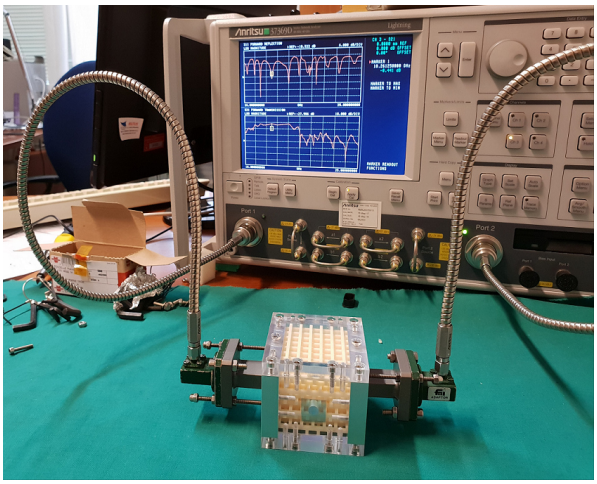

Fig. 9.4: Experimental setup used for the prototype S-Parameters measurements.

simulated model and to the fabrication tolerances. The bandwidth could be increased by adopting an optimized waveguide height $b_{opt} = 6$ mm as shown in [12]. This figure of merit could be in principle further optimized by the use of input and output waveguides with customized shape and size.

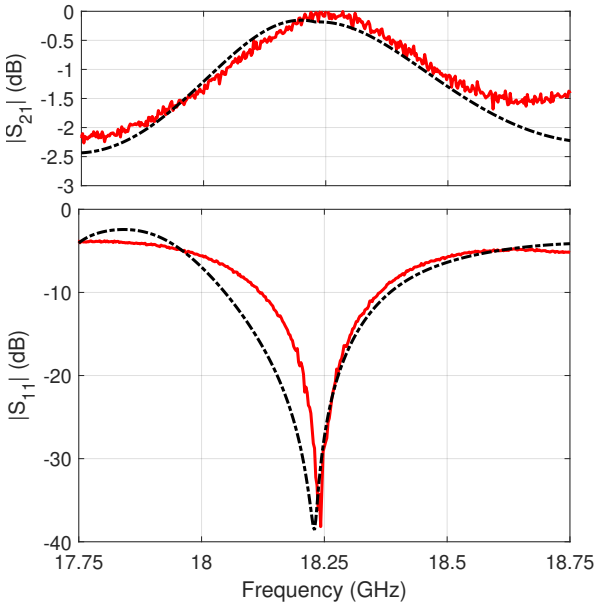

Fig. 9.5: Measured (red curves) vs. simulated (black dot-dashed curves) S-parameters of the alumina woodpile waveguide: $|S_{21}|$ (top) and $|S_{11}|$ (bottom).

9.3 Electric field measurement along the z channel

A bead-pull [49] measurement setup has been developed in order to measure the electric field profile along the longitudinal z-axis. The results here discussed are presented in [50]. The field measurement has been performed by moving a small dielectric bead, attached on a non-conductive wire, that is driven through the cavity by a motor. The perturbation at any bead position causes a $|S_{11}|$ shift that is proportional to the local field, according to the Steele non-resonant perturbation theory already mentioned in previous sections [33]. In our case, a dielectric bead of radius ≈ 0.5 mm has been moved along the hollow core axis and, for every sampled position, the value of $|S_{11}|$ at a fixed frequency has been acquired.

A schematic of the measurement setup is shown in Fig. 9.6, while a photo is shown in Fig. 9.7: the device has been connected to an open ended waveguide at the output side and to a short circuited waveguide at the input side. A coaxial probe has been inserted in the input waveguide, at a $\lambda/4$ distance from the short circuit, where a hole allows the insertion of the non-conductive wire to pull the bead along the structure axis, where the electric field has been measured. The same open/short configuration has been reproduced in a full-wave 3D simulation, where an appropriate air box with open boundary conditions has been used to simulate the air in proximity of the open output waveguide.

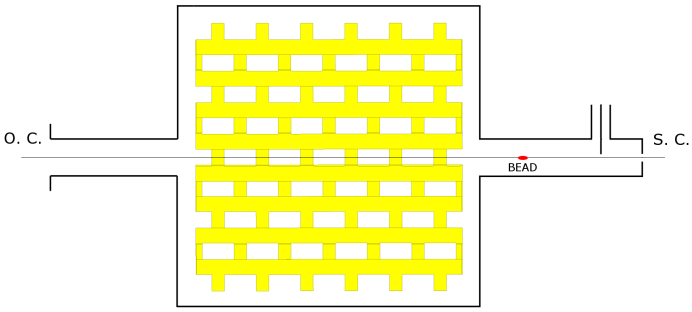

Fig. 9.6: Sketch of the bead pull setup: the woodpile structure is connected to an open ended waveguide at the output side (left side) and to a short circuited waveguide at the input side (right side), where a coaxial probe is inserted $\lambda/4$ distant from the short circuit. A non-conductive wire drives the bead along the cavity axis and the $|S_{11}|$ value is taken at every sampled position.

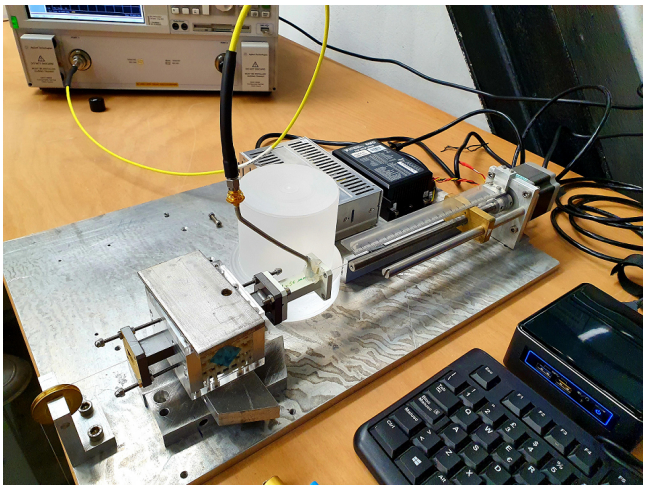

Fig. 9.7: Photo of the realized bead pull setup.

Fig. 9.8 shows the comparison between the electric field along the longitudinal axis of the structure, normalized to the maximum value, resulting from the bead-pull measurement and from the HFSS simulation. The blue curve refers to the square root of the $|S_{11}|$ measured magnitude vs. bead position at the frequency of 18.13 GHz, whereas the red curve refers to the HFSS simulation, and in particular to the electric field along the propagation direction z, plotted at the frequency of 18.13 GHz. Black vertical lines indicate the metallic waveguide-to-woodpile (input) and woodpile-to-metallic waveguide (output) interfaces.

It can be seen that the measured field profile is in good agreement with the simulated one.

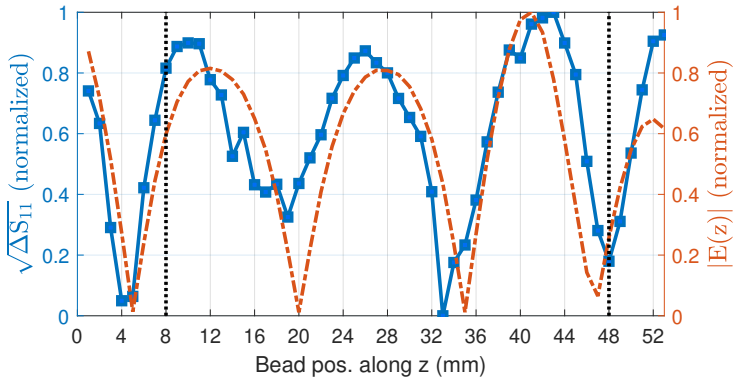

Fig. 9.8: Measured field (blue marked curve) vs HFSS simulation (red curve). Dashed vertical black lines indicate the woodpile structure input and output interfaces. The field in the metallic waveguides is also shown for $z < 8$ mm and $z > 48$ mm.

9.4 EBG waveguide as a DC-break for microwave ion sources

As pointed before, the alumina waveguide here studied as a TLC waveguide of an all-dielectric woodpile coupler can also be used as a DC-break device for microwave ion sources. Here we discuss this alternative application.

The ion sources plasma chambers are placed at high voltage (up to 50 kV [51], [52]) to allow the beam extraction. In order to insulate the high voltage plasma chamber from microwave amplifier located at ground, a device (called hereinafter DC-break) able to break the DC-path and to efficiently transfer RF power (usually up to 1 kW) has to be inserted in the RF feeding line, as seen in Fig. 9.9 where an AISHa ion source schematic is depicted. Besides the DC insulation requirement, the design of a waveguide DC-break [53] needs to take into account low reflection and negligible radiation losses of the transmitted RF power from the ground RF generator to the high voltage source. The previously presented and realized structure is able to fulfil an insulation requirement of 40 kV and low RF losses as typically required in these setups [54], and so it could be employed ad DC-break placed along the RF feeding line of microwave ion sources.

The use of a dielectric DC-break instead of a metallic one brings many advantages, immediately clear by seeing Fig. 9.10, that can be summarized as: compactness, no need of cooling setup and no need of voltage divider.

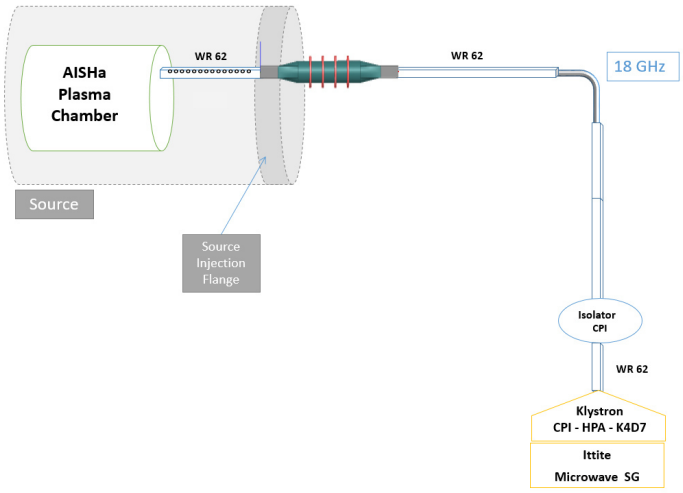

Fig. 9.9: Schematic of LNS AISHa ion source comprising the RF feeding line. In order to insulate the high voltage plasma chamber from microwave amplifier located at ground, a DC-break device able to break the DC-path and to efficiently transfer RF power (usually up to 1 kW) has to be inserted along the RF path.

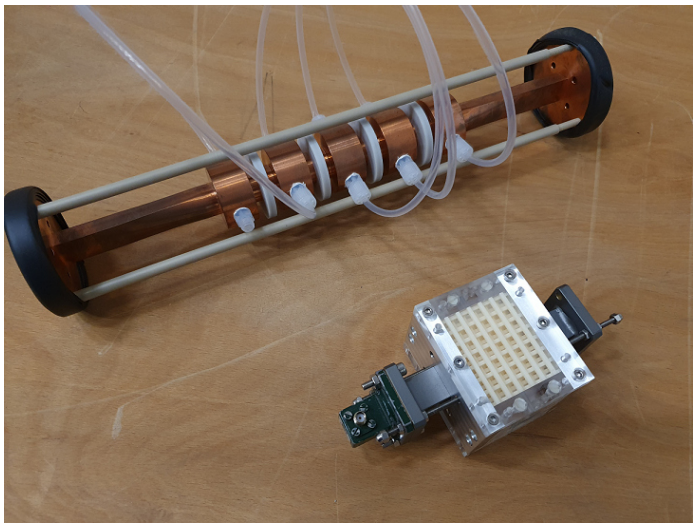

Fig. 9.10: Metallic DC-break vs. the dielectric EBG structure presented in this thesis.

10

W-band woodpile waveguide

Following the work on the 18 GHz woodpile waveguide, a W-band ($75 - 110$ GHz) dielectric woodpile PhC structure has been designed through the use of 2D and 3D full wave simulations, using the guidelines discussed in the previous chapters. The structure is presented in [55].

As said, this silicon ($\epsilon_r = 11$) woodpile waveguide has been designed to work in the W- band ($75 - 110$ GHz), and more precisely around 96.6 GHz. This EBG structure has been designed to operate around 100 GHz since it is desirable to have the operating frequency higher by 60% than the cut-off frequency (59.015 GHz) of the fundamental TE10 mode for the W-band standard WR10 waveguide (2.54 mm $\times$ 1.27 mm), which has been chosen as I/O metallic waveguide. The first step in the design of the woodpile structure for millimetre-wave frequencies has been the determination of optimal brick width (w) and height (h), in order to maximize the frequency band-gap: as discussed in §8, it is found that for the FCC lattice the optimal normalized dimensions for this purpose are equal to $w = 0.2\sqrt{2}d$, $h = 0.25\sqrt{2}d$.

The MIT Photonic-Bands (MPB) package has been used for computation of the dispersion diagram of the infinitely periodic structure.

Once the band-gap has been maximized, the structure period d has been chosen in the way to center it at the frequency of interest, in this case 96.6 GHz. By imposing $d = 1.2$ mm, the remaining parameters have been found as $w = 0.334$ mm, $h = 0.425$ mm. Subsequently, a defect has been created by removing some silicon from the structure, in the way to trap a guided mode. In the case at hand, a rectangular $w_d \times h_d$ defect has been created at the center of the silicon structure. The optimization of this guiding defect led to the dimensions $w_d = 0.877$ mm, $h_d = 0.850$ mm. The corresponding projected band diagram is visible in Fig. 10.1: the red curve represents the dispersion curve of the trapped mode that propagates along the structure, inside the defect, at the frequency of 96.6 GHz.

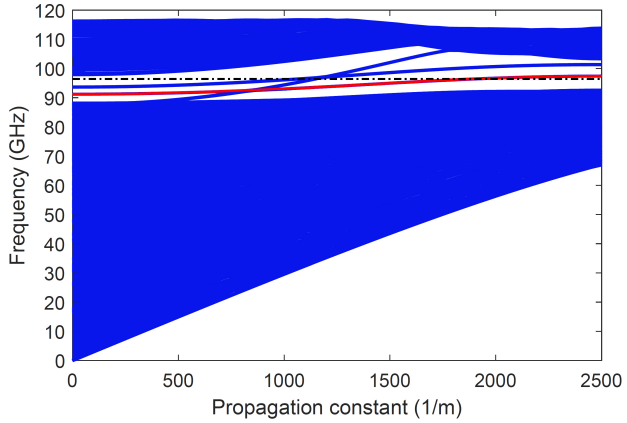

Fig. 10.1: Projected band diagram of the designed structure. For $d = 1.2$ mm the trapped mode (red curve) can be centered at the frequency of interest (black horizontal line).

Following the successful design of the 18 GHz structure, a simple metallic waveguide-to-woodpile transition has been used for the W-band structure: the standard WR10 input and output metallic waveguides are only juxtaposed to the dielectric woodpile waveguide and no custom cut of the silicon structure was necessary. This approach is possible since the fundamental mode of the rectangular waveguide is similar to the woodpile waveguide mode and an efficient transition can be achieved [40]. In Fig. 10.2 the transverse electric field profile of the standard metallic WR10 waveguide and of the woodpile waveguide at $z = 0$ mm cut (input interface) are plotted, showing a good overlap between the TE10 mode of the WR10 waveguide and the TE10-like mode of the woodpile structure.

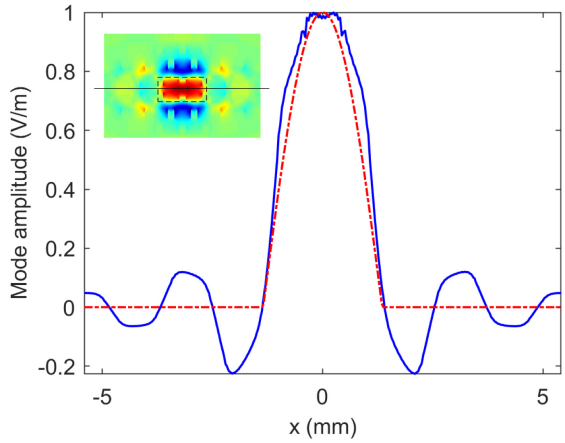

Fig. 10.2: Transverse electric field profile (see the inset) of the standard metallic WR10 waveguide (red curve) and of the woodpile waveguide (blue curve) at $z = 0$ mm cut (input port).

10.1 Realization and experimental validation

A silicon prototype has been realized and experimentally characterized: the device can be seen in Fig 10.3, while in Fig 10.4 a step during the silicon layers alignment process is depicted.

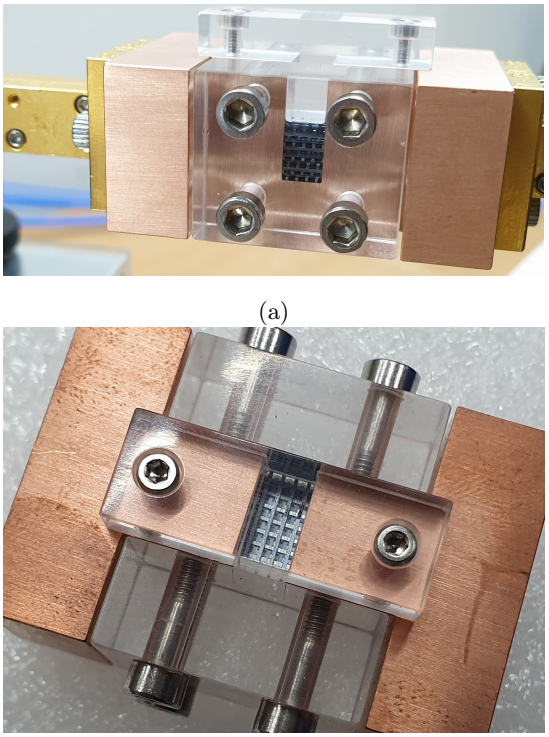

(a)

(b)

Fig. 10.3: (a) side and (b) top view of the silicon EBG woodpile waveguide. Metal enclosure for alignment and input/output waveguide connection is visible.

S-parameter measurements have been carried out using a vector network analyzer (4-port N5245B PNA-X rent from Keysight) configured with a pair of WR10 waveguide frequency multiplier VDI Mini-Module heads that cover the complete W-band (i. e. from 75 to 110 GHz). Fig 10.5 shows a photo of experimental setup used to characterize the structure: the manufactured woodpile waveguide and the rectangular metallic transition have been connected to the mm-wave extension heads of the Agilent PNA-X Vector Network Analyzer.

An interval of $[95; 98]$ GHz, with a frequency step of 12.5 MHz, has been set on the VNA. Fig. 10.6 shows the measured $|S_{11}|$ and $|S_{21}|$ curves for the manufactured silicon woodpile. The measurements have been compared to simulations, which are based on the nominal dimensions of the woodpile and include the actual length of the

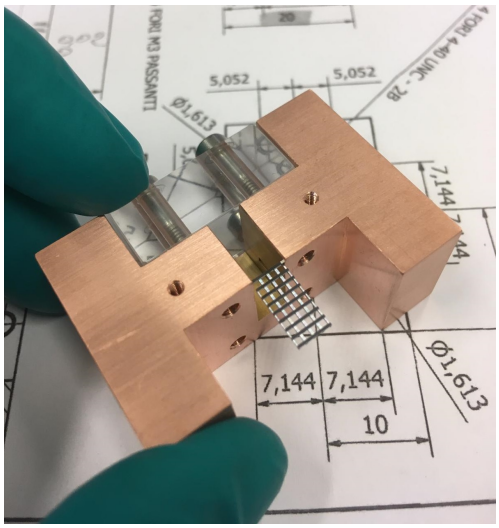

Fig. 10.4: Photo of the silicon layers alignment process inside the containment box.

Fig. 10.5: Photo of the experimental setup used to measure S-parameters of the structure: the manufactured woodpile waveguide and rectangular waveguide to EBG waveguide transition have been connected to the mm-wave extension heads of the Agilent PNA-X Vector Network Analyzer.

WR10 waveguides as well, showing that the measured scattering parameters are in very good agreement with HFSS results. The prototype exhibits a $|S_{11}|$ and a $|S_{12}|$ values of -32 dB and -0.46 dB respectively, at the frequency of 96.6 GHz; this results in approximately 0.1 dB loss per period as in [41]. System losses are mainly due to the discontinuity at the interfaces between the network analyzer adapters and the waveguide input/output ports.

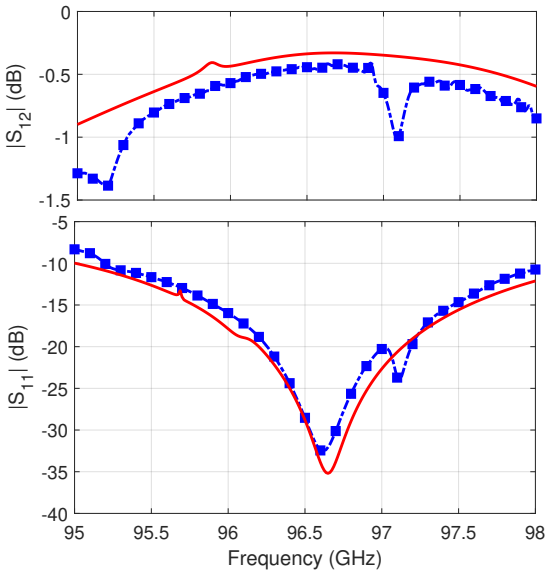

Fig. 10.6: Measured (blue marked curves) vs. simulated (red curves) S-parameters of the silicon woodpile waveguide: $|S_{12}|$ (top) and $|S_{11}|$ (bottom).

The measurement results reproduce most of the features present in the numerical predictions, although there is a small frequency shift caused by the manufacturing tolerances.

The next step will be the design of a full dielectric woodpile coupler capable to transform a standard "telecom" mode into an accelerating mode, in a similar fashion of the structure of Fig. 6.1 but with the advantage of a complete 3D mode confinement (see Fig. 6.2).

11

Conclusions and perspectives

This thesis focused on the numerical simulation and tuning methods for metallic and dielectric accelerators.

The first part dealt with metallic accelerators. After describing the typical accelerating structures for protons and electrons, with their peculiar differences, and giving the fundamental parameters of merits of an accelerator, the attention focused on the analytical and numerical methods developed in the way to simplify the simulation of large electromagnetic structures such as the Drift Tube Linac. The proposed methods can be easily applied when using commercial electromagnetic simulators such as Ansys HFSS and CST Microwave Studio and follows a dual approach: 1) permits to resolve a complex model simulation by predicting the frequency error introduced by structure discretization or 2) reduce the problem to a simpler one by exploiting the cavity rotational symmetry and creating equivalent rotationally symmetric volumes in place of those that don't have the desired symmetry. Both methods have been successfully applied for the simulations of the ESS DTL with very good results in terms of frequency and accelerating field.

The proposed methods have been experimentally validated against measured data by the employment of a ESS DTL tank 2 cold model, built and tested at INFN-LNL; this prototype has been used in order to develop and test the bead-pull field measurement setup and to apply the necessary stabilization and tuning procedures to make the accelerating field immune from manufacturing errors, a mandatory requisite for proper particle acceleration. The process is composed of various steps. After the assembly and alignment, done with a precision equal or greater than $\simeq 0.1$ mm with respect to the fiducial coordinates, that was found sufficient for the desired RF tuning purposes, the bead-pull measurement setup has been arranged: two plates have been mounted at low and high ends of the tank and a wire has been passed through the cavity axis, for the entire tank length. The bead-pull setup also includes a LabView program that controls the motor and the measure acquisition, and a MATLAB

program that deals with the measure post processing. The stabilization procedure is actually performed by inserting metal cylinders, called post couplers, inside the tank. The objective is to make the field immune to perturbation and, for every i-th cell, this can be done by a sequence of iterative steps of tuning, field measurement and tilt sensitivity observation. At the end of the stabilization campaign, the range of TS and electric field was brought to $\pm 5\%$, showing the correctness of the developed procedure.

The last chapter of the metallic accelerators part presented the experimental characterization of a novel launching-accelerating travelling wave structure for electrons, operating at X-band and able to achieve high accelerating gradient in order to increase brilliance of accelerated bunches. The structure, developed in the framework of the collaboration between INFN-LNS, INFN-LNF and SLAC (USA), is composed of a power coupler which consists of a mode launcher that converts the rectangular TE_{10} mode into the circular TM_{01} accelerating mode and adopts a fourfold symmetry in order to minimize both the dipole and the quadrupole RF components with the purpose of mitigate the emittance growth in the early stages of the acceleration process. A cold model prototype has been realized and experimentally characterized: S-parameters and electric field have been measured, showing very good agreement with the simulations.

The second part of this thesis concerned the dielectric laser accelerators. These innovative structures eliminate the major issues of the metallic accelerators, such power dissipation at high frequency, while at the same time offering the possibility to obtain very high accelerating gradients. As discussed in the first section of part 2, these structures are built exploiting the concepts and geometry of the photonic crystals, structures that can allow or inhibit the wave propagation in specific directions, creating a so called electromagnetic band gap. Of course, it is desirable to control wave propagation (or confinement) in all the three directions, so usually a 3D photonic crystal geometry is employed. If a specific amount of dielectric material is removed from such periodic structure, a defect is created and it can be used to support a guided mode. In the thesis the attention has been focused on the woodpile structure due to its capability to confine waves in three dimensions. The study began with the evaluation of the band diagram for an infinite structure; this has been done by the use of the Mit Photonic Bands package, which returns also the optimal project parameters (i. e. the structure parameters that leads to the largest band-gap). The second step has been the creation of the defect for the guided mode confinement. The infinite structure has then truncated, centered at the operating frequency (in our case 18 GHz) and simu-

lated by the use of Ansys HFSS. Standard metallic waveguides have been adopted to launch the TE_{10} mode into the structure; these metallic waveguides have been juxtaposed to the dielectric structure, without the need of elaborate geometries, making simpler the realization process. The simulations showed that the dielectric woodpile waveguide well confines the guided mode, with good performances in the band of interest. The latter can be enlarged by the use of custom metallic launch waveguides and by increasing the transversal dimensions of the crystal (or by a conjunction of both), as demonstrated by numerical simulations. The encouraging results obtained in simulation have led to the realization of a prototype working at 18 GHz: this structure has been made by stacking together layers of alumina bricks and by enclosing them into a box composed of two metallic input and output flanges and lateral plexiglass walls for protection and alignment. The structure has been experimentally validated, showing very good agreement with the simulations in terms of S-parameters. Also, on axis electric field has been measured through the bead-pull technique, confirming the expected results. After the validation of the 18 GHz structure, it has been scaled up in the W-band and a second prototype, this time made of silicon, has been realized and characterized, even here showing an excellent agreement with the simulations.

The next step will be the realization of a full 3D dielectric woodpile coupler, capable to transform a standard "telecom" mode into an accelerating mode suitable for electron acceleration.

12

Acknowledgments

The arguments presented in this thesis took three years to be mastered and a lot of people have been involved into the theoretical studies and experimental activities. I wish to thank all of them, whose assistance and guidance were fundamental in the completion of the presented work.

The metallic accelerator work has been carried out at Laboratori Nazionali di Legnaro of INFN, while the Dielectric Laser Accelerators work has been performed at Laboratori Nazionali del Sud of INFN, with a fruitful collaboration between INFN-LNS and University of Brescia. First of all, I wish to express my deepest gratitude to my tutors: Dr. Luigi Celona and Prof. Gino Sorbello (who also supported me for my master thesis at University of Catania), for their essential support during the key periods of my work. With knowledge and patience, they guided and encouraged me even when the road got tough. Without their help, this work would not have been realized. I thank the LNS director, Dr. Santo Gammino, for the opportunity to work in the exciting and challenging environment of INFN-LNS, that made me hungry for knowledge and pushed me to improve as a researcher and as a person. I wish to express my gratitude to Dr. David Mascali, who believed in me and supported my work since my arrival at INFN-LNS. He gave me the opportunity to be part of many thrilling and future-looking projects, along with a fantastic and professional team of people. Our strength lies in unity and this will lead us to success in all our activities. I thank my colleague Giuseppe Torrisi: our frequent discussions gave me hints and precious ideas that helped me to improve the overall work and in particular the numerical modelling of the dielectric devices that have been presented. I wish to thank Prof. Costantino De Angelis and Prof. Andrea Locatelli of University of Brescia for their invaluable assistance on the dielectric laser accelerators study. Their knowledge helped me to advance in the design of these complex structures, overcoming the difficulties that have presented along the path. I thank Dr. Andrea Pisent and all the INFN-LNL staff for their support during the ESS DTL activities. In particular,

thanks to Francesco Grespan, Antonio Palmieri and Luigi Ferrari, whose assistance on the mechanical aspects and on the RF tuning procedures of the tank 2 has been fundamental for the success of the work. I also thank Prof. Loreto Di Donato and Dr. Santi Pavone of University of Catania for their friendship along the years and their always present support to me and to all our activities. Furthermore, I would to acknowledge all the INFN-LNS staff for the constant support, both technical and administrative, that they gave and still give me everyday. I would like to pay my special regards to Prof. Tommaso Isernia of University of Reggio Calabria for his essential advices on how to improve my PhD work, and to Prof. Giuseppe Della Valle of University of Milano and Prof. Luca Vincetti of University of Modena and Reggio Emilia for their precious reviews that helped to improve this manuscript. A very special thank to all my colleagues of LNS, that I rather call friends: Ornella Leonardi, Andrea Miraglia, Davide Siliato, Antonio Massara, Carmen Altana, Maria Mazzaglia, Eugenia Naselli, Martina Ursino, Nancy Martorana, Angelo Pidatella, Giuseppe Castro, Grazia D'Agostino, Jessica Bellone, Vincenzo Minissale, Vincenza Bonanno, Alberto Longhitano. Thanks to all of you not only for you support but also for you presence, that makes my days perfect.

I thank my lifetime friends, Salvatore Monaco and Salvatore Fresta, because they always have been here for me in the times of need.

Finally, I thank my family for the infinite support they gave me throughout my life. Thanks to Roberta for always being with me: the goals I've reached wouldn't have been achievable without you.

Bibliography

[1] John J. Livingood. *PRINCIPLES OF CYCLIC PARTICLE ACCELERATORS*. D. VAN NOSTRAND COMPANY, INC., 1961.

[2] *Differences between electron and ion linacs*. URL: https://cds.cern.ch/record/1005048/files/p179.pdf.

[3] Martin Reiser. *Theory and Design of Charged Particle Beams*. WILEY-VCH Verlag GmbH & Co. KGaA, Weinheim, 2008.

[4] R Joel England, Robert J Noble, Karl Bane, David H Dowell, Cho-Kuen Ng, James E Spencer, Sami Tantawi, Ziran Wu, Robert L Byer, Edgar Peralta, et al. "Dielectric laser accelerators". In: *Reviews of Modern Physics* 86.4 (2014), p. 1337.

[5] D. Alesini, G. Castorina, M. Croia, M. Ferrario, A. Gallo, B. Spataro, C. Vaccarezza, A. Vannozzi, M. Diomende, A. Giribono, and F. Cardelli. "Design of a Full C-Band Injector for Ultra-High Brightness Electron Beam". In: *10th Int. Particle Accelerator Conf* (2019), pp. 1979–1982.

[6] G. Torrisi, G. S. Mauro, L. Celona, D. Mascali, S. Gammino, G. Sorbello, C. De Angelis, and A. Locatelli. "Numerical Study of Photonic-Crystal-Based Dielectric Accelerators". In: *10th Int. Particle Accelerator Conf., IPAC 2019* (2019), pp. 3653 –3656. DOI: 10.18429/JACoW-IPAC2019-THPGW033.

[9] Ardavan F Oskooi, David Roundy, Mihai Ibanescu, Peter Bermel, John D Joannopoulos, and Steven G Johnson. "MEEP: A flexible free-software package for electromagnetic simulations by the FDTD method". In: *Computer Physics Communications* 181.3 (2010), pp. 687–702.

[10] G Castorina, G Torrisi, G Sorbello, L Celona, and A Mostacci. "Conductor losses calculation in two-dimensional simulations of H-plane rectangular waveguides". In: *Journal of Electromagnetic Waves and Applications* 33.8 (2019), pp. 981–990.

[11] Marinella Aloisio and Gino Sorbello. "One-third-of-pitch reduction technique for the analysis of ternary azimuthally periodic helical slow-wave structures". In: *IEEE Trans. Electron Devices* 53.6 (2006), pp. 1467–1473.

[13] G Torrisi, G Sorbello, O Leonardi, D Mascali, L Celona, and S Gammino. "A new launching scheme for ECR plasma based on two-waveguides-array". In: *Microwave and Optical Technology Letters* 58.11 (2016), pp. 2629–2634.

[14] Christopher D Nantista and Sami G Tantawi. "A compact, planar, eight-port waveguide power divider/combiner: The cross potent superhybrid". In: *IEEE Microwave and Guided Wave Letters* 10.12 (2000), pp. 520–522.

[15] *Los Alamos National Laboratory, Superfish.*

[16] "Particle Accelerators". In: vol. 7. 1976, pp. 213–222.

[17] ANSYS HFSS. *Ansoft Corp., Pittsburgh, PA.* 2018.

[18] Thomas P. Wangler. *RF Linear Accelerators.* Wiley-VCH, 2008.

[19] L. F. Chen, C. K. Ong, and C. P. Neo. *Microwave Electronics - Measurement and Materials Characterization.* Wiley, 2004.

[20] J. C. Slater. *Microwave Electronics.* D. Van Nostrand Company Inc., 1950, p. 80.

[22] T. Hays H. Padamsee J. Knobloch. *RF Superconductivity for Accelerators.* 2008.

[23] James H. Billen and Alan H. Shapiro. "Post-coupler stabilization and tuning of a ramped-gradient Drift-Tube Linac". In: *Proceedings of the 1988 Linear Accelerator Conference, Williamsburg, Virginia, USA* (1988), pp. 128–130.

[24] M. R. Khalvati. "Stabilization Strategies for Drift Tube Linacs". PhD thesis. Institute for Research in Fundamental Science, Institute for Studies in Theoretical Physics and Mathematics (IPM), 2016.

[25] Mohammed Reza Khalvati and Suitbert Ramberger. "Straightforward and accurate technique for post-coupler stabilization in drift tube linac structures". In: *Physical Review Accelerators And Beams* (2016).

[26] Thomas P. Wangler, James Billen, and Roderich Keller. "Spallation Neutron Source (SNS) Front End and Linac Course". In: (2004).

[27] F. Grespan, G. De Michele, S. Ramberger, and M. Vretenar. "An equivalent circuit for post coupler stabilization in a drift tube linac". In: *Proceedings of Linear Accelerator Conference LINAC2010, Tsukuba, Japan* (2010), pp. 578–580.

[28] D. E. Nagle, E. A. Knapp, and B. C. Knapp. "Coupled Resonator Model for Standing Wave Accelerator Tanks". In: *Rev. Sci. Instrum.* 38.11 (1967), pp. 1583–1587.

[29] F. Grespan. "Study of DTL stabilization with post couplers for the SPES driver LINAC". PhD thesis. CERN, 2009.

[31] G Castorina, L Ficcadenti, M Migliorati, A Mostacci, L Palumbo, F Cardelli, G Franzini, A Marcelli, B Spataro, B Sorbello, L Celona, S Gammino, G Torrisi, A Cahill, J Rosenzweig, and V Dolgashev. "TM01 mode launcher with quadrupole field components cancellation for high brightness applications". In: *J. Phys.: Conf. Ser.* (2018), p. 1067 082025.

[32] Giovanni Castorina et al. "A Compact Mode Launcher for New Generation RF Photoinjectors and High Brightness Applications". In: *submitted to: Proc.*

of International Particle Accelerator Conference (IPAC'18), 9. Vancouver, Canada: JACoW, 2018.

[33] Charles W. Steele. "A Nonresonant Perturbation Theory". In: *IEEE Trans. Microw. Theory Techn.* MTT-14.2 (1966), pp. 70–74.

[34] A. Mostacci, L. Palumbo, R. Da Re, D. Alesini, L. Ficcadenti, and B. Spataro. "About Non Resonant Perturbation Field Measurement in Standing Wave Cavities". In: *Particle Accelerator Conference (PAC09)* (2009).

[35] In: URL: http://www.comeb.it.

[36] Guo Liu, Yan Wang, Youlei Pu, Jianxun Wang, Ran Yan, Yong Luo, and Shafei Wang. "A Millimeter Wave High-Order TE13 Mode Converter". In: *IEEE Transactions on Electron Devices* 63 (May 2016), pp. 1–5. DOI: 10.1109/TED.2016.2562025.

[37] Ching-Fang Yu and Tsun-Hsu Chang. "High-performance circular TE01-mode converter". In: *Microwave Theory and Techniques, IEEE Transactions on* 53 (Jan. 2006), pp. 3794 –3798. DOI: 10.1109/TMTT.2005.859866.

[38] MIT Photonic Bands (MPB). *Massachusetts Institute of Technology.* 2019.

[39] A Locatelli, G Sorbello, G Torrisi, L Celona, and C De Angelis. "Photonic crystal waveguides for particle acceleration". In: *2017 Progress In Electromagnetics Research Symposium-Spring (PIERS).* IEEE. 2017, pp. 1008–1013.

[41] I. Ederra, I. Khromova, R. Gonzalo, N. Delhote, D. Baillargeat, A. Murk, B. E. J. Alderman, and P. de Maagt. "Electromagnetic-Bandgap Waveguide for the Millimeter Range". In: *IEEE Transactions on Microwave Theory and Techniques* 58.7 (2010), pp. 1734–1741.

[42] HS Sözüer and Jonathan P Dowling. "Photonic band calculations for woodpile structures". In: *Journal of Modern Optics* 41.2 (1994), pp. 231–239.

[43] Edmond Chow, SY Lin, SG Johnson, PR Villeneuve, and JD Joannopoulos. "Fully confined photonic band gap and guided modes in a two-dimensional photonic crystal slab". In: *Lasers and Electro-Optics, 2000.(CLEO 2000). Conference on.* IEEE. 2000, pp. 87–88.

[46] John D Joannopoulos, Steven G Johnson, Joshua N Winn, and Robert D Meade. *Photonic crystals: molding the flow of light.* Princeton university press, 2011.

[47] Bartlomiej Salski. "The unfolding of bandgap diagrams of hexagonal photonic crystals computed with FDTD". In: *Progress In Electromagnetics Research* 27 (2012), pp. 27–39.

[48] A. R. Weily, K. P. Esselle, T. S. Bird, and B. C. Sanders. "Experimental woodpile EBG waveguides, bends and power dividers at microwave frequencies". In: *Electronics Letters* 42.1 (2006), pp. 32–3–.

[49] D. Alesini, A. Falone, M. Migliorati, A. Mostacci, F. Palpini, L. Palumbo, and B. Spataro. "Design and RF measurements of an X-band accelerating structure for linearizing the longitudinal emittance at SPARC". In: *Nucl. Instr. Meth. Phys. Res. A: Accelerators, Spectrometers, Detectors and Associated Equipment* 554.1 (2005), pp. 1 –12. ISSN: 0168-9002. DOI: https://doi.org/10.1016/j.nima.2005.07.072. URL: http://www.sciencedirect.com/science/article/pii/S0168900205015238.

[51] Yong-Sub Cho, Dae-Il Kim, Han-Sung Kim, Kyung-Tae Seol, and Hyeok-Jung Kwon. "Multi-layered waveguide DC electrical break for the PEFP microwave proton source". In: *Journal of the Korean Physical Society* 63.11 (2013), pp. 2085–2088.

[52] Terence Taylor and Jozef F. Mouris. "An advanced high-current low-emittance dc microwave proton source". In: *Nuclear Instruments and Methods in Physics Research* (1993), pp. 1–5.

[53] O. Leonardi, G. Torrisi, L. Di Donato, A. Locatelli, L. Celona, C. De Angelis, and G. Sorbello. "Hollow-core electromagnetic band gap waveguide as DC-break for ion sources". In: *2017 Progress In Electromagnetics Research Symposium - Spring (PIERS)*. 2017, pp. 1014–1017.

[54] O. Leonardi, G. Torrisi, G. Sorbello, L. Celona, and S. Gammino. "A compact DC-break for ECR ion source at 18 GHz". In: *Microwave and Optical Technology Letters (in press)* (2018).

Publications

[6] G. Torrisi, G. S. Mauro, L. Celona, D. Mascali, S. Gammino, G. Sorbello, C. De Angelis, and A. Locatelli. "Numerical Study of Photonic-Crystal-Based Dielectric Accelerators". In: *10th Int. Particle Accelerator Conf., IPAC 2019* (2019), pp. 3653 –3656. DOI: 10.18429/JACoW-IPAC2019-THPGW033.

[7] G. S. Mauro and A. Palmieri. "INFN-LNL Annual Report". In: (2016), p. 189.

[8] G.S. Mauro, A. Palmieri, F. Grespan, G. Torrisi, O. Leonardi, L. Celona, G. Sorbello, and A. Pisent. "Analytical Method, based on Slater Perturbation Theorem, to Control Frequency Error when representing Cylindrical Structures in 3D Simulators". In: *13th European Conference on Antennas and Propagation, EuCAP 2019* (2019).

[12] G.S. Mauro, A. Locatelli, G. Torrisi, L. Celona, C. De Angelis, and G. Sorbello. "Woodpile EBG waveguide as a DC electrical break for microwave ion sources". In: *Microw. Opt. Technol. Lett.* 61 (2018), pp. 610 –614. DOI: 10.1002/mop.31628.

[21] G.S. Mauro, F. Grespan, A. Palmieri, A. Pisent, C. Mingioni, M. Nenni, P. Mereu, and M. Mezzano. "Field Uniformity Preservation Strategies for the ESS DTL: Approach and Simulations". In: *8th International Particle Accelerator Conference, IPAC 2017* (2017), pp. 4139 –4141.

[30] G Torrisi, G. Sorbello, L. Celona, O. Leonardi, G. Mauro, and S. Gammino. "Low Power RF Test of a Quadrupole-Free X-Band Mode Launcher for High Brightness Applications". In: *10th Int. Particle Accelerator Conf., IPAC 2019* (2019), pp. 2856 –2859. DOI: 10.18429/JACoW-IPAC2019-WEPRB024.

[40] G. Torrisi, G. Sorbello, O. Leonardi, L. Celona, G. Mauro, S. Gammino, G. Castorina, B. Spataro, and V. Dolgashev. "Closed-to-open conversion of a mm-wave Gaussian Horn antenna". In: *IET Conference Publications* (2018). DOI: 10.1049/cp.2018.1146.

[44] G.S. Mauro, A. Locatelli, G. Torrisi, A. Rovelli, L. Celona, C. De Angelis, G. Sorbello, and S. Gammino. "Hollow Core Dielectric EBG Waveguide to feed Microwave Ion Sources". In: *13th European Conference on Antennas and Propagation, EuCAP 2019* (2019).

[45] G.S. Mauro, A. Locatelli, G. Torrisi, O. Leonardi, F. Chines, L. Celona, C. De Angelis, G. Sorbello, and S. Gammino. "RF and DC electrical characterization of a Woodpile EBG Waveguide for Microwave Ion Sources". In: *PhotonIcs & Electromagnetics Research Symposium, PIERS 2019* (2019).

[50] G.S. Mauro, A. Locatelli, G. Torrisi, O. Leonardi, L. Celona, C. De Angelis, and G. Sorbello. "Fabrication and Characterization of Woodpile Waveguides for Microwave Injection in Ion Sources". In: *accepted in IEEE Trans. Microw. Theory Tech.* (2019).

[55] G. Torrisi, A. Locatelli, G.S. Mauro, M. Bellettato, L. Celona, F. Mancarella, C. De Angelis, and G. Sorbello. "Design and Characterization of a Silicon W-band Woodpile Photonic Crystal Waveguide". In: *accepted in IEEE Microw. Wirel. Compon. Lett.* (2019).